

UNIVERSIDADE FEDERAL DE MINAS GERAIS
PROGRAMA DE PÓS-GRADUAÇÃO EM ENGENHARIA QUÍMICA

MASTER`S DEGREE DISSERTATION

**Solar pyrolysis and electrical furnace pyrolysis of *Luffa cylindrica* fibers to obtain
adsorbent biochar**

Author: Pedro Henrique Cabral de Souza

Advisor: Prof. Daniel Bastos de Rezende

Co-Advisor: Prof. Sônia Denise Ferreira Rocha

JANUARY/2022

UNIVERSIDADE FEDERAL DE MINAS GERAIS

Pedro Henrique Cabral de Souza

Solar pyrolysis and electrical furnace pyrolysis of *Luffa cylindrica* fibers to obtain adsorbent biochar

Master`s Degree Dissertation presented to the Chemical Engineering Post-Graduation Program of the Engineering School of the Federal University of Minas Gerais as a requirement for obtaining a Chemical Engineering Master`s Degree.

Concentration area: Engenharia de Sistemas em Processos

Advisor: Prof. Daniel Bastos de Rezende

Co-Advisor: Prof. Sônia Denise Ferreira Rocha

January/2022

S729s Souza, Pedro Henrique Cabral de.
Solar pyrolysis and electrical furnace pyrolysis of *Luffa cylindrica* fibers to obtain adsorbent biochar [recurso eletrônico] / Pedro Henrique Cabral de Souza. - 2022.
1 recurso online (115 f. : il., color.) : pdf.

Orientador: Daniel Bastos de Rezende.
Coorientador: Sônia Denise Ferreira Rocha.

Dissertação (mestrado) - Universidade Federal de Minas Gerais, Escola de Engenharia.

Anexos: f. 94-115.

Bibliografia: f. 83-93.
Exigências do sistema: Adobe Acrobat Reader.

1. Engenharia química - Teses. 2. Adsorção - Teses. 3. Biomassa - Teses. 4. Energia solar - Teses. 5. Pirolise - Teses. I. Rezende, Daniel Bastos de. II. Rocha, Sônia Denise Ferreira. III. Universidade Federal de Minas Gerais. Escola de Engenharia. IV. Título.

CDU: 66.0(043)



UNIVERSIDADE FEDERAL DE MINAS GERAIS
ESCOLA DE ENGENHARIA
PROGRAMA DE PÓS-GRADUAÇÃO EM ENGENHARIA QUÍMICA

ATA DA 290ª DEFESA DE DISSERTAÇÃO DE MESTRADO

Às quatorze horas do dia 14 de janeiro de 2022, por videoconferência, foi dado início à defesa de dissertação de Mestrado do aluno **Pedro Henrique Cabral de Souza**, intitulada: **“Solar pyrolysis and electrical furnace pyrolysis of Luffa cylindrica fibers to obtain adsorbent biochar”**. A Banca Examinadora foi composta pelos seguintes membros: Prof. Dr. Mateus de Souza Amaral (UFOP), Profa. Dra. Érika Cristina Cren (DEQ/UFMG), Profa. Dra. Sônia Denise Ferreira Rocha (DEMIN/UFMG), Coordenadora, e Prof. Dr. Daniel Bastos de Rezende (DEQ/UFMG), Orientador. Após a apresentação do trabalho pelo mestrando, o professor orientador, Presidente da sessão, passou a palavra aos membros da banca para que procedessem aos comentários e à arguição do aluno. Terminada essa etapa, os examinadores se reuniram sem a presença do aluno para deliberação e expedição do resultado final. A dissertação foi **APROVADA** pelos membros da banca e o resultado final foi comunicado publicamente ao aluno. Para fazer jus ao título de Mestre em Engenharia Química, a versão final da dissertação, devidamente conferida pelo orientador, deverá ser entregue na Secretaria do PPGEQ dentro do prazo de 60 (sessenta) dias, a partir da data da defesa, de acordo com o previsto no Regulamento do Programa, art. 56, § 2º. Após a entrega do exemplar definitivo, o resultado será homologado pelo Colegiado do Programa, conferindo título de validade nacional ao aprovado. Nada mais havendo a tratar, o Presidente encerrou a sessão, da qual foi lavrada a presente ata que será assinada pelos membros da Banca Examinadora. Belo Horizonte, 14 de janeiro de 2022.



Documento assinado eletronicamente por **Erika Cristina Cren, Coordenador(a) de curso**, em 14/01/2022, às 16:41, conforme horário oficial de Brasília, com fundamento no art. 5º do [Decreto nº 10.543, de 13 de novembro de 2020](#).



Documento assinado eletronicamente por **Daniel Bastos de Rezende, Professor do Magistério Superior**, em 14/01/2022, às 16:47, conforme horário oficial de Brasília, com fundamento no art. 5º do [Decreto nº 10.543, de 13 de novembro de 2020](#).



Documento assinado eletronicamente por **Mateus de Souza Amaral, Usuário Externo**, em 14/01/2022, às 16:50, conforme horário oficial de Brasília, com fundamento no art. 5º do [Decreto nº 10.543, de 13 de novembro de 2020](#).



Documento assinado eletronicamente por **Sônia Denise Ferreira Rocha, Professora do Magistério Superior**, em 14/01/2022, às 16:50, conforme horário oficial de Brasília, com fundamento no art. 5º do [Decreto nº 10.543, de 13 de novembro de 2020](#).



A autenticidade deste documento pode ser conferida no site https://sei.ufmg.br/sei/controlador_externo.php?acao=documento_conferir&id_orgao_acesso_externo=0, informando o código verificador **1175337** e o código CRC **5B394873**.

ACKNOWLEDGMENTS

One can achieve nothing alone. It is part of our nature. We are born from people, we learn from people, we work for people and experience joy through people. Thus, this work is as much mine as it is of anyone who has ever contributed to my journey.

First and foremost, I thank the sovereign and triune God for his breath of life and salvation in his Son, Jesus Christ. His lingering grace carried me forward when my feet could not walk. *Soli Deo Gloria.*

I am very grateful to my advisor, prof. Daniel, for all the guidance and for the freedom to explore and decide on the directions of the research. Daniel committed himself many times to this work as if it were his own. This project could not be if not for his support. It was an honor to be mentored by him and to be part of the birth of LPT (Laboratório de Processos Termoquímicos).

I thankfully acknowledge my co-advisor, prof. Sonia, who contributed a lot with her experience and her bright character. Her counsels and insights were crucial for the development of the work. I also thank all MinPEnv (Mineral Processing and Environment Laboratory) colleagues, especially Elbert, who helped me a lot in the preliminary adsorption experiments.

I thankfully acknowledge the CNPq (Conselho Nacional de Desenvolvimento Científico e Tecnológico) for the granted scholarship, which was of major importance for my personal sustenance.

I thank the LEC (Laboratório de Ensaios de Combustíveis) in the person of prof. Vânia Pasa for all the provided support for pyrolysis experiments and analyses. I especially thank Regiane Fernandes, who gracefully helped in many characterization analyses.

I acknowledge the CM-UFGM (Centro de Microscopia da UFGM) for providing all the necessary structure for Scanning Electron Microscopy analyses.

I gratefully thank CTNano (Centro de Tecnologia em Nanomateriais e Grafeno) in the person of Cláudia Vasconcelos for providing the ultimate analysis of *Luffa Cylindrica* fibers.

No other person may be so responsible for this work as much as my parents. My father, Joaquim, taught me the incalculable value of education without ever saying a word. My mother, Márcia, taught me dedication and discipline through the labor of several words. With hardship, my grandparents paved the way today I walk with ease. João, my brother, is the one friend closer to me than the distance between our rooms. For my family, I am eternally grateful.

Saving the best for last, I gratefully thank Larissa, the love of my life. She gave me reasons to persevere. A future worth fighting for. She took care of me in the dark days and made my bright ones shine. Thank you, minha menina.

“The Lord has done great things for us, and we are filled with joy.”

Psalm 126:3

RESUMO

Na última década, muitos estudos comprovaram a eficiência das fibras de *Luffa cylindrica* em várias aplicações de adsorção de águas residuais. Porém, uma vez que os contaminantes são removidos da água pelas fibras naturais, um novo resíduo sólido é gerado. Uma ótima alternativa de tratamento para diminuir o impacto ambiental desses resíduos sólidos é o processo de pirólise. Pirólise, a decomposição térmica de compostos orgânicos na ausência de oxigênio em altas temperaturas, foi amplamente desenvolvida como uma plataforma promissora para a produção de combustíveis e produtos químicos a partir de vários tipos de biomassa. Os principais produtos desse processo são biocarvão, bio-óleo e gás de síntese. Embora os produtos voláteis sejam geralmente associados a fins energéticos, alguns biocarvões têm sido amplamente estudados e aplicados com sucesso como materiais adsorventes. Um grande desafio da pirólise de biomassa é a necessidade de aquecer a matéria-prima em altas temperaturas, o que aumenta os custos econômicos e ambientais do processo. Para resolver esse problema, uma alternativa é realizar o aquecimento com energia solar concentrada. Dois pirolisares solares de diferentes designs foram construídos neste trabalho, um com coletor de calha parabólica e o outro com coletor de prato parabólico. Os custos de construção foram de R\$ 10.000 e R\$ 200, respectivamente. Os cálculos de transferência de calor estão disponíveis como resultado deste trabalho. Este projeto de pesquisa estudou a pirólise lenta de *Luffa cylindrica* para a obtenção de biocarvão nos pirolisados solares e em um reator elétrico. Diferentes temperaturas terminais (300, 400 e 500 °C) e taxas de aquecimento (2, 10 e 20 ° C.min⁻¹) foram testadas sob atmosfera de nitrogênio no forno elétrico. O experimento de pirólise solar foi realizado no reator com coletor de prato parabólico sob fluxo de nitrogênio por 1 hora, chegando a temperaturas de até 417 °C. O pirolisador de calha parabólica não foi operacionalizado até a redação deste documento devido a questões técnicas e logísticas. Os biocarvões obtidos foram caracterizados via número de iodo, TG/DTG, FTIR, PCS e MEV. A influência dos parâmetros de pirólise no rendimento, composição, grupos funcionais de superfície, poder calorífico e morfologia dos biocarvões foi estudada e discutida neste trabalho. Todos os biocarvões produzidos e um carvão ativado comercial também foram submetidos a testes de adsorção de iodo para avaliar a influência dos parâmetros do processo no desempenho de adsorção. Os objetivos definidos para este trabalho foram cumpridos, uma vez que os pirolisadores solares propostos foram construídos, a pirólise lenta de *Luffa cylindrica* foi

estudada com detalhes ainda não vistos na literatura e biocarvões com boas propriedades adsorptivas foram obtidos.

Palavras-chave: Pirólise; Energia Solar; Biomassa; Luffa cylindrica; Biocarvão; Adsorção.

ABSTRACT

In the past decade, many studies have proven the efficiency of *Luffa cylindrica* fibers on various wastewater adsorption applications. However, once the contaminants are removed from water by the natural fibers, a new solid waste is generated. A great alternative treatment to diminish the environmental impact of this solid waste is the pyrolysis process. Pyrolysis, the thermal decomposition of organics in the absence of oxygen at high temperatures, has been extensively developed as a promising platform to produce fuels and chemicals from various types of biomass. The main products of this process are biochar, bio-oil, and syngas. While the volatile products are usually linked to energetic purposes, some biochars have been widely studied and successfully applied as adsorbent materials. A major challenge of biomass pyrolysis is the necessity to heat the feedstock to high temperatures, which adds to the economic and environmental costs of the process. To address this matter, an alternative is to perform the heating process using concentrated solar energy. In this work, two solar pyrolyzers of different designs were built, one with a parabolic trough collector and the other with a parabolic dish collector. Their building costs were R\$ 10.000 and R\$ 200, respectively. The thermal transfer calculations for the solar pyrolyzer are available as a result of this project. This research project studied the slow pyrolysis of *Luffa cylindrica* to obtain biochar in electric and solar ensembles. Different terminal temperatures (300, 400, and 500 °C) and heating rates (2, 10, and 20 °C.min⁻¹) were tested under a nitrogen atmosphere in the electric furnace. A solar pyrolysis experiment was performed on the solar dish collector pyrolyzer under nitrogen flux for 1 hour at temperatures up to 417 °C. The parabolic trough pyrolyzer was not operationalized until the writing of this document due to logistics and technical matters. Obtained biochars were characterized via iodine number, TG/DTG, FTIR, HHV, and SEM. The influence of pyrolysis parameters in biochar yield, composition, surface functional groups, morphology, and high heating value was accessed and discussed in this work. All produced biochars and a commercial activated biochar were submitted to iodine adsorption tests to evaluate the influence of process parameters on adsorption performance. The goals set for this work were accomplished since the proposed solar pyrolyzers were built, *Luffa cylindrica* slow pyrolysis was studied with details yet unseen on the literature, and biochars with good adsorptive properties were obtained.

Key words: Pyrolysis; Solar energy; Biomass; *Luffa cylindrica*; Biochar; Adsorption.

FIGURES LIST

Figure 1 - Cellulose, hemicellulose, and lignin in a plant cell structure	5
Figure 2 - Pyrolysis curves of hemicellulose, cellulose, and lignin in TG/DTG	7
Figure 3 - Pyrolysis curves of hemicellulose, cellulose, and lignin in DSC	7
Figure 4 - Cellulose molecular structure	8
Figure 5 - Mechanism of cellulose pyrolysis proposed by Lin <i>et al.</i> (2009).....	10
Figure 6 - Chemical structure of hemicelluloses monomers	11
Figure 7 - The speculative chemical pathways for thermal decomposition of the main chain of Xylan	12
Figure 8 - Basic units of lignin polymer.....	13
Figure 9 - Thermogravimetric analysis of milled wood lignin isolated from Japanese cedar.....	14
Figure 10 - Aromatic substitution and side-chain products from Guaiacyl based lignin.....	15
Figure 11 - Char yield of live plant species on a dry and ash-free basis	16
Figure 12 - Mass yields of products obtained by pyrolyzes with different terminal temperatures: a) biochar, b) bio-oil, c) non-condensable gas	17
Figure 13 - Solar radiation flux density on fine summer and winter days	20
Figure 14 - Schematic of a parabolic trough solar concentrator.....	21
Figure 15 - Schematic of a parabolic dish solar concentrator	21
Figure 16 - Schematic of a heliostat field solar concentrator	22
Figure 17 - Schematic of a linear Fresnel solar concentrator	23
Figure 18 - <i>Luffa cylindrica</i> : a) Plant; b) Early harvested gourd; c) Ripen gourd; d) Luffa sponge	24
Figure 19 - <i>Luffa cylindrica</i> fibers: a) at 10mm macroscopic scale; b) at 0.1 mm scale (cross-section); c) at 0.01 mm scale (cross-section); d) Scanning Electron Microscope micrograph (X400).....	25
Figure 20 - FTIR of raw <i>Luffa cylindrica</i> fibers.....	27

Figure 21 - X-ray diffraction pattern of <i>Luffa cylindrica</i> fibers	29
Figure 22 - XPS spectrum of <i>Luffa Cylindrica</i> fibers: a) Over a binding energy range of 0–1200 eV; b) Deconvolution of C1s peak	30
Figure 23 - TGA/DTG curves of <i>Luffa cylindrica</i> fibers	31
Figure 24 - DSC curve of <i>Luffa cylindrica</i> fibers.....	32
Figure 25 - FTIR spectra of <i>Luffa cylindrica</i> activated biochar prepared by treatment with nitric acid in various concentrations	33
Figure 26 - Fortelab FT 1200 H/V furnace	40
Figure 27 – Schematic of the electrical furnace pyrolysis arrangement (cross-section).....	41
Figure 28 - Assembled parabolic trough solar pyrolyzer	48
Figure 29 - Assembled parabolic dish solar pyrolyzer.....	50
Figure 30 - Biochars obtained from laboratory-scale pyrolysis of <i>Luffa cylindrica</i> at the final temperatures of a) Non pyrolyzed Luffa; b) 300 °C; c) 400 °C; d) 500 °C	51
Figure 31 - <i>Luffa cylindrica</i> biochar yields from electric furnace pyrolysis	52
Figure 32 - Biochar obtained from solar pyrolysis.....	53
Figure 33 - Temperature evolution over the parabolic dish solar pyrolysis.....	54
Figure 34 - TGA/DTG curves of <i>Luffa cylindrica</i> fibers	57
Figure 35 - DTG curves of <i>Luffa cylindrica</i> and <i>Luffa cylindrica</i> biochar from 2 °C/min pyrolysis experiments.....	59
Figure 36 - DTG curves of <i>Luffa cylindrica</i> and <i>Luffa cylindrica</i> biochar from 10 °C/min pyrolysis experiments.....	60
Figure 37 - DTG curves of <i>Luffa cylindrica</i> and <i>Luffa cylindrica</i> biochar from 20 °C/min pyrolysis experiments.....	61
Figure 38 - DTG curves of <i>Luffa cylindrica</i> and <i>Luffa cylindrica</i> solar biochar.	62
Figure 39 - Infrared absorption spectrum of <i>Luffa cylindrica</i>	63
Figure 40 - Infrared absorption spectrum of <i>Luffa cylindrica</i> and <i>Luffa cylindrica</i> biochars from 2°C/min pyrolysis experiments	65

Figure 41 - Infrared absorption spectrum of <i>Luffa cylindrica</i> and <i>Luffa cylindrica</i> biochars from 10 °C/min pyrolysis experiments	67
Figure 42 - Infrared absorption spectrum of <i>Luffa cylindrica</i> and <i>Luffa cylindrica</i> biochars from 20 °C/min pyrolysis experiments	69
Figure 43 - Infrared absorption spectrum of <i>Luffa cylindrica</i> and <i>Luffa cylindrica</i> solar biochar.	71
Figure 44 - HHV of <i>Luffa cylindrica</i> and produced biochars	72
Figure 45 - <i>Luffa cylindrica</i> SEM micrographs: a) Fiber (X 100); b) Fiber surface (X 500); c) Natural fiber tear (X 500); d) Natural fiber tear up close (X 5000); e) Fiber cross-section (X 1000); f) Fiber cross-section up close (X 10000).....	74
Figure 46 - <i>Luffa cylindrica</i> biochar (B400-2): a) X500; b) X1000; c) Cross-section (X2000); d) Cross-section (X10000).....	75
Figure 47 - <i>Luffa cylindrica</i> biochar (B500-2): a) X100; b) X2000; c) Cross-section and surface (X500); d) Cross-section (X5000).....	76
Figure 48 - <i>Luffa cylindrica</i> solar biochar: a) X500; b) X1000; c) Cross-section (X2000); d) Cross-section (X10000).....	77
Figure 49 - Iodine adsorption of produced biochars	78

TABLES LIST

Table 1 - Chemical composition (wt %) of different biomasses from literature	6
Table 2 - Chemical composition (wt %) of <i>Luffa cylindrica</i> fibers from literature	26
Table 3 - Ultimate analysis (wt %) of <i>Luffa cylindrica</i> fibers from literature.....	26
Table 4 - FTIR Peaks of <i>Luffa cylindrica</i> fibers.....	27
Table 5 - BET analyses of <i>Luffa cylindrica</i> biochars pyrolyzed at different temperatures.....	32
Table 6 - Maximum adsorption capacity of some heavy metal ions by <i>Luffa cylindrica</i> biochar.	34
Table 7 - Electric furnace biochar nomenclature.....	41
Table 8 - Calculated convective coefficients and surface temperatures for exposed and insulated cylinders designs and insulated lids of the cylinders.....	46
Table 9 - Calculated heat losses of insulated and exposed cylinders, insulated lid, and the fully assembled reactor	47
Table 10 - Ultimate analysis (wt %) of <i>Luffa cylindrica</i> fibers	55
Table 11 - <i>Luffa cylindrica</i> X-Ray Fluorescence Spectrometry qualitative result.	56
Table 12 - Interpretation of FTIR Peaks of <i>Luffa cylindrica</i> fibers.....	63

ACRONYMS LIST

AGF - 1,6-anhydro-D-glucofuranose
ASTM - American Society for Testing and Materials
BET - Brunauer–Emmett–Teller
BoPET - Biaxially-Oriented Polyethylene Terephthalate
CTNano - Centro de Tecnologia em Nanomateriais
DGP - 6-Dianhydro-R-D-Glucopyranose
DSC - Differential Scanning Calorimetry
DTG - Derivative Thermogravimetric Analysis
EDS - Energy-Dispersive X-Ray Spectroscopy
FTIR - Fourier-Transform Infrared Spectroscopy
HHV - Higher Heating Value
IR – Infrared
LEC - Laboratório de Ensaio de Combustíveis
LGA - Levoglucosan
LGO - Levoglucosenone
pH - Potential of Hydrogen
SEM - Scanning Electron Microscopy
TGA - Thermogravimetric Analysis
UFMG - Universidade Federal de Minas Gerais
XRD - X-Ray Diffraction
XRF - X-Ray Fluorescence

SUMMARY

1 INTRODUCTION.....	1
1.1 RELEVANCE.....	1
1.2 OBJECTIVES	2
2 LITERATURE REVIEW	3
2.1 BIOMASS PYROLYSIS	3
2.1.1 Lignocellulosic Biomass	5
2.1.2 Cellulose Pyrolysis	8
2.1.3 Hemicellulose Pyrolysis	10
2.1.4 Lignin Pyrolysis	12
2.1.5 Pyrolysis Reaction Parameters	15
2.1.6 Solar Pyrolysis	19
2.2 LUFFA CYLINDRICA	23
2.2.1 Characterization of <i>Luffa Cylindrica</i> Fibers	26
2.2.2 <i>Luffa Cylindrica</i> Biochar: Pyrolysis and Adsorption	32
3 METHODOLOGY	36
3.1 DESIGN AND CONSTRUCTION OF TWO SOLAR PYROLYZERS	36
3.2 BIOMASS CHARACTERIZATION	38
3.2.1 Ultimate Analysis	38
3.2.2 X-Ray Fluorescence Spectrometry	38
3.2.3 Thermogravimetric Analysis.....	39
3.2.4 Fourier Transform Infrared Spectroscopy.....	39
3.2.5 Heat of Combustion Analysis	39
3.2.5 Scanning Electron Microscopy	39
3.3 ELECTRIC FURNACE BIOMASS PYROLYSIS	40

3.4 BIOMASS SOLAR PYROLYSIS	41
3.5 BIOCHARS CHARACTERIZATION	42
3.6 IODINE ADSORPTION EXPERIMENTS	42
4 RESULTS AND DISCUSSION	43
4.1 DESIGN AND CONSTRUCTION OF TWO SOLAR PYROLYZERS	43
4.1.1 Parabolic trough solar pyrolizer	43
4.1.1.1 Reactor heat transfer calculations	44
4.1.1.2 Parabolic trough collector design.....	47
4.1.2 Parabolic dish solar pyrolizer.....	49
4.2 ELECTRIC FURNACE BIOMASS PYROLYSIS	50
4.3 SOLAR BIOMASS PYROLYSIS	53
4.4 BIOMASS AND BIOCHAR CHARACTERIZATION.....	54
4.4.1 Ultimate Analysis.....	55
4.4.2 X-Ray Fluorescence Spectrometry	55
4.4.3 Thermogravimetric Analysis.....	56
4.4.4 Fourier Transform Infrared Spectroscopy.....	62
4.4.5 Heat of Combustion Analysis	71
4.4.6 Scanning Electron Microscopy	73
4.5 PRELIMINARY IODINE ADSORPTION EXPERIMENTS	78
5 CONCLUSIONS	79
6 FUTURE WORK SUGGESTIONS	82
REFERENCES	83
APPENDIX	94
APPENDIX A - PARABOLIC TROUGH SOLAR PYROLYZER DESIGN	94
APPENDIX B - CURVED CARBON STEEL SHEET	95

APPENDIX C - MIRROR STRIP	96
APPENDIX D - CYLINDRICAL STAINLESS-STEEL REACTOR	97
APPENDIX E - PARABOLIC TROUGH REACTOR CONVECTIVE COEFFICIENTS.....	98
APPENDIX F - PARABOLIC TROUGH REACTOR HEAT LOSSES	103
APPENDIX G - PARABOLIC DISH REACTOR CONVECTIVE COEFFICIENTS	105
APPENDIX H - PARABOLIC DISH REACTOR FINAL TEMPERATURE	107
APPENDIX I - TGA/DTG CURVES	109
APPENDIX J – LUFFA CYLINDRICA EDS	115

1 INTRODUCTION

1.1 RELEVANCE

Due to the fast-growing consumption pattern of modern societies, there is a strong concern regarding the environmental issues related to human activity. Every industrial process constitutes a potential font of by-products and residues. Waste is a global growing issue linked directly to the way society produces and consumes. If not properly dealt with, waste generation is expected to grow 70 % by 2050, posing a threat to public health and the environment (Glob. Waste Manag. Outlook, 2016; KAZA et al., 2015). Therefore, it is urgent to redesign industrial processes to mitigate the production of wastes, especially environmentally hazardous residues.

The removal of poisonous substances from wastewater has challenged many industrial sectors. Treatment methods such as reduction, precipitation, oxidation, membrane separation processes and ion exchange have been used to remove the contaminants. Nonetheless, when the pollutant is low concentration some techniques are not efficient and in this case adsorption has been used due to its high efficiency and economic aspects (SADEGH et al., 2019).

In the past decade, many studies have proven the efficiency of *Luffa cylindrica* fibers on various wastewater adsorption applications. Great results have been obtained on the adsorption of etheramines from iron ore flotation effluent, phenol, cationic surfactants, cadmium ions, and dyes from diverse industrial wastewaters (ABDELWAHAB; AMIN, 2013; ALTINIŞIK; GÜR; SEKI, 2010; BASTOS et al., 2017; GUPTA et al., 2014; HENINI et al., 2012; LINDINO et al., 2014; SHAHIDI; JALILNEJAD; JALILNEJAD, 2015; YE; HU; WANG, 2013). However, a major concern regarding effluent adsorption systems is the generation of large amounts of contaminated solid residues. It is necessary to establish efficient disposal methodologies for these residues. A promising alternative is to apply pyrolysis to saturated carbonaceous adsorbents.

Pyrolysis, the thermal decomposition of organics in the absence of oxygen, has been extensively developed as a promising platform to produce fuels and chemicals from various types of biomass. Pyrolysis produces biochar, bio-oil, and gas products (WANG et al., 2017). The potential biochar applications include carbon sequestration, soil fertility improvement, pollution remediation, and agricultural by-product/waste recycling. The key process parameters controlling its properties include pyrolysis temperature, residence time, heat transfer rate, and feedstock type (AHMAD et al., 2014).

Luffa cylindrica biochar has emerged as promising adsorbent material for harmful heavy metal ions, such as uranium, copper, thorium, and samarium (LIATSOU et al., 2017a, 2017b; LIATSOU; CHRISTODOULOU; PASHALIDIS, 2018; LIATSOU; CONSTANTINOU; PASHALIDIS, 2017).

A major challenge of biomass pyrolysis is the necessity to heat the feedstock to high temperatures, which adds economic and environmental costs to the process. To address this matter, a promising alternative is to perform the heating process using concentrated solar energy. Solar pyrolysis has the potential to produce higher calorific value products with lower CO₂ emissions than conventional pyrolysis processes. As a consequence, intermittent solar energy is chemically stored in the form of solar fuels (ZENG et al., 2017).

1.2 OBJECTIVES

The primary purpose of this work is to study the pyrolysis of *Luffa cylindrica* fibers (in electrical and solar ensembles) to obtain good adsorbent biochar. As means to reach this global aim, the following specific goals have been established for this research:

- To study *Luffa cylindrica* pyrolysis (process parameters and product characterization);
- To design and assemble two solar pyrolyzers of distinct configurations;
- To study *Luffa cylindrica* solar pyrolysis;

- To evaluate the adsorption performance of *Luffa cylindrica* biochars through iodine adsorption experiments.

2 LITERATURE REVIEW

2.1 BIOMASS PYROLYSIS

The word pyrolysis is coined from two ancient Greek words: “pyro” (πυρο), which means fire, and “lysis” (λύσις), which means breaking or separation. Thus, pyrolysis means breaking or separating through thermal energy. Similarly, several other molecular breakdown processes have names that come from the same Greek root, including electrolysis, breakdown by electricity, hydrolysis, breakdown by water, and photolysis, breakdown by excitation by light radiation.

The carbonization of biomass traces back to the beginnings of recorded human history, when producing char was the sole objective of wood pyrolysis (FAHMY et al., 2020). Ancient Egyptians performed the pyrolysis process to obtain tar for sealing wooden boats against water and rot and pyrolytic liquid products, such as fluid wood-tar and pyroligneous acid to embalm their dead (GARCIA-NUNEZ et al., 2017; MOHAN; PITTMAN; PHILIP, 2017). At the end of the eighteenth century, technologies to recover and utilize the condensable pyrolysis products were relatively well developed. In the 19th century the “acid-wood industry”, also known as the “wood distillation industry” was established to produce charcoal and liquid by-products (e.g. acetic acid, methanol, and acetone) (GARCIA-NUNEZ et al., 2017).

Pyrolysis, the thermal decomposition occurring in the absence of oxygen, has been extensively developed as a promising platform to produce fuels and chemicals from various types of biomass (BRIDGWATER, 2011). Biomass is the generic term for plant (phytomass) and animal (zoomass) matter. Lignocellulosic biomass refers to dry plant matter, which is an abundant and low-cost source of renewable energy (DHYANI; BHASKAR, 2018). Biomass resources are vastly abundant in nature. Global biomass production is estimated to be around 100 billion tons per year (SHELDON, 2014). As the only renewable carbonaceous resource, biomass

has the potential to produce heat, electricity, fuel, chemicals, and other products (LI et al., 2018; SHYLESH et al., 2017).

Heating of biomass in inert atmosphere results in the production of organic vapor composed of depolymerized fragments of cellulose, hemicellulose, and lignin polymers found in the biomass. These vapors can be condensed to give a free-flowing organic liquid, commonly known as bio-oil. The noncondensable gases leave the reaction system and can be used to provide heat for pyrolysis. The remaining carbon-rich residual is left as bio-char (DHYANI; BHASKAR, 2018). The distribution of pyrolysis products strongly depends on the reaction conditions and the biomass feedstock (WANG et al., 2017).

During the biomass pyrolysis, a large number of reactions take place in parallel and series, including dehydration, depolymerization, isomerization, aromatization, decarboxylation, and charring (BRIDGWATER, 2011; FAHMY et al., 2020; MOHAN; PITTMAN; PHILIP, 2017). It is generally accepted that the pyrolysis of biomass consists of three main stages: (i) initial evaporation of free moisture, (ii) primary decomposition, and (iii) secondary reactions, which embody oil cracking and repolymerization (WANG et al., 2017). These stages are intermingled, with a possibility to observe their transitional behavior through thermal analysis.

Depending on the heating rate and solid residence time, biomass pyrolysis can be divided into three main types including slow (conventional) pyrolysis, fast pyrolysis, and flash pyrolysis. Some other pyrolysis processes may also be conducted between these typical pyrolysis types (MOHAN; PITTMAN; PHILIP, 2017). Slow pyrolysis, also known as carbonization, is the method traditionally applied to obtain high proportions of charcoal. The thermal decomposition of biomass under a very low heating rate allows sufficient time for repolymerization reactions maximizing the solid yields (KAN; STREZOV; EVANS, 2016). Therefore, it presents a long residence time, ranging from minutes to days, and it does not require fine biomass feedstock particle sizes. Fast pyrolysis, on the other hand, typically involves high heating rates (hundreds of Celsius degrees per second) and short residence times (0.5–10 s, usually around 2 s). Bio-oil yield can be as high as 50 - 70 wt % (HEIDARI et al., 2019). Finally, the flash pyrolysis process

is characterized by higher heating rates higher than 1000 °C/s and residence time up to 0.5 s resulting in very high bio-oil yields which can achieve up to 75–80 wt % (NZIHOU et al., 2019).

2.1.1 Lignocellulosic Biomass

Lignocellulosic biomass is composed of three major components, cellulose, hemicellulose, and lignin (NZIHOU et al., 2019). Other than these three components, biomass also comprises some extractives and inorganic components. Extractives include alkaloids, essential oils, fats, glycosides, gums, mucilages, pectins, and other chemicals, while the most common ashes are potassium, calcium, sodium, silicon, phosphorus, and chlorines (DHYANI; BHASKAR, 2018). The main load-bearing component of plant walls is cellulose. Plant cells are surrounded by layers of long cellulose fibers that are hydrogen-bonded to form an insoluble and inelastic crystalline material (VORWERK; SOMERVILLE; SOMERVILLE, 2004). As illustrated in Figure 1, the cellulose fibrils are interconnected with high molecular weight hemicellulose molecules that are hydrogen-bonded to the surface of the cellulose microfibrils, and the inner space is packed with lignin linking material (DHYANI; BHASKAR, 2018; VORWERK; SOMERVILLE; SOMERVILLE, 2004; WANG et al., 2017).

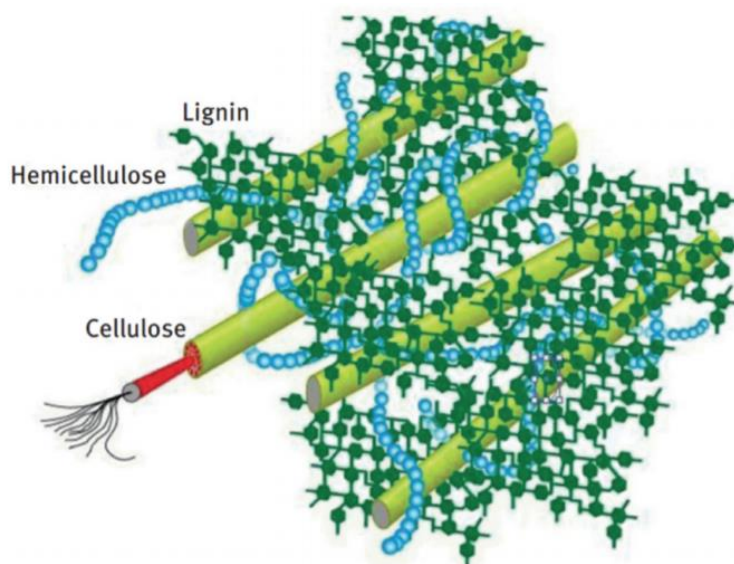


Figure 1 - Cellulose, hemicellulose, and lignin in a plant cell structure (WANG; LUO, 2016).

The content of these components in biomass varies depending on the biomass type (STEFANIDIS et al., 2014). As shown in Table 1, *Luffa cylindrica* biomass presents an exceptional amount of cellulose when compared to herbaceous and wood biomass. It also possesses an especially low content of extractives and ashes.

Table 1 - Chemical composition (wt %) of different biomasses from literature.

Biomass	Cellulose	Hemicellulose	Lignin	Extractives	Ashes	Reference
<i>Luffa cylindrica</i>	63.0	19.4	11.2	3.2	0.4	(TANOBE et al., 2005)
Rice husk	37.00	23.43	24.77	3.19	17.27	(RABEMANOLONTSOA; SAKA, 2013)
Corn straw	42.7	23.2	17.5	9.8	6.8	(QU et al., 2011)
Wheat straw	37.55	18.22	20.24	4.05	3.74	(RABEMANOLONTSOA; SAKA, 2013)
Bamboo	39.80	19.49	20.81	6.77	1.21	(RABEMANOLONTSOA; SAKA, 2013)
Spruce	45.6	20.0	28.2	5.9	0.3	(TAHERZADEH et al., 1997)
Japanese Cedar	38.6	23.1	33.8	4.0	0.3	(RABEMANOLONTSOA; SAKA, 2013)
Alder	45.5	20.6	23.3	9.8	0.7	(TAHERZADEH et al., 1997)
Cherry Wood	46	29	18	6.3	0.5	(DI BLASI; BRANCA; GALGANO, 2010)
Poplar	49	24	20	5.9	1	(DI BLASI; BRANCA; GALGANO, 2010)

Stefanidis *et al.* (2014) studied the characteristics of cellulose, xylan (hemicellulose), and lignin pyrolysis (STEFANIDIS et al., 2014). Great differences in the pyrolysis behavior among the three main components were drawn from the experimental results. As it can be seen in the TG/DTG curves portrayed in Figure 2, hemicellulose was easily degraded, and its pyrolysis was focused at 220–320 °C. The pyrolysis of cellulose mainly happened at 300-370 °C, while that of lignin covered a whole temperature range (200–800 °C) (STEFANIDIS et al., 2014).

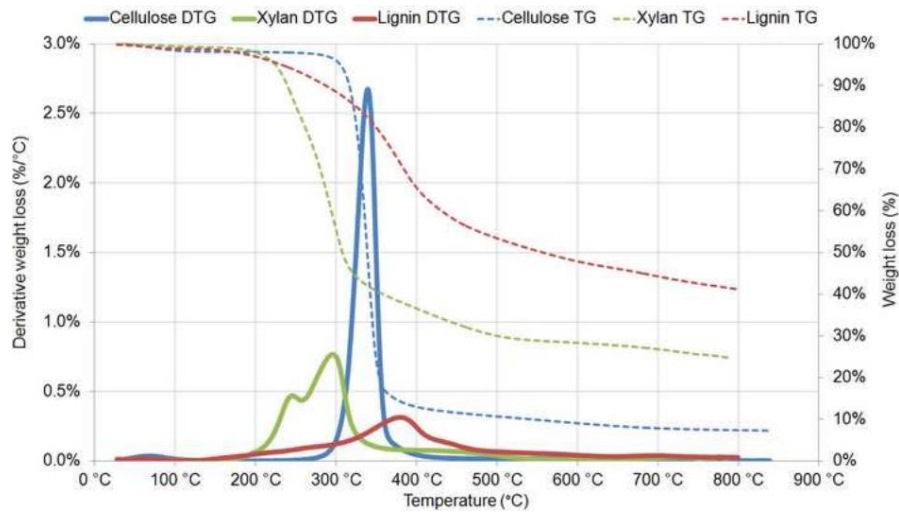


Figure 2 - Pyrolysis curves of hemicellulose, cellulose, and lignin in TG/DTG(STEFANIDIS et al., 2014).

Yang *et al.* (2007) published Differential Scanning Calorimetry (DSC) curves of the pyrolysis reactions of the three main components of lignocellulosic biomass (Figure 3) (YANG et al., 2007). At low temperatures (<500 °C), the pyrolysis of hemicellulose and lignin involved exothermic reactions while those of cellulose were endothermic. However, at high temperatures (>500 °C), the situation just changed inversely (YANG et al., 2007).

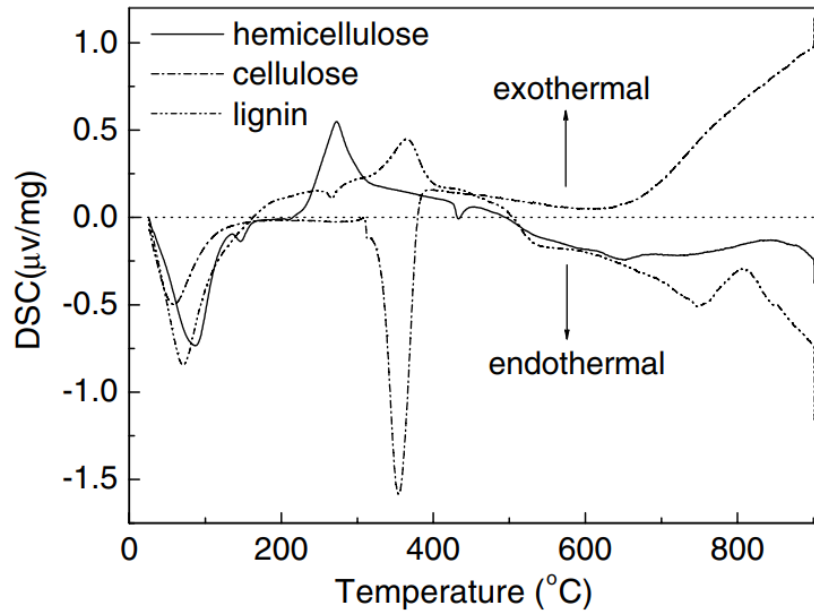


Figure 3 - Pyrolysis curves of hemicellulose, cellulose, and lignin in DSC (YANG et al., 2007).

2.1.2 Cellulose Pyrolysis

Among the various raw materials which are available in nature for industrial purposes, cellulose has indubitably occupied a prominent position. Its abundance is attributed to the constant photosynthetic cycles taking place in higher plants, which can synthesize around $10^{11} \pm 10^{12}$ tons of cellulose in a rather pure form (KUMAR GUPTA et al., 2019). Cellulose is the most abundant biopolymer available in nature (KHANDELWAL; WINDLE, 2013).

Cellulose is a linear homopolymer macromolecular polysaccharide that consists of a long chain of glucose units linked by β 1,4-glycosidic bonds (WANG et al., 2017). The molecular structure, represented in Figure 4, is responsible for its significant properties: Chirality, hydrophilicity, degradability, and chemical variability due to high reactivity from the donor group OH. The superior hydrogen bonds add a crystalline fiber structure to cellulose (KUMAR GUPTA et al., 2019).

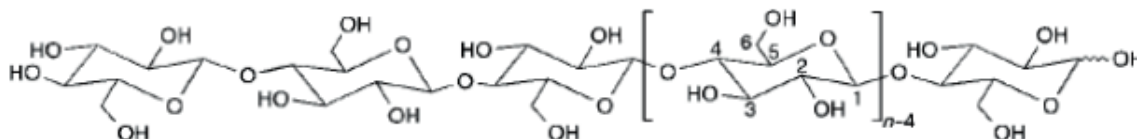


Figure 4 - Cellulose molecular structure ($n = DP$, degree of polymerization)(NOBLES; ROMANOVICZ; BROWN, 2001).

Stefanidis *et al* (2014) performed the pyrolysis of isolated cellulose (Figure 2). In the experiments, cellulose was decomposed over a narrow temperature range, between 280 °C and 360 °C. The highest decomposition rate was observed at 339 °C and the total contents of solid residue at 500 °C and 800 °C were 10.7 and 7.4 wt %, respectively (STEFANIDIS et al., 2014).

The glycosidic bonds linking the glucose units in cellulose are not strong and tend to break under severe thermochemical conditions. Therefore, the cellulose structure degrades intensely during the initial pyrolysis stages with the reduction of the degree of polymerization, which, for woody fibers, may average around 10,000, but may be as high as 15,000 (WANG et

al., 2017). The cleavage of β 1,4-glycosidic bonds contributes strongly to the formation of furans and levoglucosan (LGA) (WU et al., 2016).

Lin *et al.* (2009) have proposed a reaction mechanism for cellulose pyrolysis (Figure 5) (LIN et al., 2009). In the study, cellulose was initially decomposed to the oligosaccharides having relatively lower molecular units and continued to complete the chain breaks until it was reached the sugar level. The first resulting anhydro-monosaccharide was levoglucosan (LGA). LGA can undergo dehydration and isomerization reactions to form other anhydro-monosaccharides such as 1,4:3,6-dianhydro-R-D-glucopyranose (DGP), levoglucosenone (LGO), and 1,6-anhydro--D-glucofuranose (AGF). These anhydro-monosaccharides could either be repolymerized to form anhydro-oligomers or further be transformed by fragmentation, condensation, dehydration, decarbonylation, or decarboxylation. The resulting chemical species from these processes are hydroxyacetaldehyde, hydroxyacetone, and glyceraldehyde, from fragmentation, water, and furanoses (furfural, hydroxymethylfurfural HMF, etc.) from dehydration. CO and CO₂ are generated by a very complex series of reactions that probably involve decarbonylation and decarboxylation, respectively. All the products may be further converted to form char (except CO and CO₂) or be converted into light gases, such as H₂ and CH₄ (LIN et al., 2009).

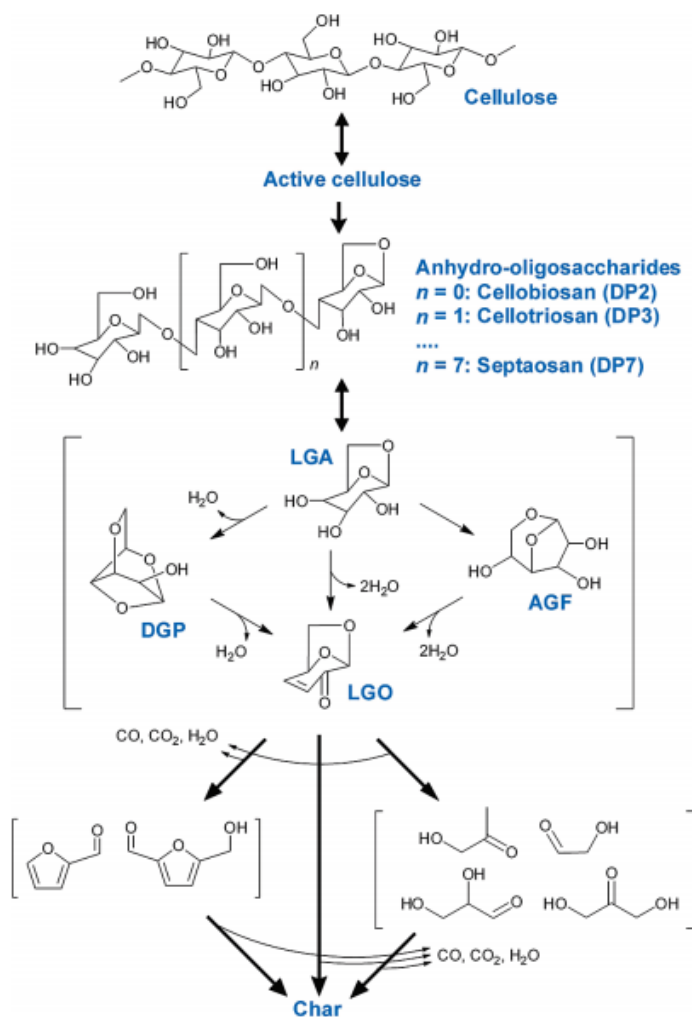


Figure 5 - Mechanism of cellulose pyrolysis proposed by Lin *et al.* (2009) (LIN *et al.*, 2009).

2.1.3 Hemicellulose Pyrolysis

Hemicelluloses are the second most abundant polysaccharide in plants, comprising a wide variety of monosaccharides. They are low molecular weight branched amorphous heteropolymers with degrees of polymerization ranging from 80 to 200 (PENG *et al.*, 2012). The main hemicelluloses present in lignocellulosic biomass are glucuronoxylans (main hemicelluloses of hardwoods), galactoglucomannans (main hemicelluloses of softwoods), xyloglucans, arabinoxylans, arabinoglucuronoxylans (GÍRIO *et al.*, 2010; PENG *et al.*, 2012). These polysaccharides may have different characteristics due to different monomeric compositions,

degrees of polymerization, and chain structure. The monosaccharide units constituting hemicellulose include mainly hexoses (glucose, mannose, and galactose) and pentoses (xylose and arabinose), as well as some other low-content saccharides (rhamnose and fructose). In addition, there are some uronic acids (4-O-methyl-d-glucuronic acid, d-glucuronic acid, and d-galacturonic acid) and acetyl groups in the hemicellulose structure (WANG et al., 2017). The structures of these monomers are shown in Figure 6.

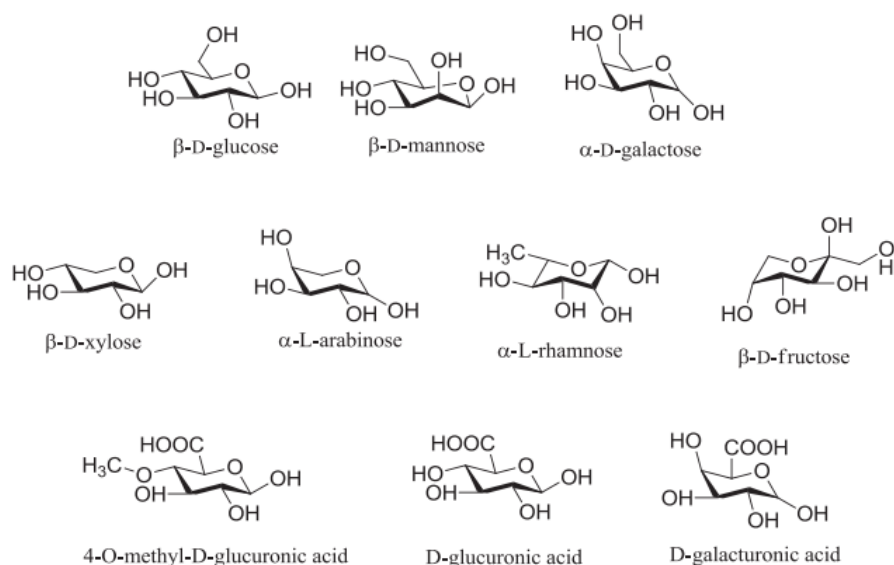


Figure 6 - Chemical structure of hemicelluloses monomers(WANG et al., 2017).

Stefanidis *et al.* (2014) performed the pyrolysis of isolated xylan (Figure 2), which is considered to be an adequate replacement for hemicellulose and it is widely used in the literature for this purpose since xylans are the main hemicellulose components of secondary cell walls, constituting about 20–30% of the biomass of hardwoods and herbaceous plants (GÍRIO et al., 2010; PENG et al., 2012; STEFANIDIS et al., 2014). In Stefanidis's experiment, xylan decomposed at low temperatures and a wide temperature range, between 200 °C and 320 °C, with two distinct peaks; one at 246 °C and another at 295 °C. The low decomposition temperature range of xylan was attributed to its structure, which is amorphous with branched units that have low degradation activation energy (STEFANIDIS et al., 2014).

Shen, Gu, and Bridgwater (2010) (SHEN; GU; BRIDGWATER, 2010) proposed the xylan-based hemicellulose pyrolysis pathway illustrated in Figure 7. The mechanism presents that the formation of 1,4-anhydro-D-xylopyranose is mainly attributed to the cleavage of the glycosidic linkage of the xylan chain, followed by the rearrangement of the depolymerized molecules. Due to the instability of the 1,4 intramolecular glycosidic bonds on the xylopyranose, most of the produced 1,4-anhydro-D-xylopyranose is instantly consumed to produce the two-carbon, three-carbon fragments and gases through the pathways (2), (3), (4), (5), and (6) in Figure 7, acting as an intermediate product from the hemicellulose pyrolysis. Shen, Gu, and Bridgwater (2010) also proposed a new chemical pathway for the production of furfural: A ring-opening reaction of the depolymerized xylan unit through the cleavage of the hemiacetal bond (between oxygen and C-1 on the pyran-ring), followed by the dehydration between the hydroxyl groups on C2 and C5 position (pathway (4) → (8) in Figure 7) (SHEN; GU; BRIDGWATER, 2010).

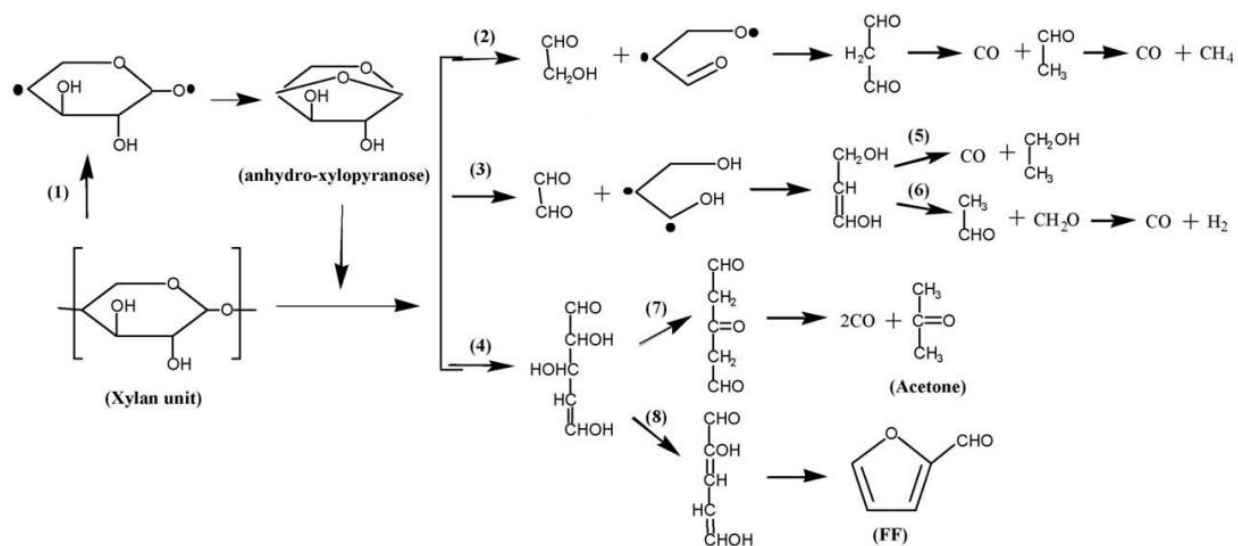


Figure 7 - The speculative chemical pathways for thermal decomposition of the main chain of Xylan (SHEN; GU; BRIDGWATER, 2010).

2.1.4 Lignin Pyrolysis

Lignin, a valuable resource for chemicals and energy, is the most abundant natural aromatic polymer (LEISOLA; PASTINEN; AXE, 2012). As a major by-product of the paper industry, lignin is most often used as fuel in paper industry. However, due to the very large

generated quantities, lignin is increasingly considered as a potential source of chemicals, and studies on its thermal degradation has received much interest (PONNUSAMY et al., 2019).

Lignin has a highly branched three-dimensional phenolic structure including three main phenylpropane units, namely p-hydroxyphenyl, guaiacyl, syringyl (Figure 8) (PONNUSAMY et al., 2019; RALPH; LAPIERRE; BOERJAN, 2019). The linkages of basic lignin units are complex and can be divided into two classes: carbon-carbon bonds (30-40%) and carbon-oxygen (ether and ester) bonds (60-70%) (WANG et al., 2017). The composition and amount of lignin vary from species to species, tree to tree, and even in woods from different parts of the same tree (RALPH; LAPIERRE; BOERJAN, 2019). Softwoods are known to contain higher contents of lignin, followed by hardwoods and grasses (LEISOLA; PASTINEN; AXE, 2012).

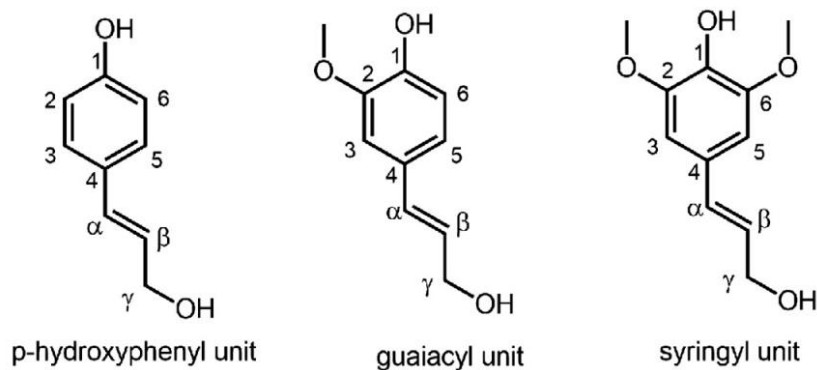


Figure 8 - Basic units of lignin polymer (WANG et al., 2017).

Kawamoto (2014) described the pyrolysis reactions of isolated lignin (KAWAMOTO, 2017). As reported in the study and illustrated in Figure 9, thermogravimetric analysis (TG) of lignin shows several derivative (DTG) peaks at 350 °C from primary pyrolysis reactions and 400–450 °C and 550–600 °C from secondary pyrolysis reactions (KAWAMOTO, 2017).

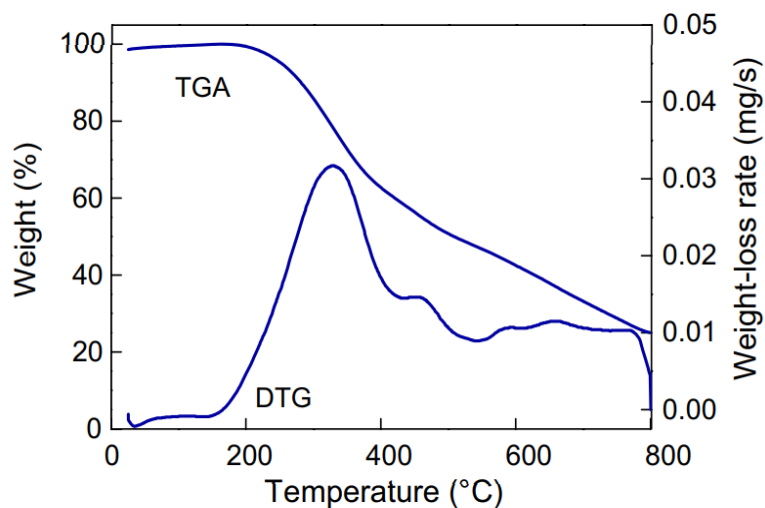


Figure 9 - Thermogravimetric analysis of milled wood lignin isolated from Japanese cedar (KAWAMOTO, 2017).

According to Kawamoto (2014), in the first stage of lignin pyrolysis, lignin macromolecules undergo a depolymerization process, especially by the linkage of ether bonds. Condensed (C–C) type linkages are stable during depolymerization of lignin macromolecules, therefore biomass with a higher proportion of condensed linkage tends to generate larger amounts of residue (ASMADI; KAWAMOTO; SAKA, 2011; KAWAMOTO, 2017; NAKAMURA; KAWAMOTO; SAKA, 2008). The aromatic compounds produced during the primary pyrolysis stage are predominantly guaiacols from guaiacyl-based lignins (Figure 10) and syringols from syringyl-based lignins, while the majority of side-chain products are unsaturated alkyl groups (NAKAMURA; KAWAMOTO; SAKA, 2008). Some volatile products from guaiacyl-based lignins in this stage include coniferyl alcohol, coniferyl aldehyde, isoeugenol, 4-vinylguaiacol, vanillin, acetovanillone, and dihydroconiferyl alcohol (KAWAMOTO, 2017).

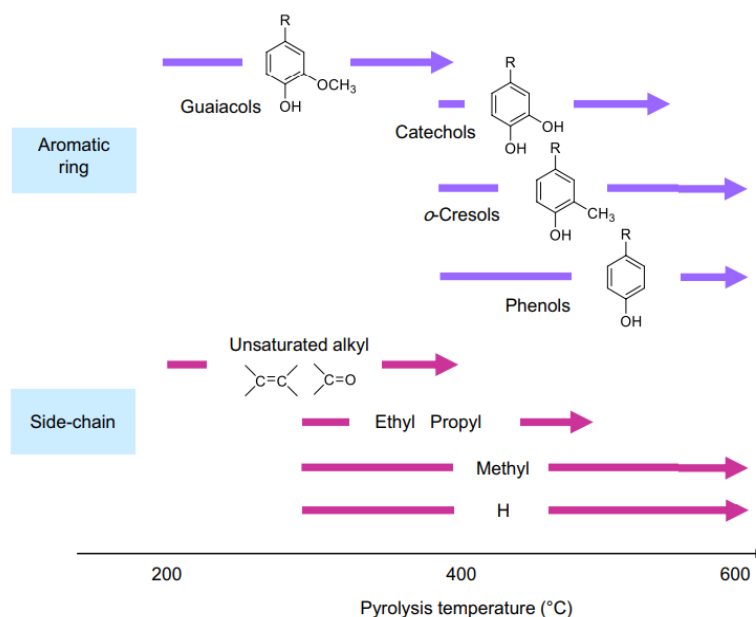


Figure 10 - Aromatic substitution and side-chain products from Guaiacyl based lignin (KAWAMOTO, 2017).

When the pyrolysis temperature is increased to 400–450 °C, secondary pyrolysis reactions take place and guaiacols/syringols rapidly transition to catechols and o-cresols along with phenols (Figure 10) (BREBU; VASILE, 2010). In this temperature range, cracking of side-chain C–C bonds occurs, which increases the yields of monomers (ASMADI; KAWAMOTO; SAKA, 2011; SHEN et al., 2010a; WANG et al., 2017). The reaction products transition from unsaturated to saturated alkyl side-chains and non-substituted (–H) types. Coke and polycyclic aromatic hydrocarbons (PAHs) formation also start. Around 550 °C, catechols and non-condensable gas yields (particularly CO) significantly increase. At temperatures >700 °C, the formation of PAHs is enhanced. Phenols and o-cresols are relatively stable at such high temperatures; hence, these compounds are observed along with PAHs even during high-temperature pyrolysis (KAWAMOTO, 2017).

2.1.5 Pyrolysis Reaction Parameters

Reaction conditions are crucial for the pyrolysis process. Biochar production through pyrolysis is influenced by process parameters like temperature, heating rate, residence time,

particle size, and others. These operating parameters not only control the char yield but also affect the properties of the pyrolysis products (TRIPATHI; SAHU; GANESAN, 2016).

Heating rate is one of the most fundamental parameters in pyrolysis processes, as it defines the type of pyrolysis: flash, fast, or slow pyrolysis. At low heating rates, the possibility of secondary pyrolysis reactions, such as those of repolymerization, is enhanced (AKHTAR; SAIDINA AMIN, 2012). Fast heating rates favor quick fragmentation of the biomass and yield more gases and produce less char (KAN; STREZOV; EVANS, 2016). Safdari *et al* (2019) performed fast and slow pyrolysis, $100^{\circ}\text{C}\cdot\text{min}^{-1}$ and $0.5^{\circ}\text{C}\cdot\text{min}^{-1}$, respectively, of a series of lignocellulosic biomass feedstock (SAFDARI et al., 2019). Slow pyrolysis presented invariably a greater char yield, lower bio-oil yield, and slightly lower gas product proportion (Figure 11).

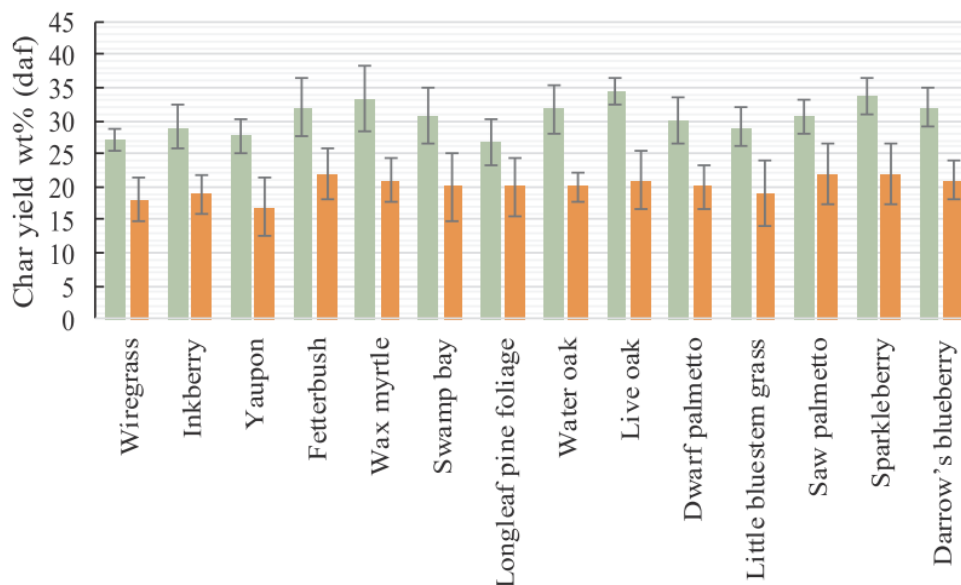


Figure 11 - Char yield of live plant species on a dry and ash-free basis (SAFDARI et al., 2019).

Chen *et al* (2016) studied the influence of heating rate and temperature on the pyrolysis of poplar wood biomass (CHEN et al., 2016). Pyrolysis reactions were performed at 10, 30, and $50^{\circ}\text{C}\cdot\text{min}^{-1}$ and temperatures ranging from 400 to 600°C (Figure 12). Higher char and lower bio-oil yields were obtained at lower heating rates, while the effect of the heating rate was insignificant on the mass yield of the non-condensable gas.

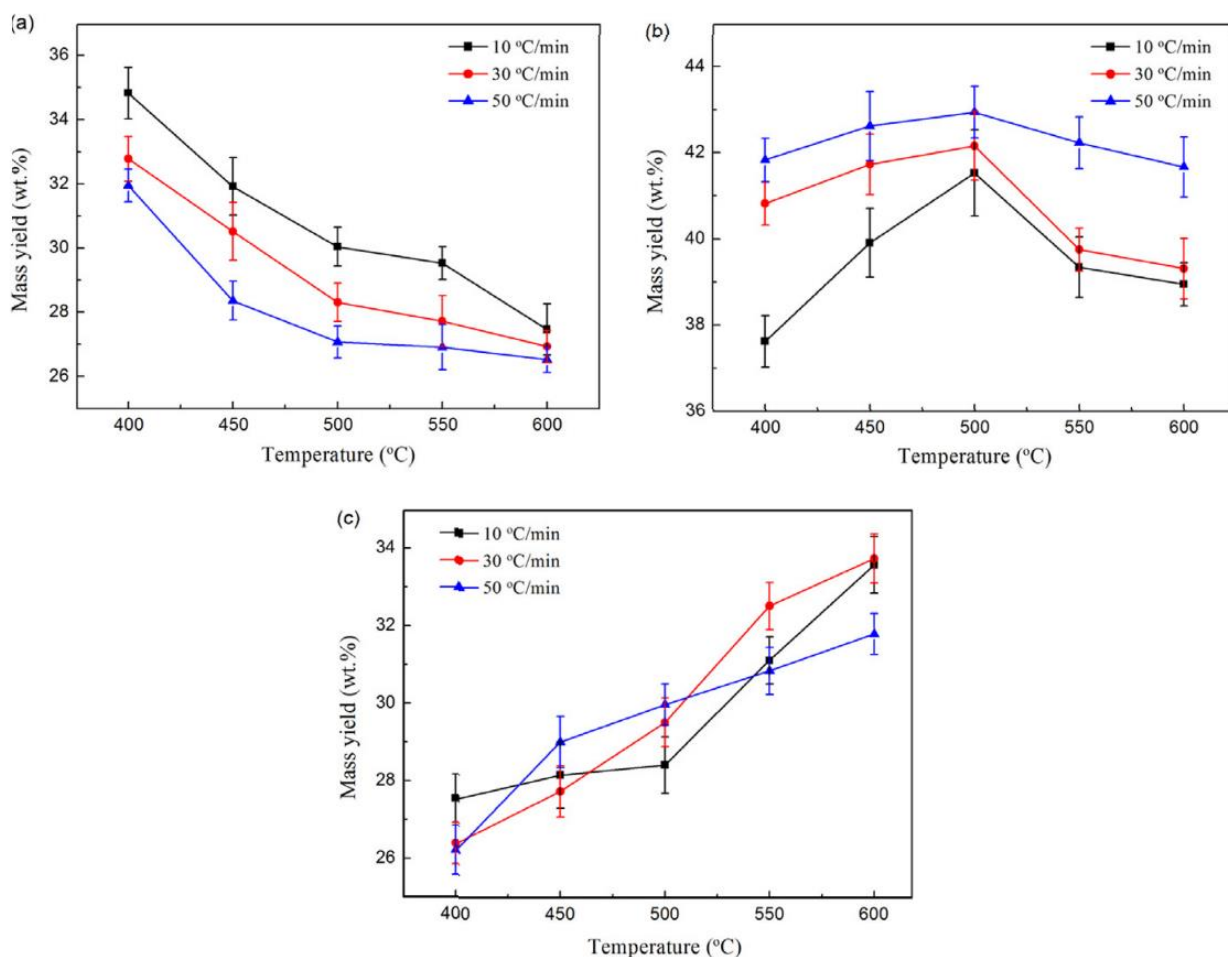


Figure 12 - Mass yields of products obtained by pyrolyzes with different terminal temperatures: (a) biochar, (b) bio-oil, (c) non-condensable gas (CHEN et al., 2016).

Pyrolysis temperature significantly influences the distribution and properties of products. The basic role of high-temperature application in the pyrolysis reaction is to provide the necessary heat for the decomposition of biomass through chemical bonds cleavage (GUEDES; LUNA; TORRES, 2018). At low temperatures (<300 °C), decomposition mainly occurs at heteroatom sites within biomass structure which results in the production of heavy tars. While at high temperature (>550 °C), massive fragmentation of biomass species causes extremely high molecular disordering which results in the production of numerous types of compounds (AKHTAR; SAIDINA AMIN, 2012). Therefore, raising the temperature in pyrolysis affects the biochar yield negatively, as it allows the thermal cracking of heavy hydrocarbon materials, leading to the increase of liquid and gaseous and a decrease in the biochar yield (TRIPATHI;

SAHU; GANESAN, 2016). Generally, the bio-oil yields reach their peak concentrations at temperatures between 400 and 550 °C and then decline after proceeding with heating due to the dominant secondary cracking reactions that produce non-condensable gases (KAN; STREZOV; EVANS, 2016).

During the pyrolysis process of the biomass, a significant amount of vapor is formed. The pyrolysis vapor can suffer secondary reactions of thermal cracking, repolymerization, and recondensation of the char residue, which leads to a decrease in bio-oil yield and increases solid and gas production (GUEDES; LUNA; TORRES, 2018). Low temperatures associated with long vapor residence times are required for higher biochar production (AKHTAR; SAIDINA AMIN, 2012). Increasing the vapor residence time helps the repolymerization of the biomass constituents by giving them sufficient time to react. While if the residence time is shorter, repolymerization of the biomass constituents does not get completed and biochar yield is reduced (PARK; PARK; KIM, 2008).

The reaction atmosphere is another important factor that influences the pyrolysis process and products. The use of inert gases such as N₂ (the most used due to its cheapness) is common practice for the rapid purging of hot pyrolysis vapors. However, literature shows that different outcomes regarding product composition and properties may be achieved by using other purge gases, such as CO₂, CH₄, and H₂ (GUIZANI; ESCUDERO SANZ; SALVADOR, 2014; ZHANG et al., 2011). For example, the char obtained by Guizani *et al* (2014) in the CO₂ atmosphere had increased surface area and different chemical composition compared to the char produced under nitrogen atmosphere.

Biochar yield is increased when the pyrolysis is completed under the influence of high pressure (MANYÀ et al., 2014). An increase in pressure favors effective collisions, resulting in more extensive secondary cracking and repolymerization reactions (TRIPATHI; SAHU; GANESAN, 2016). Vacuum pyrolysis, on the other hand, favors rapid withdrawal of volatile pyrolytic products, which reduces secondary reactions. This method decreases the yield of the

solid product, but increases biochar porosity and develops several porous structures (URAS et al., 2012).

Another substantially important pyrolysis parameter is biomass particle size. Biomass is a poor heat conductor (GUEDES; LUNA; TORRES, 2018). Thus, the greater the particle size, the distance between the biomass surface and its core increases, which retards the rapid heat flow from the hot to cold end (SURIAPPARAO; VINU, 2018). As lower temperatures favor biochar yields, greater particle size is usually desirable when the solids are the product of interest (YU et al., 2018). Also on increasing the particle size the vapor formed in the inner layers during the thermal cracking of biomass has to diffuse greater distances through the char fibers, causing more secondary reactions and resulting in the formation of more amounts of char (TRIPATHI; SAHU; GANESAN, 2016).

2.1.6 Solar Pyrolysis

The growing demand for alternative energy sources is driving not only the investigation of new and renewable alternative feedstocks but also clean production mechanisms. The application of solar energy for biomass pyrolysis is a promising technology for converting biomass to energy, fuels, and other chemical substances with neutral CO₂ emissions. Compared to the conventional pyrolysis process, the biomass conversion efficiency can be greatly improved if the pyrolysis heat is supplied from a concentrated solar system which can be achieved at reasonably moderate solar radiations (WELDEKIDAN et al., 2018).

The main challenge for the usage of solar energy as a heat source for chemical processes is the need to increase the solar radiation flux density (Figure 13) given the dilution of terrestrial solar radiation (ZENG et al., 2017). Optical reflective concentration devices, such as parabolic troughs, parabolic dishes, heliostat fields, and linear Fresnel reflectors have been successfully used to focus incident solar radiation on surfaces that are much smaller than the collection surfaces of the mirrors (FERNÁNDEZ-GARCÍA et al., 2010; KAYHAN, 2018; SAXE et al., 2019; ZENG et al., 2017).

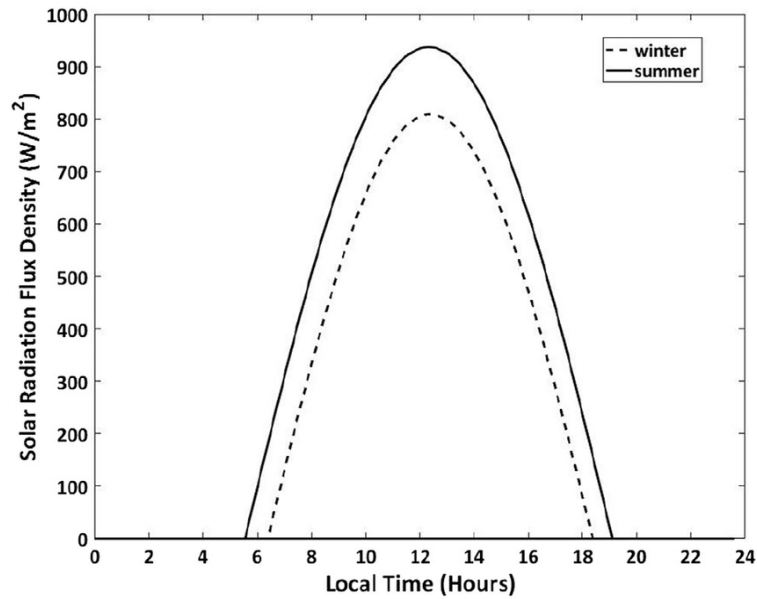


Figure 13 - Solar radiation flux density on fine summer and winter days (KAYHAN, 2018).

A parabolic trough (Figure 14) is a type of solar radiation concentrator which is straight in one dimension and curved as a parabola in the other two (WELDEKIDAN et al., 2018). The concave side is coated with a highly reflective material, so solar radiation is reflected onto a linear receiver placed at the concentrator's focal line (FERNÁNDEZ-GARCÍA et al., 2010). The pyrolysis reactor is placed at this linear focal point of the parabolic trough. Typically, a reactor made from a metal of high thermal conductivity can reach working temperatures of over 400 °C, and the concentration ratio (ratio between the concentrator opening area and the aperture area that receives) of 30–100 (JOARDDER et al., 2017). The parabolic trough linear focus is an advantage for continuous process applications, once it enables the use of tubular reactors.

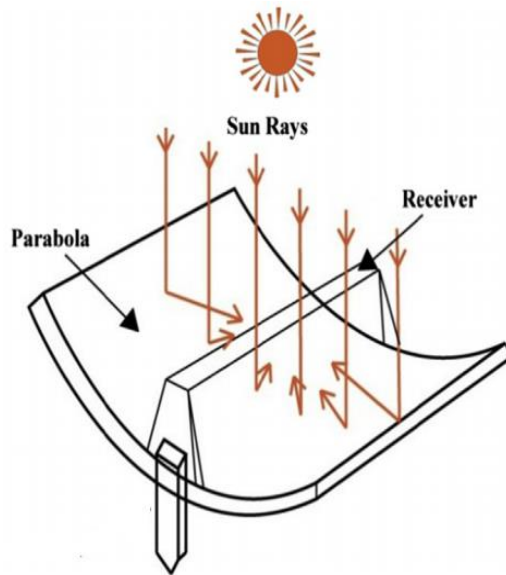


Figure 14 - Schematic of a parabolic trough solar concentrator (KODAMA, 2003).

A parabolic dish is a surface generated by a parabola revolving around its axis. Parabolic dish solar concentrators (Figure 15) are systems that make use of this geometry to concentrate solar radiation toward the thermal receiver located on the focal point of the dish collector (JOARDDER et al., 2017). The operating temperature of the systems is up to 2000 °C while the concentration ratio typically is in the range of 500 to 2000 (WELDEKIDAN et al., 2018). Given that parabolic dish concentrators present a focal point, rather than a focal line, they are more suited to batch processes, thus limiting their application.

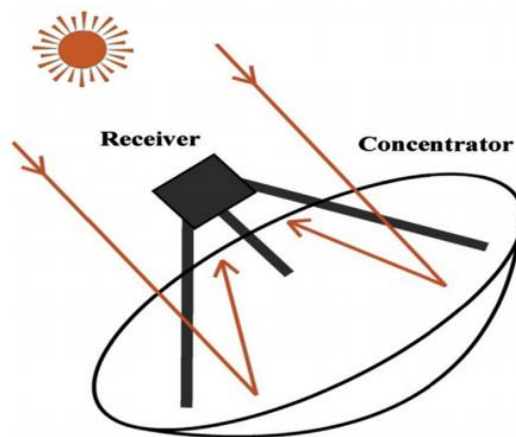


Figure 15 - Schematic of a parabolic dish solar concentrator (KODAMA, 2003).

Heliostat field solar concentrating systems (Figure 16) are focal point collectors that consist of a large array of mirrors, heliostats, which reflect the directly incident solar rays toward the receiver located on a central tower (PITZ-PAAL; BOTERO; STEINFELD, 2011). These systems usually achieve temperatures up to 1250°C and concentration ratios of 300-1500 (JOARDDER et al., 2017). Heliostat field solar systems are suitable for large-scale applications, such as power plants (ZHANG et al., 2013).

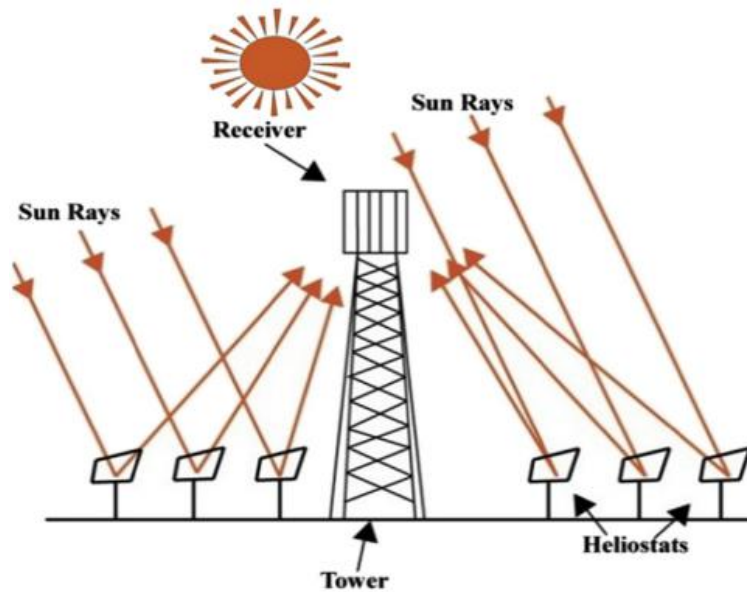


Figure 16 - Schematic of a heliostat field solar concentrator(KODAMA, 2003).

Linear Fresnel collectors (Figure 17) utilize an array of low-profile, flat, or nearly flat primary reflectors and a fixed receiver assembly that includes one or more linear receiver tubes and an optional secondary reflector (ZHU et al., 2014). Linear Fresnel systems may achieve temperatures up to 150°C (300 °C if a secondary reflector is used) and concentration ratios around 30 (WELDEKIDAN et al., 2018). As this approach presents tubular receivers in the focal line, continuous plug flow reactors may be used. However, the low-temperature range of linear Fresnel collectors limits the possible applications.

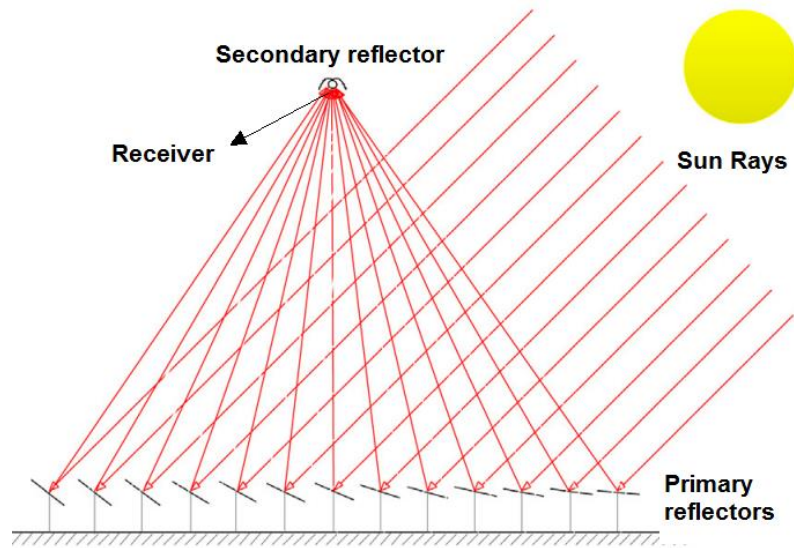


Figure 17 - Schematic of a linear Fresnel concentrator(ZHU, 2013).

2.2 LUFFA CYLINDRICA

Luffa cylindrica commonly called sponge gourd, loofah, vegetable sponge, bath sponge, or dishcloth gourd, is a member of the Cucurbitaceae family commonly found in Asia, Africa, Central and South America (OBOH; ALUYOR, 2009; PARTAP et al., 2012; SILVA; RANIL; FONSEKA, 2015). Apart from Africa, Brazil is the largest producer and also an exploiter of these sponges (SATYANARAYANA; GUIMARÃES; WYPYCH, 2007).

Luffa cylindrica (Figure 18-a) is a herbaceous creeper, whose length may reach 10 meters or more, usually cultivated for its fruit, a 15 - 25 cm to 1.20 - 1.50 m long, oblong cylindrical, green smooth, with numerous black, gray, or medium brown spots on their skin (BASTOS, 2018; SATYANARAYANA; GUIMARÃES; WYPYCH, 2007; TANOBE et al., 2005). Luffa gourd, when harvested early (Figure 18-b), is an edible vegetable, but as the fruit ripens, it becomes fibrous (Figure 18-c). The sponge (Figure 18-d) may then be extracted from the gourd to be used in various applications.



Figura 18 - *Luffa cylindrica*: a) Plant; b) Early harvested gourd; c) Ripen gourd; d) Luffa sponge.

Luffa cylindrica can be used in an array of different applications. While the young loofah fruit is edible, the fibrous matured gourd is widely used as a cleaning sponge. Other than that, many studies have been unveiling new possible uses of luffa fibers. OBOH et al. (2009) highlight technological applications in various science fields, such as agriculture, biotechnology, medicine, and engineering (OBOH; ALUYOR, 2009). PARTAP et al (2012) compile the pharmacological actions of substances found in *Luffa cylindrica* (PARTAP et al., 2012). Luffa fibers have been studied as a reinforcement material for polymeric matrix composites (BOYNARD; D'ALMEIDA, 2000; SIQUEIRA et al., 2013). Adsorption systems based on the sponge gourd have been proposed for the removal of dyes, phenols, cationic surfactants, and heavy metal ions (ABDELWAHAB; AMIN, 2013; BASTOS et al., 2017; HENINI et al., 2012; LINDINO et al., 2014; SHAHIDI; JALILNEJAD; JALILNEJAD, 2015; YE; HU; WANG, 2013).

Luffa sponges are materials with hierarchical architectures at different length scales. At each hierarchical level, there is a corresponding density. At the macroscopic scale, considering the entire luffa gourd volume, literature specifies densities ranging from 25 to 65 kg.m⁻³ (SHEN et al., 2012). At the sponge fibers scale densities range from 350 to 650 kg/m³ (PAGLICAWAN et al., 2005; SHEN et al., 2012). Finally, at the microscopic cell wall scale, densities in the range of 820 to 920 kg.m⁻³ have been measured (SATYANARAYANA; GUIMARÃES; WYPYCH, 2007; TANOBE et al., 2005). *Luffa cylindrica* is considered low-density biomass, as most natural fibers register values higher than 1000 kg.m⁻³ (PEREIRA et al., 2015). Figure 19 compiles *Luffa cylindrica* images from literature at different levels of magnification. The porosity between the fibers at the macroscopic scale and within the fibers at the microscopic scale explains the different densities reported in the literature.

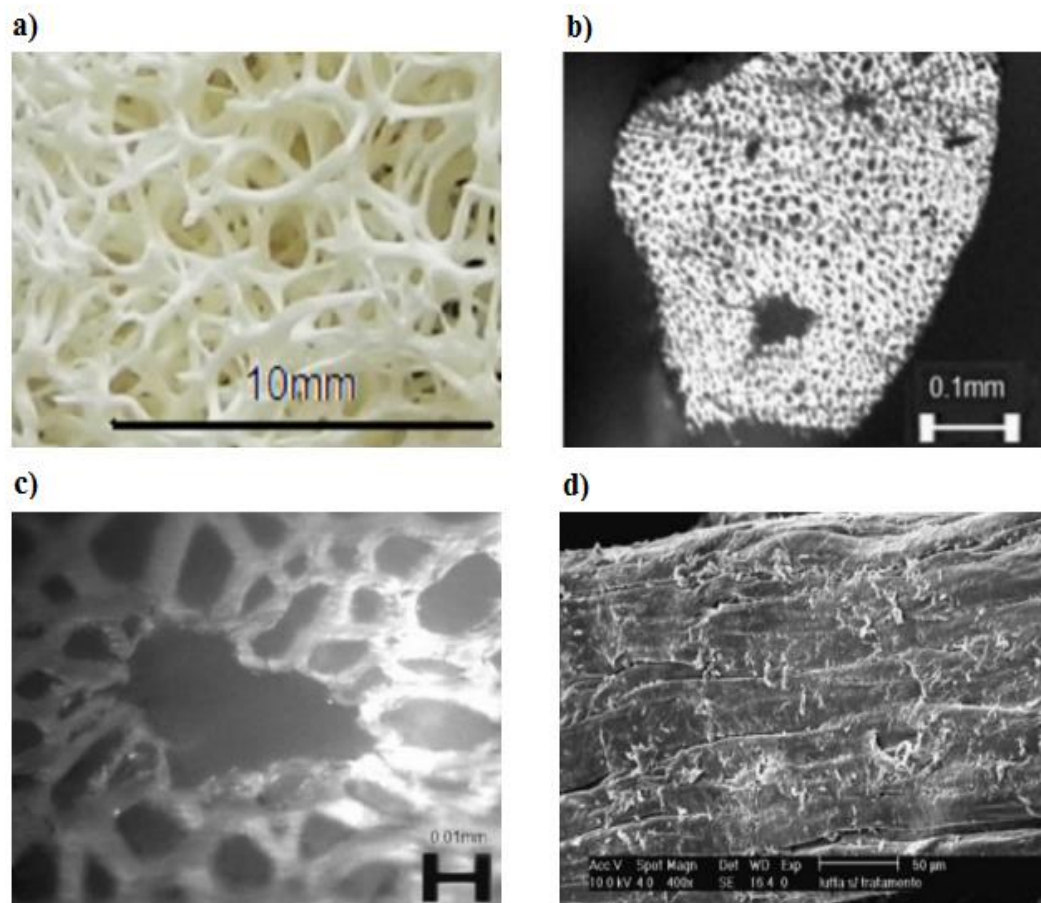


Figure 19 - *Luffa cylindrica* fibers: **a)** at 10 mm macroscopic scale (SHEN et al., 2012); **b)** at 0.1 mm scale (cross-section) (SHEN et al., 2012); **c)** at 0.01 mm scale (cross-section) (SHEN et al., 2012); **d)** Scanning Electron Microscope micrograph (X400) (TANOBE et al., 2005).

2.2.1 Characterization of *Luffa cylindrica* Fibers

In recent years, many studies have focused on the characterization of *Luffa cylindrica* fibers. *Luffa cylindrica* is a lignocellulosic biomass source, thus it is mainly composed of cellulose, hemicellulose, and lignin (TANOBE et al., 2005). The chemical composition of Luffa fibers depends on several factors, such as plant origin, weather conditions, soil nature, and others (SIQUEIRA et al., 2013). Table 2 presents the chemical composition of *Luffa cylindrica* found in the literature. Sponge gourd fibers have a higher cellulose content than most lignocellulosic biomasses (WANG et al., 2017).

Table 2 - Chemical composition (wt %) of *Luffa cylindrica* fibers from literature.

Cellulose	Hemicellulose	Lignin	Others	Reference
63	19.4	11.2	3.6	(TANOBE et al., 2005)
65.5	17.5	15.2	3.8	(SIQUEIRA et al., 2013)
63	14.4	1.6	21	(SEKI et al., 2011)

Ultimate analysis of *Luffa cylindrica* gourd is also available in the literature and can be seen in Table 3 (LAIDANI et al., 2012; SIQUEIRA et al., 2013; ZDARTA; JESIONOWSKI, 2016a). Like most vegetable biomasses, Luffa fibers are a highly oxygenated material with an O/C ratio close to one (SHEN et al., 2010b). Hydrogen and Nitrogen are the other two most expressive elements, although in much lower proportions.

Table 3 - Ultimate analysis (wt %) of *Luffa cylindrica* fibers from literature.

Carbon	Hydrogen	Nitrogen	Oxygen	Reference
41.2	6.2	<0.10	51.3	(SIQUEIRA et al., 2013)
46.5	7.7	3.8	37.6	(LAIDANI et al., 2012)
46.2	19.5	7.3	-	(ZDARTA; JESIONOWSKI, 2016b)

Figure 20 shows a Fourier Transform Infrared (FTIR) spectrum of untreated *Luffa cylindrica* fibers from literature.

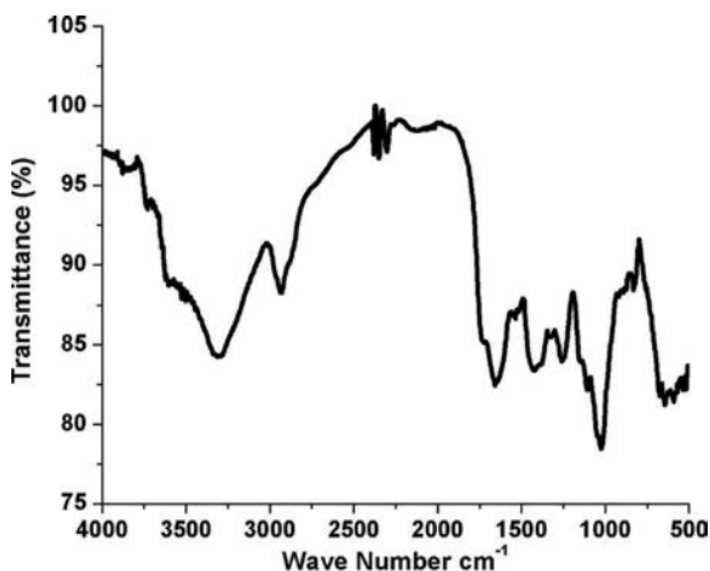


Figure 20 - FTIR of raw *Luffa cylindrica* fibers (NAGARAJAGANESH; MURALIKANNAN, 2016).

Spectrums found in different papers present very similar data, with roughly the same absorption peaks, except for small shifts in the functional groups. Table 4 compiles usual *Luffa cylindrica* FTIR spectrum peaks and their assignments found in the literature.

Table 4 – FTIR Peaks of *Luffa cylindrica* fibers.

Wavenumber (cm ⁻¹)	Assignment	Reference
3300	OH stretching	(NAGARAJAGANESH; MURALIKANNAN, 2016; SEKI et al., 2011; SIQUEIRA et al., 2013; TANOBE et al., 2005)
2929	Saturated C–H stretching	(NAGARAJAGANESH; MURALIKANNAN, 2016; SEKI et al., 2011; SIQUEIRA et al., 2013; TANOBE et al., 2005)
1730	C=O stretching (acetyl or carboxylic acid)	(SEKI et al., 2011; SIQUEIRA et al., 2013; TANOBE et al., 2005)
1649	OH bending (absorbed water)	(NAGARAJAGANESH; MURALIKANNAN, 2016; SEKI et al., 2011; TANOBE et al., 2005)
1579	C=C stretching of aromatic	(NAGARAJAGANESH; MURALIKANNAN, 2016)
1505	C–H aromatic bending	(SEKI et al., 2011; TANOBE et al., 2005)
1454	CH ₂ symmetric bending (lignin)	(TANOBE et al., 2005)
1423	CH ₂ bending (cellulose)	(NAGARAJAGANESH; MURALIKANNAN, 2016;

1381	C-H bending	SEKI et al., 2011; TANOBE et al., 2005) (NAGARAJAGANESH; MURALIKANNAN, 2016; SEKI et al., 2011; TANOBE et al., 2005)
1355	O-H in-plane bending (cellulose)	(TANOBE et al., 2005)
1143	Antisymmetric bridge C-OR-C stretching (cellulose)	(NAGARAJAGANESH; MURALIKANNAN, 2016; SEKI et al., 2011; TANOBE et al., 2005)
1107	Anhydroglucose ring	(NAGARAJAGANESH; MURALIKANNAN, 2016; SEKI et al., 2011)
1022	C-OR stretching (cellulose)	(NAGARAJAGANESH; MURALIKANNAN, 2016; SEKI et al., 2011; TANOBE et al., 2005)
819	Antisymmetric out of phase ring stretching	(NAGARAJAGANESH; MURALIKANNAN, 2016; SEKI et al., 2011; TANOBE et al., 2005)

Figure 21 shows X-ray Diffraction spectra from literature (XRD). Typical *Luffa cylindrica* XRD pattern can be found in many papers with main diffraction signals at $2\theta = 16.8$, 23.3 and 34.9° assigned to (1 0 1), (0 0 2) and (0 4 0) cellulose diffraction planes, respectively (NAGARAJAGANESH; MURALIKANNAN, 2016; PREMALATHA et al., 2019; SIQUEIRA et al., 2013; TANOBE et al., 2005). The crystallinity index of untreated *Luffa cylindrica* fibers found in the literature ranges from 52.4 to 59.1% (NAGARAJAGANESH; MURALIKANNAN, 2016; PREMALATHA et al., 2019; TANOBE et al., 2005).

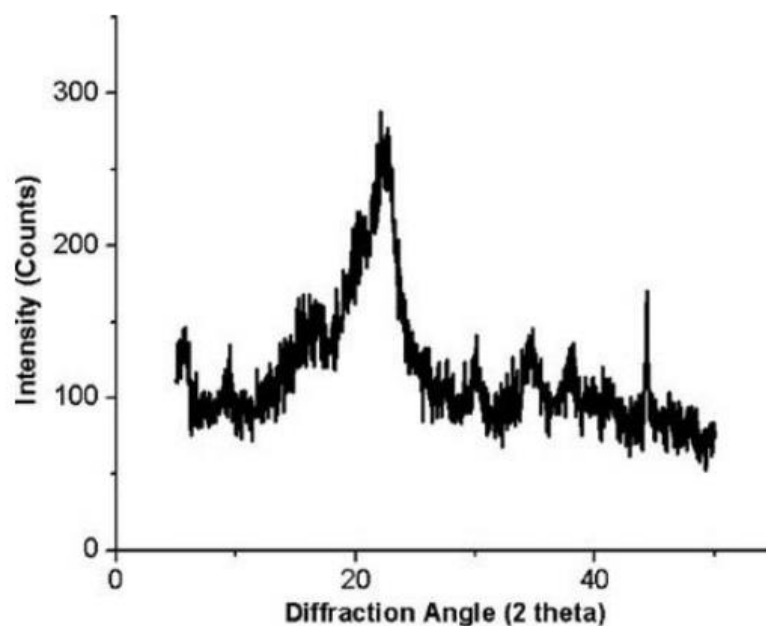


Figure 21 - X-ray diffraction pattern of *Luffa cylindrica* fibers(NAGARAJAGANESH; MURALIKANNAN, 2016).

Tanobe et al. (2005) and Seki et al. (2012) have performed X-ray photoelectron spectroscopy analysis of *Luffa cylindrica* fibers (SEKI et al., 2011; TANOBE et al., 2005). Figure 22 shows the photoelectron spectrum found in Tanobe's work and the deconvolution of the C1s peak, with the respective functional groups associated with each envelope. Apart from the functional groups identified by Tanobe et. al. (2005), a C-C/C-H peak was found in Seki's deconvolution at approximately 285 eV. The surface atomic composition was determined in both papers through the XPS technique: C - 59.6%, O - 36.1%, and N - 4.3% for Seki's work, and C - 64.0%, O -34.9%, and N - 1.2%. Thus, O/C ratios were found to be 0.57 and 0.54, respectively. When this ratio reaches 0.83 the sample is said to be pure cellulose, whereas when it is in the range of 0.31 - 0.40, it is said to be pure lignin (TÓTH et al., 1993). The abundance of carbon, oxygen, and nitrogen can be explained due to proteins and alkaloids characteristic of vegetable materials (TANOBE et al., 2005).

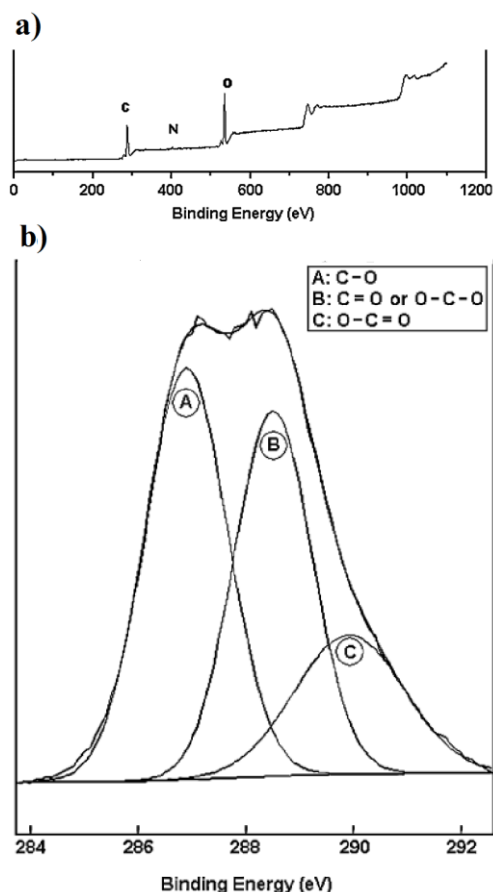


Figure 22 - XPS spectrum of *Luffa cylindrica* fibers (TANOBE et al., 2005): a) Over a binding energy range of 0–1200 eV; b) Deconvolution of C1s peak.

Thermogravimetric analysis of *Luffa cylindrica* fibers have been published by several authors (BOYNARD; D’ALMEIDA, 2000; NAGARAJAGANESH; MURALIKANNAN, 2016; PREMALATHA et al., 2019; SEKI et al., 2011; TANOBE et al., 2005; ZHANG et al., 2017). Although their experimental parameters may vary, the results obtained by them are remarkably similar. Nitrogen and argon atmospheres, 10 to 20 °C.min⁻¹ heating rate and 500 to 800 °C final temperatures are found in these articles. *Luffa cylindrica* TGA/DTG curves from the literature are displayed in Figure 23. Usually, the first event portrayed in these analyses is the water loss at temperatures below 110 °C (100% to 95% in weight) (NAGARAJAGANESH; MURALIKANNAN, 2016). Then, due to the pyrolysis of hemicelluloses, the fibers undergo thermal decomposition mass loss, 95 to 85% in weight, at temperatures from 220 to 300 °C (PREMALATHA et al., 2019). The greatest event in Figure 23 is an expressive mass loss (85 to

40 wt %) at temperatures between 300 and 370 °C, due to the pyrolysis of cellulose, the main component of *Luffa cylindrica* fibers (TANOBE et al., 2005). The slow and steady decrease in weight observed from 370 to 700 °C is commonly associated with the pyrolysis of lignin, an especially thermally stable component of lignocellulosic biomass (SEKI et al., 2011).

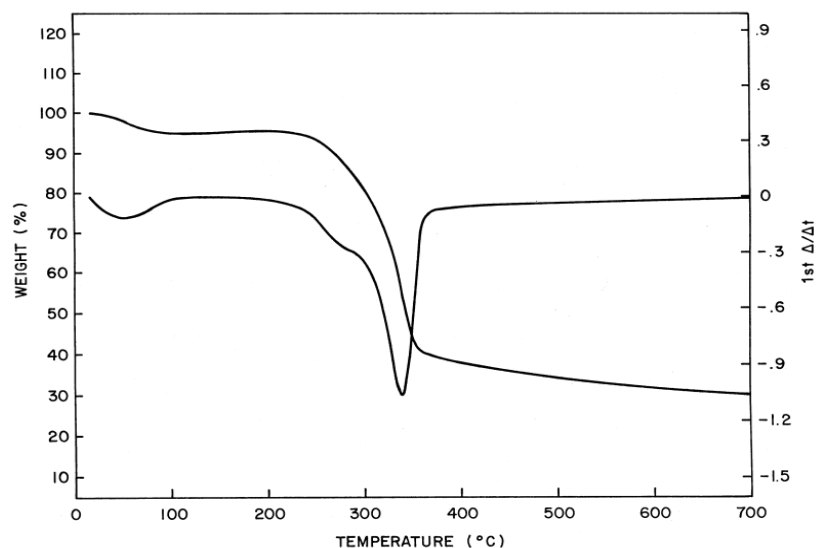


Figure 23 - TGA/DTG curves of *Luffa cylindrica* fibers (BOYNARD; D'ALMEIDA, 2000).

Zhang et al. (2017) performed Differential Scanning Calorimetry of *Luffa cylindrica* (Figure 24) (ZHANG et al., 2017). The analyzed sample mass was approximately 10 mg. The flow rate of the nitrogen was 60.0 mL.min⁻¹, and the heating rate was 10 C.min⁻¹. Only one endothermic peak with a heat flow of about -9 mW appears at 373 °C in the DSC curve, suggesting the cracking of organic matter and carbonization processes. This peak is related to the cellulose endothermic depolymerization, which can also be found in Figure 3.

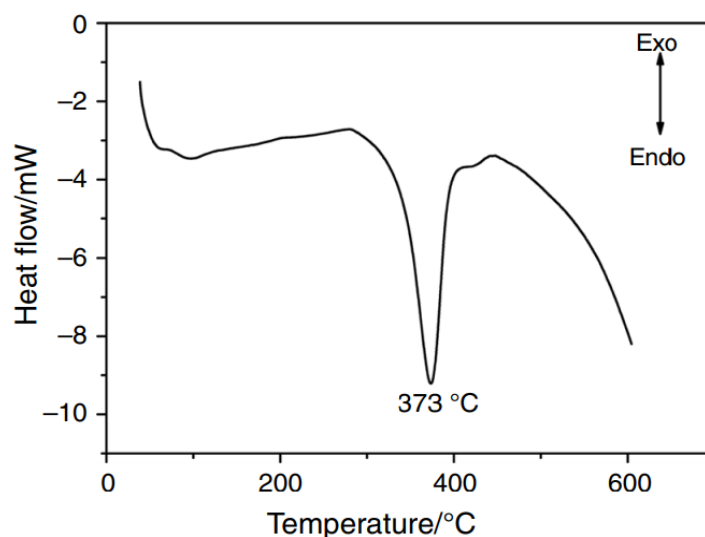


Figure 24 - DSC curve of *Luffa cylindrica* fibers (ZHANG et al., 2017).

2.2.2 *Luffa Cylindrica* Biochar: Pyrolysis and Adsorption

Zhang et al. (2017) performed thermal destruction of luffa sponge under air and nitrogen atmospheres (ZHANG et al., 2017). However, as pyrolysis is a process that occurs in the absence of oxygen, only nitrogen atmosphere results were taken into consideration for this work. 25 g of cleaned luffa sponge was placed in a furnace and heated at 400, 500, 600, and 700 °C. The flow rate of the nitrogen was 20 mL.min⁻¹. The isothermal time was 2 h, and the heating rate was 10 C.min⁻¹. Table 5 shows the calculated BET surface area, pore-volume, mesopore volume, and average pore size of the samples. As expected, BET surface area and total pore volume substantially increase with temperature. It is important to note that, for every final temperature, a high percentage of the volumetric porosity is due to mesopores. Mesopores are 2-50 nm wide pores, which are essential to adsorption materials properties because some organic molecules, like many dyes, are too big to fit in micropores (CHEN et al., 2012).

Table 5 – BET analyses of *Luffa cylindrica* biochars pyrolyzed at different temperatures (ZHANG et al., 2017).

Final temperature (°C)	BET surface area (m ² .g ⁻¹)	Total pore volume (cm ³ .g ⁻¹)	Mesopore volume (cm ³ .g ⁻¹)	Mesopore percentage (%)	Average pore size (nm)
400	11.0	0.025	0.022	88.00	9.08
500	58.7	0.056	0.038	67.86	3.84
600	50.3	0.083	0.072	86.75	6.58
700	168.8	0.199	0.161	80.90	4.70

Research on the adsorption of several heavy metals using *Luffa cylindrica* biochar as adsorbent material has been made (LIATSOU et al., 2017a, 2017b; LIATSOU; CHRISTODOULOU; PASHALIDIS, 2018; LIATSOU; CONSTANTINOU; PASHALIDIS, 2017). For Liatsou`s adsorption experiments, *Luffa cylindrica* sponges were thermally treated for 1 hour at 700 °C under a nitrogen atmosphere to obtain biochar. Biochar activation was carried out by chemical oxidation in HNO₃ for 3 hours at 80 °C under reflux and continuous stirring. The product was washed until pH neutrality. The neutralized material was then dried in an oven at 130 °C for 24 h in the air. FTIR analysis of the resulting biochar after oxidation in different HNO₃ concentrations was performed (Figure 25) (LIATSOU et al., 2017b). The characteristic *Luffa cylindrica* absorption peaks found in figure 20 are not observed in figure 25. New signals at 1420 and 1100 cm⁻¹ are present. These peaks are characteristic of carbonized cellulosic materials and correspond to conjugated carbon-carbon stretching vibration (GEDAM; DONGRE, 2016). Activation of the carbonized material results in dramatic changes in the IR spectrum. Absorption bands found at 1713 and 1242 cm⁻¹ are attributed to carbonyl stretching vibrations and carboxylic acid bending vibrations, respectively (LIATSOU et al., 2017b).

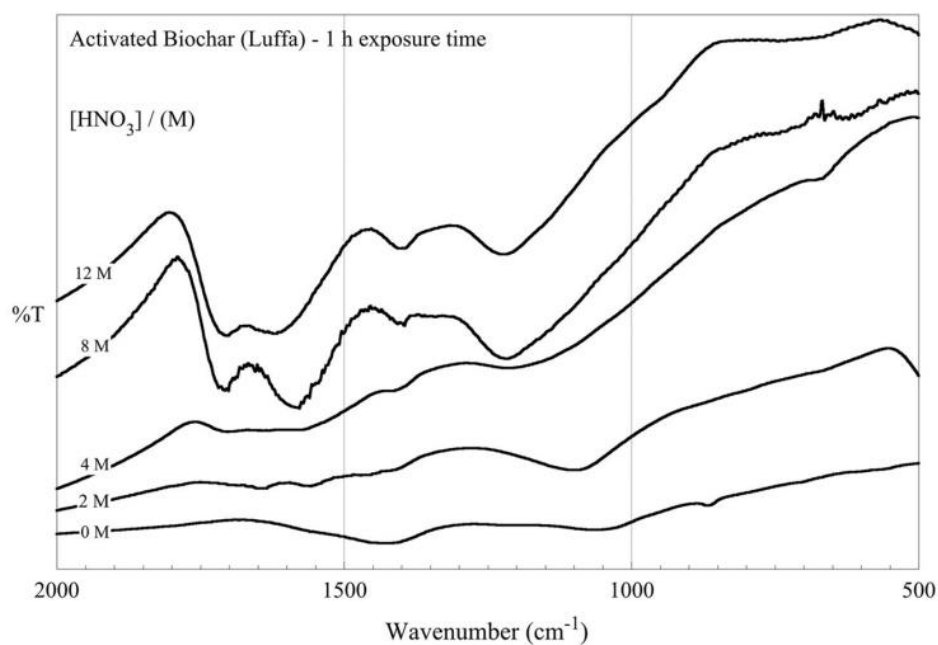


Figure 25. FTIR spectra of *Luffa cylindrica* activated biochar prepared by treatment with nitric acid in various concentrations (LIATSOU et al., 2017b).

The adsorption experiments carried out by Liatsou et al. (2017) were performed with biochar activated using 8 M HNO₃. Test solutions (15 ml) containing the metal ions in known concentrations were mixed with activated biochar (0.01 g) and the mixture was stirred in a thermostatic orbital shaker (at 100 rpm) for 24 h to assure that equilibrium had been reached. Table 6 shows the results for maximum adsorption capacity based on the Langmuir adsorption isotherm of samarium, uranium, copper, and thorium ions in water solutions. All of the solutions were prepared at pH 3, a non-optimal pH for the adsorption process due to the de-protonation of the carboxylic surface groups, which bind the cations by forming inner-sphere surface complexes (LIATSOU et al., 2017a). In the cases studied by Liatsou et al. (2017), it was not possible to determine the maximum adsorption capacities at higher values of pH, once there was no observable surface saturation in the adsorption isotherms. Cationic solubility was exceeded before the maximum adsorption capacity.

Table 6. The maximum adsorption capacity of some heavy metal ions by *Luffa cylindrica* oxidized biochar.

Adsorbate	Chemical activator	pH	Maximum adsorption capacity (mmol.g ⁻¹)	Maximum adsorption capacity (mg.g ⁻¹)	Reference
Samarium(III)	HNO ₃	3	2.4	360	(LIATSOU et al., 2017a)
Uranium(VI)	HNO ₃	3	0.39	92	(LIATSOU et al., 2017b)
Copper(II)	HNO ₃	3	3.9	248	(LIATSOU; CONSTANTINOU; PASHALIDIS, 2017)
Thorium(IV)	HNO ₃	3	0.30	70	(LIATSOU; CHRISTODOULOU; PASHALIDIS, 2018)
Lead(II)	Chitosan	5	0.54	112	(GEDAM; DONGRE, 2016)

Gedan and Dongre (2016) have used activated carbon from *Luffa cylindrica* doped chitosan for mitigation of lead (II) from aqueous solution (GEDAM; DONGRE, 2016). Clean and dry *Luffa* fibers were pyrolyzed in a modified muffle furnace in a nitrogen atmosphere. The temperature was increased at a rate of 10 °C.min⁻¹ and kept at 700-800 °C for 1 hour. Chitosan dissolved in a 3% acetic acid solution was blended with the obtained biochar on a magnetic stirrer at 800 rpm at room temperature for 6 hours in a 1:1 ratio. The mixture was then dropped in 50% aqueous ammonia, washed in distilled water, and dried. Batch adsorption experiments were carried out to study the effect of operating parameters such as pH, initial metal ion concentration,

and contact time on the adsorption rate. All adsorption experiments were carried out at room temperature in Erlenmeyer flasks containing 100 ml of test solution agitated on a rotary shaker at 200 rpm. Adsorption rate grows rapidly from pH 2 to pH 5 and slowly decreases until pH 8. This recurrent behavior is due to the protonation of adsorption sites at lower pH values and the precipitation of the metallic cation in alkaline solutions. The uptake of lead (II) ions increases with time with a maximum of 98 % (for 35 mg.L⁻¹) to 86 % (for 115 mg.L⁻¹) lead (II) removal efficiency and thereafter, the rate of adsorption becomes slower near the equilibrium. The adsorption experimental data were fitted to the Langmuir adsorption isotherm model with a maximum monolayer adsorption capacity of 112 mg.g⁻¹.

Anastopoulos and Pashalidis (2019) have applied oxidized carbon derived from *Luffa cylindrica* for Caffeine removal from aqueous solutions (ANASTOPOULOS; PASHALIDIS, 2019). The preparation of the biochar followed the method described by Liatsou (2017a) (LIATSOU et al., 2017a). Adsorption studies were conducted by equilibrating 0.05 g of biochar with 30 mL of Caffeine solutions of the desired concentration in 50 mL plastic tubes. The content of the tubes was agitated on an orbital shaker at 125 rpm at constant temperatures. Adsorption parameters such as contact time, temperature, and pH were studied. The adsorption was found to be very fast in the first 10 min and with progressing contact time, the adsorption rate decreases gradually until equilibrium is achieved after 80 min. The adsorption capacity was found to increase with a decrease in temperature, which indicates the adsorption process to be exothermic. The adsorption was found to increase slightly from pH 1 to pH 4 and then decrease continuously up to pH 8. The maximum adsorption capacity, obtained from the Langmuir isotherm model, was estimated to be 59.9 mg.g⁻¹ at pH 4 and 298 K.

Feng et al. (2018) performed the removal of Norfloxacin, an antibiotic medication, from an aqueous solution using biochar derived from a luffa sponge (FENG et al., 2018). 3 to 4 mm pieces of clean, dry Luffa fibers were infused in 85 wt % phosphoric acid at room temperature for 12 h at a solid-liquid ratio of 1:4 (g:mL). After activation, the samples were pyrolyzed for 2 h in a box-type resistance furnace at 450 °C. The biochar was then washed until pH was close to neutral. BET analysis of the obtained biochar was performed, resulting in an 822.35 m².g⁻¹

specific surface area and a 5.35 nm average pore size. While the pore size result of Feng`s work is similar to the one found in the research of Zhang et al. (2017), the specific surface area is substantially higher. This result could be explained mainly by the acid activation process specified in Feng`s work (FENG et al., 2018). Batch adsorption experiments were carried out at a constant stirring velocity of 180 rpm in a temperature-controlled oscillator. Parameters, such as contact time, temperature, pH, and biochar content were evaluated for an initial concentration of 100 mg.L⁻¹ of Norfloxacin. Experimental data was successfully described by the Langmuir model. *Luffa cylindrica* biochar adsorbed 99.86% of the Norfloxacin with maximum absorption of approximately 250 mg.g⁻¹.

Therefore, given the theoretical framework addressed in this work, the study of the pyrolysis of *Luffa cylindrica* fibers in an electrical furnace and a solar ensemble was proposed. To reach this goal, two solar pyrolyzers were designed and built. *Luffa cylindrica* fibers and the produced biochars were characterized. An extensive discussion regarding the influence of reactional parameters on biochar properties is presented in this document. Finally, preliminary adsorption experiments were carried out to evaluate the influence of pyrolysis parameters on adsorption performance.

3 METHODOLOGY

3.1 DESIGN AND CONSTRUCTION OF TWO SOLAR PYROLYZERS

Two solar pyrolyzer designs are proposed in this work: one with a parabolic trough collector, and the other with a parabolic dish collector. The parabolic trough design has been chosen due to its characteristic focal line. Even though the solar pyrolysis methods proposed in section 3.3 are batch processes, the parabolic trough design will enable future continuous solar pyrolysis reactions studies. The parabolic dish design, on the other hand, although only suitable to batch processes, usually has a higher irradiance concentration ratio, which enables the use of a smaller, more practical collector. Furthermore, it is important to highlight that the parabolic dish solar pyrolyzer proposed in this work was constructed mainly with recycled materials. The low

assembly cost of both pyrolyzers is also highlighted since the parabolic trough reactor had a cost of less than R\$10.000,00 and the recycled parabolic dish reactor had a cost of R\$200,00.

The proposed parabolic trough solar collector design (Appendix A) consists of a curved carbon steel sheet (Appendix B) fully covered by thin aluminum-coated mirror stripes (Appendix C). Aluminum has been chosen as the reflective material, once it possesses a reflectance index higher than 90% for the solar spectrum and good corrosion resistance (FEARON et al., 2007; FOLEY, 1986). A cylindrical 316L stainless steel reactor (Appendix D) is placed at the focal line of the parabola. A total of 90% of the reactor surface is thermally insulated by 50 millimeters, 128 kg/m³ ceramic fiber insulator. The other 10% of the surface was painted with a high temperature resistant commercial black paint to maximize absorption of concentrated solar radiation. Finally, a metallic structure is responsible for supporting all pieces in the right positions. This structure is equipped with four wheels to enable easy transportation and set-up. It also possesses a reactor height regulator to ensure the reactor is positioned at the focal line of the collector. The structure is equipped with rolling arms to support the steel sheet. The rolling feature of the support is essential to the project, once it enables some angular movement of the collector to compensate for the movement of the sun throughout the day, ensuring higher radiation collection. Specific project parameters, such as but not limited to reactor length and diameter, are found in the referenced Appendixes. Measures are always referred to in millimeters for length and in degrees for angles.

The proposed parabolic dish solar collector consists of a reused satellite antenna covered with a commercial reflective film. The antenna has a parabolic shape with a 65 cm vertical diameter and a 60 cm horizontal diameter. The chosen reflective film is an aluminized biaxially-oriented polyethylene terephthalate (boPET), a polymer used for its high tensile strength, chemical and dimensional stability, transparency, gas, and aroma barrier properties, and electrical insulation. When coated with aluminum by vacuum metallization, a physical vapor deposition process, boPET becomes highly reflective, with a reflectance index of 89.5% (GOOD et al., 2016). Aluminized boPET, therefore, was chosen as the reflective material for the parabolic dish solar collector due to its high reflectance and its ease of application, since it is a malleable film. It

can be conformed to the three-dimensional parabolic shape of the collector without great difficulty. A reactor made of a reused cylindrical can of paint was placed at one of the focal points of the parabolic dish with one of its plane surfaces facing the parabola. The can of paint has 10 cm of height and a 7,5 cm diameter. All reactor surfaces but the one facing the reflective parabola were insulated with 25 millimeters, 128 kg.m⁻³ ceramic fiber insulator. There was no need to project a support for this system since the antenna already had all the needed structures.

3.2 BIOMASS CHARACTERIZATION

Clean dry *Luffa Cylindrica* gourds, purchased in a typical popular market in Belo Horizonte, Brazil (Mercado Central de Belo Horizonte) were characterized. The chosen characterization methods were: Ultimate Analysis; Thermogravimetric Analysis (TGA); Fourier Transform Infrared Analysis (FTIR); Heat of Combustion Analysis (HHV); and X-Ray Fluorescence Analysis (XRF).

3.2.1 Ultimate Analysis

A *Luffa cylindrica* gourd sample was sent to CTNano UFMG (Centro de Tecnologia em Nanomateriais e Grafeno - UFMG) for the determination of atomic composition via ultimate analysis, also known as elemental analysis. The experiment was conducted in duplicates in an Eurovector 3100 instrument.

3.2.2 X-Ray Fluorescence Spectrometry

A *Luffa cylindrica* gourd sample was sent to the Fuel Testing Laboratory of the Federal University of Minas Gerais (LEC-UFMG) for qualitative X-Ray Fluorescence Spectrometry. Sulfur determination was also performed via X-Ray Fluorescence, following the ASTM D4294-16e1 (Standard Test Method for Sulfur in Petroleum and Petroleum Products by Energy Dispersive X-Ray Fluorescence Spectrometry). These analyses were performed in an IKA C200 equipment.

3.2.3 Thermogravimetric Analysis

Thermogravimetric and Derivative Thermogravimetric Analysis of *Luffa cylindrica* fibers were performed in a TA Instruments Q50 equipment. Curves were obtained in the temperature range from 35 to 900 °C with a 10 °C.min⁻¹ heating rate under 60 mL.min⁻¹ N₂ flux atmosphere.

3.2.4 Fourier Transform Infrared Spectroscopy

For the characterization of the main functional groups present in *Luffa Cylindrica* fibers, an absorption spectrum in the infrared (IR) was obtained in the range of 550 to 4000 cm⁻¹ by ATR (Attenuated Total Reflectance). An ARIS-ZONE ABB Bomem-MB Series equipment with a diamond cell was utilized to acquire 32 reading, 4 cm⁻¹ resolution scans.

3.2.5 Heat of Combustion Analysis

A *Luffa cylindrica* gourd sample was sent to the Fuel Testing Laboratory of the Federal University of Minas Gerais (LEC-UFGM) for heat of combustion determination. The essay was performed following the ASTM D5865M-19 (Standard Test Method for Gross Calorific Value of Coal and Coke) on a Shimadzu EDX 800 equipment.

3.2.6 Scanning Electron Microscopy

A *Luffa cylindrica* gourd sample was analyzed via Scanning Electron Microscopy (SEM) at the UFGM Microscopy Center (Centro de Microscopia da UFGM). The sample was prepared on conductive carbon adhesive tape. Due to the non-conductive character of the natural fibers, it was necessary to apply a carbon sputter coating onto the sample to avoid the surface charging effect caused by the electron beam. Images were obtained by secondary electrons detection in a FEI Quanta FEG 3D equipment with a 15 keV electron beam. Energy-Dispersive X-Ray Spectroscopy (EDS) was performed with a XFlash 5010 detector.

3.3 ELECTRIC FURNACE BIOMASS PYROLYSIS

The electric furnace biomass pyrolysis was performed in a 0.45 m long stainless-steel tubular reactor, which was placed inside of a Fortelab FT 1200 H/V furnace (Figure 26).



Figure 26 - Fortelab FT 1200 H/V furnace (“FORTELAB - Industria de Fornos Elétricos LTDA - Forno FT - 1200H/V”, [s.d.]).

The arrangement is equipped with a thermocouple inside the tubular reactor for temperature control, as shown in Figure 27. In each pyrolysis experiment, approximately 6 g of clean sponge gourd was added to the reactor. The biomass was not milled, since in its gourd form it already presents a very high surface/volume ratio. The reactor was then heated under a 1 L.min⁻¹ nitrogen gas flow. Once the final pyrolysis temperature was reached, the furnace was promptly turned off and the tubular reactor was removed from it, so it could naturally be cooled down to ambient temperature. The obtained biochar masses were weighted and reserved for future analysis. Volatile products were not collected, given that this work focuses solely on the solid products and their adsorption performance.

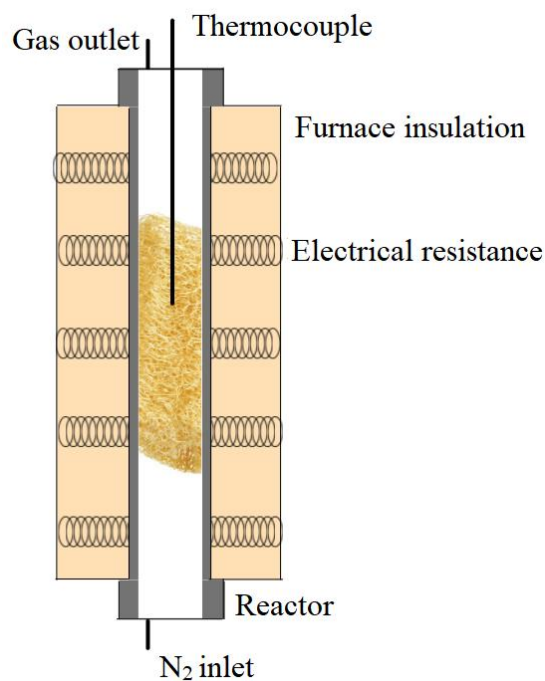


Figure 27 – Schematic of the electrical furnace pyrolysis arrangement (cross-section).

Pyrolysis experiments were performed to study the effect of pyrolysis temperature and heating rate on the resulting biochar. The final temperatures of 300, 400, and 500 °C were selected for this study. At 300 °C, only the hemicelluloses were expected to degrade. At 400 °C cellulose pyrolysis was anticipated as well. Only at 500 °C, it was prospected some of the lignin content being partially degraded. Pyrolysis with heating rates of 2, 10, and 20 °C.min⁻¹ were performed for all final temperatures, totalizing 9 experiments. Slow hating rates were chosen because solid biochar is the product of interest in this study. To make this work more comprehensive, biochar samples will be called as shown in Table 7 according to their pyrolysis temperature and heating rate.

Table 7 - Electric furnace biochar nomenclature.

Heating rate (°C.min ⁻¹) \ Temperature (°C)	300	400	500
2	B300-2	B400-2	B500-2
10	B300-10	B400-10	B500-10
20	B300-20	B400-20	B500-20

3.4 BIOMASS SOLAR PYROLYSIS

Delays in the methodology were caused by sanitary restrictions imposed due to the Corona Virus pandemic. The parabolic trough solar reactor could not be assembled in time to perform a pyrolysis run. The parabolic dish solar reactor, however, given its simpler construction, was assembled in time. A pyrolysis run was performed on 26/07/2021. The solar collector was aligned to the Sun ray's incidence to maximize energy input. A clean sponge gourd (approximately 6 g) was placed inside the reactor. A 1 L/min nitrogen flux was used to guarantee a non-oxidative atmosphere. A thermocouple was placed inside the system to evaluate the temperature. The experiment was conducted for one hour of solar irradiance (12:30 - 13:30 h). The resulting biochar was collected and weighted and reserved for posterior analysis.

3.5 BIOCHARS CHARACTERIZATION

The biochars obtained from electric furnace pyrolysis and solar pyrolysis were subjected to the same characterization methods used to characterize *Luffa cylindrica* fibers described in section 3.2, except for X-Ray Fluorescence Spectrometry and ultimate analysis. The XRF analysis was not performed since the content of inorganic substances in the solid phase is not significantly altered by pyrolysis. Ultimate analysis could not be performed on the biochars due to a limitation on the number of available analyses.

The Scanning Electron Microscopy technique was employed on only 3 biochars, due to a limitation on instrument availability. The chosen biochars for SEM were the one with the highest iodine number, the one with the most complete pyrolysis (B500-2), and the one produced in the solar pyrolyzer. Energy-Dispersive X-Ray Spectroscopy analysis was not performed on the biochars on the same grounds that justify the absence of biochar XRF analysis.

3.6 IODINE ADSORPTION EXPERIMENTS

Iodine adsorptions experiments adapted from the experimental procedure of ASTM D4607-14 (Standard Test Method for Determination of Iodine Number of Activated Carbon)

were performed on all samples. A CABOT Norit GAC 1240 activated carbon was tested as well to establish a standard for this methodology. Biochars were ground to 100% smaller than 154 μm (100#). Milled biochar samples were dried on a stove for 3 h at 120 $^{\circ}\text{C}$ and cooled down to ambient temperature on a desiccator. Approximately 0.5 g of each biochar was weighed and transferred to an Erlenmeyer, where they were acidified with 10 ml 5 wt % hydrochloric acid solution. The mixtures were allowed to boil for 30 s on a hot plate to remove any sulfur that could interfere with test results. 100 ml of a standardized 0.05 N iodine solution were added to each flask with subsequent agitation for 30 s. The mixtures were filtered by gravity, while the filtrates were collected into a flask. The first 20 ml of each filtrate were discarded. 20 ml of each filtrate were then titrated in triplicates with a 0.05 N sodium thiosulfate standardized solution until a pale-yellow color was obtained. 2 ml of a 1 wt % starch solution were, then, added to the solutions as titration indicator. The titration proceeded until a colorless solution was obtained. The average iodine adsorption capacity in $\text{mg}\cdot\text{g}^{-1}$ of each biochar sample was calculated.

4 RESULTS AND DISCUSSION

4.1 DESIGN AND CONSTRUCTION OF TWO SOLAR PYROLYZERS

Two solar pyrolyzers were proposed and built on this work. One with a parabolic trough solar collector, and the other with a parabolic dish solar collector. The entire design process, from energy transfer calculations to the assembly of the reactors, is documented in this section. Most of the mathematical development was kept on the appendixes of this document to facilitate reader understanding. Proper references of these appendixes are made through the text whenever necessary.

4.1.1 Parabolic trough solar pyrolyzer

The parabolic trough solar pyrolyzer was built having the purchased cylindrical reactor (Appendix D) in consideration. In other words, it was necessary to evaluate the heat losses of the reactor at the pyrolysis temperature before designing an adequate solar collector. The solar

collector should be capable of providing the same amount of energy as the reactor loses to maintain maximum temperature.

4.1.1.1 Reactor heat transfer calculations

The most important project parameter to be defined in a slow pyrolysis reactor is the final maximum equilibrium temperature. The reactor temperature is considered to be uniform. As the highest proposed temperature studied in the laboratory scale furnace reactor is 500 °C, the final equilibrium temperature of the solar pyrolyzer was defined to be 900 K, so there was some safety margin for eventual changes in the methodology. The final equilibrium temperature may be understood as the one at which the heat inlet due to the radiation absorption equals the heat loss due to heat convection to the surroundings. As the reactor is covered by a thick layer of insulation material, the radiation heat loss is considered to be neglectable. The 10% of the reactor surface that remains uncovered, on the other hand, radiates considerable amounts of energy. Although, as it radiates from the focal point of the parabolic trough, most of this energy is reflected towards the reactor itself, making this effect less pronounced. The pyrolysis reaction heat is also neglected in this work, given the small amounts of biomass that could potentially fit in the reactor, when compared to the order of magnitude of the heat inlets and outlets. Furthermore, biomass pyrolysis reactions, as can be seen in Figure 3, exhibit a thermic behavior ranging from endothermic to largely exothermic that strongly depends on the biomass type.

To define the convective heat flow of the partially insulated reactor system, convective coefficients of exposed and insulated cylinder reactors were obtained through Zukauskas's correlation, Equation 1, for circular cylinders with cross flow (INCROPERA; BERGMAN; LAVINE, 2008).

$$Nu_d = \frac{h*d}{k} = C * Re_d^m * Pr^n * \left(\frac{Pr}{Pr_s}\right)^{0.25} \quad (1)$$

All of the properties above are calculated at ambient temperature (considered to be 300 K), except for Pr_s , which is calculated at the surface temperature (900 K for the exposed cylinder

and calculated in Appendix E for the insulated cylinder). Nu_d and Re_d are the Nusselt and Reynolds numbers for the diameter of the reactor, respectively. The convective coefficient is represented by h , while d is the diameter of the reactor and k is the thermal conductivity of air. Pr and Pr_s are, respectively, the Prandtl numbers calculated at ambient and surface temperatures. C , m , and n are constants whose values depend on the Reynolds and Prandtl numbers.

The convective coefficient for the reactor insulated lids is calculated through the correlation below (Equation 2), which considers the lids to be flat plates in a laminar flow with constant thermal flow (INCROPERA; BERGMAN; LAVINE, 2008).

$$Nu_L = \frac{h*L}{k} = 0.453 * Re_L^{1/2} * Pr^{1/3} \quad (2)$$

All of the properties above are calculated at ambient temperature (considered to be 300 K). Nu_L and Re_L are the Nusselt and Reynolds numbers for the length of the flat plate, respectively. The convective coefficient is represented by h , while L is the length of the flat plate, which is considered to be equal to the edge of and square whose area is equivalent to the reactor lid's area ($L = \frac{d}{2} * \sqrt{\pi}$). The thermal conductivity of air is represented by k , while Pr is the Prandtl number calculated at ambient temperature.

The calculations for the convective coefficients are available in Appendix E. As the surface temperature of the insulated cylinder is unknown, an iterative algorithm was implemented to obtain its convective coefficient and surface temperature. Thermophysical properties of air at atmospheric pressure were obtained from Incropera et al. (2008) (INCROPERA; BERGMAN; LAVINE, 2008). The velocity of the airflow considered in the calculations was the global average wind velocity over land, 3.28 m.s^{-1} (ARCHER; JACOBSON, 2005). The conductivity of the insulator was informed by the manufacturer ($0.12 \text{ W.m}^{-1}.\text{K}^{-1}$). Table 8 presents the calculated convective coefficients and outer surface temperatures for the insulated and exposed cylinders designs and the reactor lids.

Table 8 - Calculated convective coefficients and surface temperatures for exposed and insulated cylinders designs and insulated lids of the cylinders.

Design	Surface temperature (K)	Convective coefficient ($W \cdot m^{-2} \cdot K^{-1}$)
Exposed cylinder	900	26.3
Insulated cylinder	347	18.8
Reactor lid	377	16.2

The critical radius is calculated to ensure that the thick insulation layer is capable of mitigating heat loss due to its low conductivity, rather than enhancing it by heat convection to the surroundings, given the increase in surface area. The critical radius of an insulated system is the one at which the heat transfer to the surroundings finds its maximum value (SAHIN; KALYON, 2004) and for a cylinder is calculated by dividing the insulated system convective coefficient by the insulating material conductivity. For the minimization of heat loss, it is desired the insulated system radius to be greater than the critical radius. Considering the calculated convective coefficient and the thermal conductivity of the insulator, the critical radius for the solar pyrolyzer is 6 mm. As the diameter of the insulated tube is 173 mm, the insulation can be safely considered efficient for the mitigation of heat loss.

Once the convective coefficients and surface temperatures are known, it is possible to calculate the total heat transfer from Equation 3. Because the cylindrical reactor is designed to have 90% of its area covered by the ceramic fiber insulator, while the other 10% are exposed, it is considered that the total heat loss of the partially insulated cylinder is equal to the sum of 90% of the heat loss of a fully insulated cylinder and 10% of the heat loss of a fully exposed cylinder. The convective loss at the insulated lids is also considered for the calculation of the total heat loss. Calculations for heat losses are available in Appendix F.

$$Q_{total} = 0.9 * Q_{insulated} + 0.1 * Q_{exposed} + 2 * Q_{lid} \quad (3)$$

Table 9 compiles the calculated heat losses through the exposed cylinder, insulated cylinder, insulated lids, and the total heat loss of the fully assembled reactor, calculated using Equation 3.

Table 9 - Calculated heat losses of insulated and exposed cylinders, insulated lid, and the fully assembled reactor.

Arrangement	Heat loss (W)
Exposed cylinder	1809
Insulated cylinder	240
Insulated lid	9.8
Fully assembled reactor	416

4.1.1.2 Parabolic trough collector design

Once the total heat loss is known, it is possible to project the solar collector to fully satisfy the energetic demands. According to the Brazilian Atlas of Solar Energy, the average daily solar irradiance in Brazil is 5153 W.h.m^{-2} (E. PEREIRRA ET AL., 2006). Considering the standard 12 hours of daily solar light, the average solar irradiance through the day in Brazil is 429 W.m^{-2} . However, as it can be seen in Figure 13, solar radiation strongly varies by the hour of the day. It is considered that the maximum solar irradiance at Earth surface is around 1000 W.m^{-2} , while in a study performed in Brazilian territory, values as high as 1822 W.m^{-2} were measured (DO NASCIMENTO et al., 2019; E. PEREIRRA ET AL., 2006). In this work, the solar irradiance is considered to be 600 W.m^{-2} for design and calculation purposes. This irradiance value allows the reactor to be useful, not only at peak values of solar radiation, but also at suboptimal circumstances. Given the reflectivity of aluminum (taken as 90% in the solar spectrum), available radiation for reactor heating is 540 W.m^{-2} (FEARON et al., 2007).

The ground area that must be covered by the collector can be given by Equation 4, which relates the power requirement (416 W) and available radiation for reactor heating

$$\text{Area} = (\text{Reactor heat loss}) / (\text{solar irradiance}) \quad (4)$$

The calculated ground area that must be covered by the collector is 0.770 m^2 . Once the mirror stripes have been designed to be 0.48 m long, the collector projection must be at least 1.60 m wide. To compensate for the shadow of the insulated reactor, a 1.78 m wide projection has been taken for the solar collector. A 1.20 m curvature radius has been defined as a project parameter, resulting in a 95.6° angle and 2.00 m arc. The reactor must then be placed at the

collector focal line, which is half the radius curvature, in other words, at 0.60 m. The parabolic trough solar pyrolyzer was assembled and can be seen in Figure 28.



Figure 28 - Assembled parabolic trough solar pyrolyzer.

Solar pyrolysis experiments could not be conducted on the parabolic trough reactor. The collector support design has a limitation regarding the angle adjustment range. In July 2021, when solar pyrolysis experiments were to be performed, solar elevation reached values up to 50 ° at the highest point of the day (CASIO COMPUTER, 2021). Such low elevations could not be reached by a simple support design, where the collector is held down only by its weight. A stiffer collector and a more complex support structure are required. The adjustment range limitation caused the solar light to be only reflected from a portion of the collector, drastically reducing its effectiveness. Maximum recorded temperatures were only around 250 °C.

4.1.2 Parabolic dish solar pyrolizer

Like the previous calculation, the reactor temperature is considered to be uniform, and the final temperature is the one at which solar heat input equals convection heat loss. Unlike the previous solar collector design, the structure of the parabolic dish cannot be altered since it has been reused from a satellite antenna. Therefore, the calculations now go the other way around, reactor final temperature is calculated with the knowledge of the design. The collection area is known to be 0.3063 m^2 since the two diameters of the parabola are 60 cm and 65 cm. The insulated reactor projects a shadow of 0.0123 m^2 (12.5 cm diameter), which lowers the collection area to 0.2940 m^2 . Considering Equation 4, 600 W.m^{-2} of available irradiation and 89.5% aluminized boPET reflectance, reactor heat input is calculated to be 158 W.

Convective coefficients calculations for the insulated cylinder portion, as well as for the reactor lids are presented in Appendix G. The convective coefficient for the cylinder portion is calculated to be $21.2 \text{ W.m}^{-2}.\text{K}^{-1}$, while for both lids, it is $18.3 \text{ W.m}^2.\text{K}^{-1}$. To calculate the theoretical final temperature of the parabolic dish solar pyrolizer, an energy balance must be established, considering the insulated reactor as the control volume. In the equilibrium, the total solar heat input equals the sum of heat losses through the insulated cylindrical portion of the reactor, the insulated lid, and the exposed lid, as follows in Equation 5.

$$Q_{input} = Q_{Ins.lid} + Q_{Exp.lid} + Q_{Ins.cyl} \quad (5)$$

Calculations for the final reactor temperature are presented in Appendix H. Theoretical final temperature is calculated to be 1213 K. Maximum recorded temperature on the pyrolysis experiment was 690 K. The commercial boPET purchased for the collector assemble might not have such a great reflectance index as found in the literature. Also, the boPET film roughness causes some of the irradiation to be scattered, reducing energy flux. The parabolic dish solar pyrolizer was built and can be seen in Figure 29.



Figure 29 - Assembled parabolic dish solar pyrolyzer.

4.2 ELECTRIC FURNACE BIOMASS PYROLYSIS

The electric furnace *Luffa cylindrica* pyrolysis experiments described in section 3.3 were performed. The thermal degradation of Luffa fibers was visible, as the final temperature increased. Figure 30 portrays the solid biochar obtained at 300, 400, and 500 °C at 2 °C.min⁻¹ heating rate. The visual aspect of solid products was very similar independently of the heating rate. During the pyrolysis process, the Luffa gourd, which initially has a light yellowish color, goes through brown shades and then becomes black, evidencing the biomass carbonification. Significant volume shrinkage was also observed as the final pyrolysis temperature rose because of the loss of volatile products. The Luffa fibers, which are very resistant in their initial form, also become weak and brittle due to the thermal depolymerization of the biomass components.

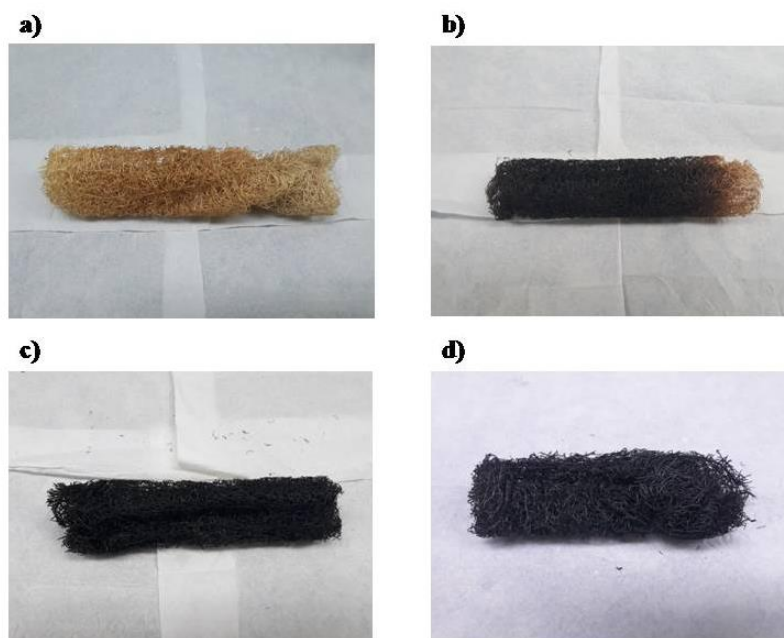


Figure 30 - Biochars obtained from laboratory-scale pyrolysis of *Luffa cylindrica* at the final temperatures of **a)** Non pyrolyzed Luffa; **b)** B300-2; **c)** B400-2; **d)** B500-2.

The sponge gourds and the biochars were weighted, and the percentile char yield was calculated for every experiment as presented in Figure 31. For every investigated heating rate at 300 °C, around 75% of the initial mass was present in the solid product. Below this temperature, hemicelluloses are the only major component of lignocellulosic biomass to thermally degrade in large proportions (MOHAN; PITTMAN; PHILIP, 2017; TANOBE et al., 2005; WANG et al., 2017). This result indicates that the pyrolysis of hemicelluloses is a fast kinetics event, which resonates with literature, which describes it as a low activation energy process, due to the weak heteropolymeric glycosidic bonds and the amorphous branched structure of hemicelluloses (SHEN; GU; BRIDGWATER, 2010; STEFANIDIS et al., 2014). This 25 % mass loss is coherent with the hemicellulose content on *Luffa cylindrica* fibers from literature (Table 2), which usually is around 15 to 20 wt %, and the water content found in TG analysis from literature, which was found to be around 5 % (Figure 23).

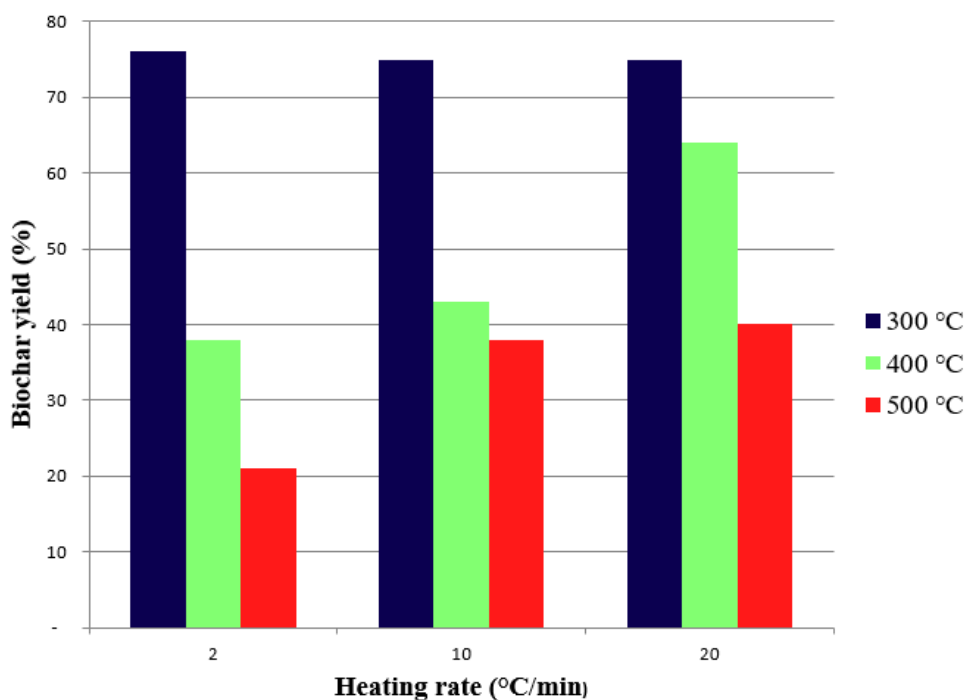


Figure 31 - *Luffa cylindrica* biochar yields from electric furnace pyrolysis.

At the 400 °C final pyrolysis temperature a different trend is observed. The greater the heating rate is, the fewer volatile products are produced, resulting in larger biochar yields. In the temperature range of 300 to 400 °C, two major biomass pyrolysis events occur: degradation of cellulose, the major component of *Luffa cylindrica*, and the primary reactions of depolymerization of lignin (LIN et al., 2009; SHEN et al., 2010a; STEFANIDIS et al., 2014). Considering that the cellulose/lignin ratio in *Luffa cylindrica* is usually around 6:1 or lower (SEKI et al., 2011; SIQUEIRA et al., 2013; TANOBE et al., 2005) it is safe to say that most of the mass loss in the 300 to 400 °C range is due to the de pyrolysis of cellulose. Furthermore, primary pyrolysis reactions of lignin below 400 °C involve partial polymer depolymerization by the cleavage of ether and ester polymeric bonds, while saturated C-C polymeric bonds are still preserved, resulting in a conservation of up to 60% of lignin initial mass (KAWAMOTO, 2017; LEISOLA; PASTINEN; AXE, 2012). Cellulose degradation, therefore, is a kinetically slower event when compared to hemicellulose thermal degradation. Although cellulose monomers are linked with glycosidic bonds similar to those found in hemicelluloses, the organized homopolymeric crystalline structure of cellulose grants its higher stability, increasing pyrolysis

activation energy, which influences the reaction kinetics (KUMAR GUPTA et al., 2019; WANG et al., 2017).

Finally, in 500 °C final pyrolysis temperature experiments, it was observed further mass loss due to the formation of volatiles. In the slower heating rate pyrolysis reaction, *Luffa cylindrica* biomass was submitted to high-temperature conditions long enough for the thermal degradation of all three major components. Some saturated C-C bonds of lignin side-chains crack, resulting in a large production of guaiacols/syringols monomers, that are further degraded due to secondary reactions (ASMADI; KAWAMOTO; SAKA, 2011; BREBU; VASILE, 2010; SHEN et al., 2010a). In the 10 °C.min⁻¹ pyrolysis experiment, a much smaller mass loss was observed. This result indicates that the degradation of lignin is a very time-dependent process at the temperatures at which *Luffa cylindrica* was submitted in this study. In the 20 °C.min⁻¹ pyrolysis, the cellulose content that did not fully degrade at 400 °C had enough reaction time to satisfy its pyrolysis kinetics, resulting in a large decrease in biochar yield.

4.3 SOLAR BIOMASS PYROLYSIS

A solar pyrolysis experiment was conducted on the solar dish pyrolyzer from 12:30 to 13:30 h on 26/07/2021. A 5.80 g *Luffa* gourd was placed in the reactor, and 2.95 g of biochar was obtained, resulting in a 50.8 wt % yield. Figure 32 is a picture of the resulting biochar.



Figure 32 - Biochar obtained from solar pyrolysis.

The pyrolysis experiment had a maximum temperature of 417.4 °C, and a final temperature of 401.9 °C resulting in average heating of 5.5 °C.min⁻¹. Figure 33 shows the temperature evolution over the pyrolysis experiment. Considering the final temperature, the biochar should not have any hemicellulose content, while lignin molecules are well preserved. The 50.8 % biochar yield indicates that cellulose content is partially preserved, despite the high reached temperature. Similar to what was observed in the B400-10 and B400-20 biochars, there was not enough time for cellulose to fully degrade. In fact, given the obtained solar biochar yield, it is concluded that the residual cellulose content of the solar biochar is higher than B400-10 and lower than B400-20. Cellulose content was expected to be lower than B400-10 since the average heating rate was faster (5.5 °C.min⁻¹). This result can be explained by pyrolysis reactors designs. The electric furnace reactor receives heat from the entire cylindrical surface, which makes the inner temperature to be more homogeneous. The heat in the solar design comes from the bottom surface of the reactor, causing a temperature gradient inside the reactor volume.

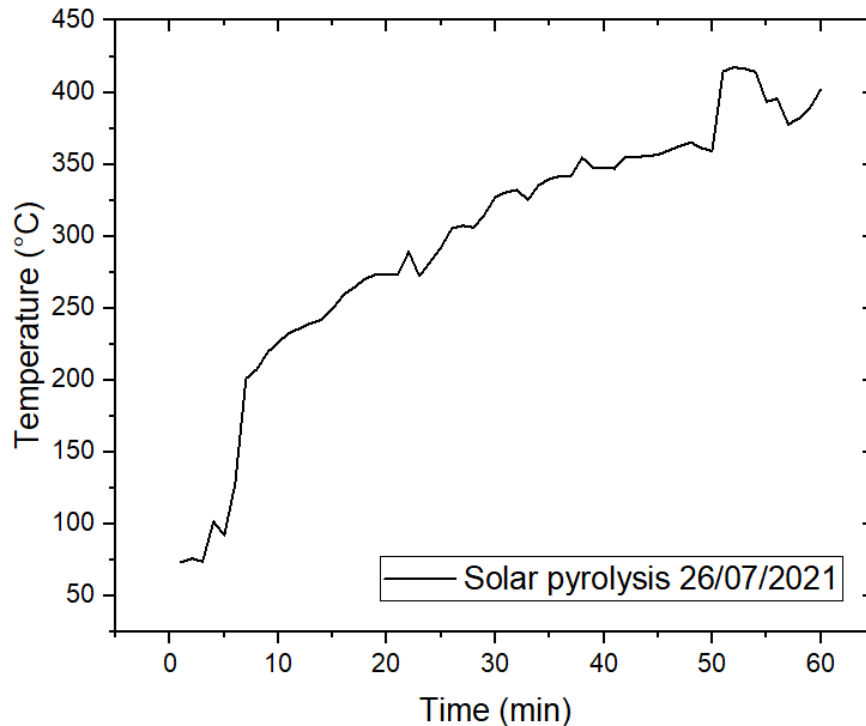


Figure 33 - Temperature evolution over the parabolic dish solar pyrolysis.

4.4 BIOMASS AND BIOCHAR CHARACTERIZATION

4.4.1 Ultimate Analysis

The performed ultimate analysis of *Luffa cylindrica* comprises the percentile content of carbon, hydrogen, nitrogen, oxygen, and sulfur elements. The obtained results are available in Table 10.

Table 10 - Ultimate analysis (wt %) of *Luffa cylindrica* fibers.

Duplicate	Carbon	Hydrogen	Nitrogen	Oxygen	Sulfur
1	43.57	5.71	0.21	44.14	1.24
2	43.73	5.79	0.11	44.70	1.33
Average	43.65	5.75	0.16	44.42	1.28

The obtained result is in resonance with what is found in the literature (Table 3). The high oxygen content indicates that *Luffa cylindrica* is comprised of highly polar structures, which is beneficial to the ion exchange adsorption mechanism. However, the adsorption performance of raw biomass is usually poor when compared to activated biochars due to the lower surface area.

A recent study has proposed an ultimate analysis correlation to the higher heating value of lignocellulosic biomass with absolute percentage errors lower than 3% (HUANG; LO, 2020). According to this correlation, which is available in Equation 6, the HHV of *Luffa cylindrica* fibers is predicted to be 17.0 MJ.kg⁻¹. As can be inferred from the correlation, the high oxygen content of Luffa fibers is detrimental to its HHV. As pyrolysis progresses, oxygen content decreases due to charring reactions, which results in higher HHV. The low nitrogen and sulfur content on the sample is a very important result since the combustion of these elements generates pollutant oxides (NO_x and SO_x), which have adverse effects on the ozone layer in the troposphere.

$$HHV = 0.3443C + 1.192H - 0.113O - 0.0240N + 0.093S \quad (6)$$

4.4.2 X-Ray Fluorescence Spectrometry

Luffa cylindrica fibers were submitted to qualitative X-Ray Fluorescence Spectrometry to help elucidate the inorganic elemental composition of this biomass. The mass percentile content is available in Table 11.

Table 11 – *Luffa cylindrica* X-Ray Fluorescence Spectrometry qualitative result.

Element	Content (wt %)
Potassium	0.468
Calcium	0.419
Copper	0.159
Iron	0.133
Phosphorus	0.021
Sulfur	0.013

As was expected, only a small mass fraction of the biomass is composed of inorganic constituents, due to the organic nature of plant matter. The elements spotted via qualitative XRF are linked with many metabolic functions of *Luffa cylindrica*. Potassium plays a major role as a stabilizer in metabolism and cellular hydrostatic pressure, growth, and responses to environmental changes (DREYER; UOZUMI, 2011). Calcium is required for structural roles in the cell wall and membranes, as a counter-cation for inorganic and organic anions, and as an intracellular messenger (WHITE; BROADLEY, 2003). Copper acts as a structural element in reglementary proteins and participates in photosynthetic electron transport, mitochondrial respiration, and hormone signaling (YRUELA, 2005). Iron plays a critical role in metabolic processes such as DNA synthesis, respiration, and photosynthesis (ROUT; SAHOO, 2015). Phosphorus is an essential element for plant metabolism and growth since it is present in the highly energetic adenosine triphosphate (ATP) molecules produced in photosynthesis and in nucleic acids (HASANUZZAMAN et al., 2018). Finally, sulfur is present in an array of plant metabolic functions, since it is a unique mineral, capable of transitioning to a wide range of oxidations states.

4.4.3 Thermogravimetric Analysis

Thermogravimetric and Derivative Thermogravimetric Analysis of *Luffa cylindrica* fibers and *Luffa cylindrica* biochars were performed as described in the methodology section of this

work. Figure 34 displays the TGA/DTG curves for the dry and clean Luffa fibers. Appendix I compiles TGA/DTG curves for every tested biochar sample.

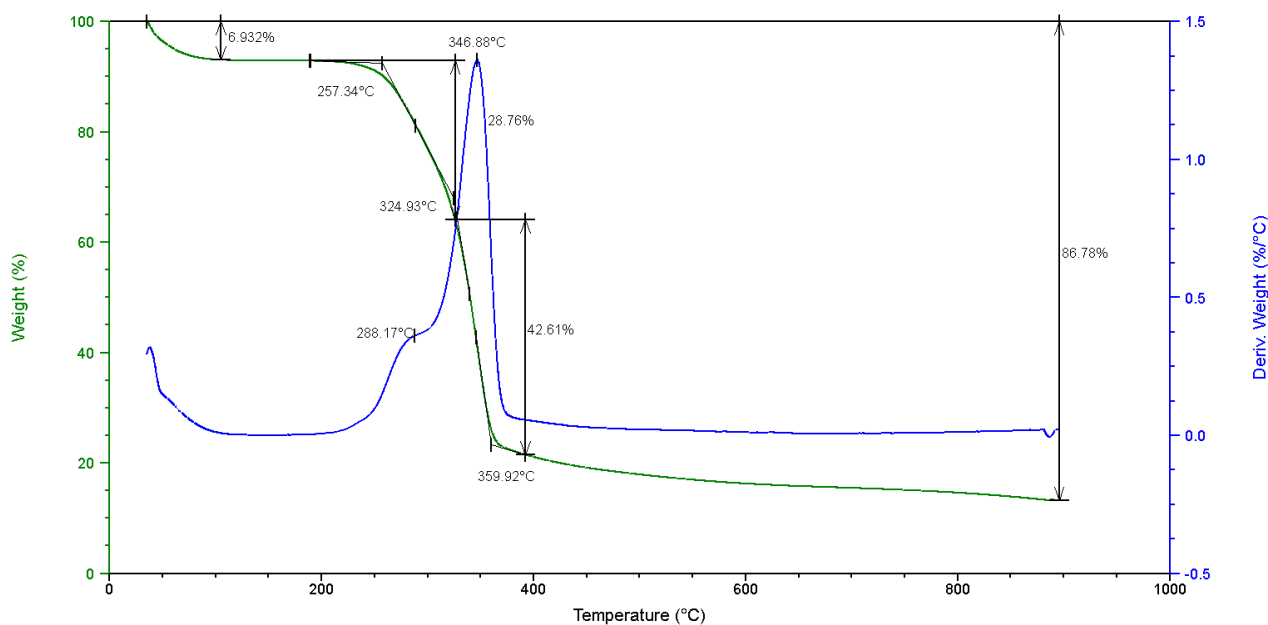


Figure 34 - TGA/DTG curves of Luffa cylindrica fibers.

The obtained *Luffa cylindrica* TGA/DTG curves present great similarity to the ones found in the literature for this biomass type (BOYNARD; D'ALMEIDA, 2000; NAGARAJAGANESH; MURALIKANNAN, 2016; PREMALATHA et al., 2019; SEKI et al., 2011; TANOBE et al., 2005; ZHANG et al., 2017). The first event observed in the analysis is the 6.9 % mass loss due to the evaporation of absorbed water at low temperatures (< 120 °C). This value is similar to what has been observed in the literature, as Figure 23 shows.

The second observed event, related to the pyrolysis of hemicelluloses, happens between 257 and 325 °C and peaking at 288 °C, resulting in a 28.8 % mass loss. Hemicellulose content on Luffa fibers is usually around 15 to 20 % (Table 2). This discrepancy is observed due to the overlapping of cellulose and hemicellulose pyrolysis events, which makes it difficult to point out the temperature at which one event has finished and the other has begun.

The third event, related to cellulose pyrolysis, is a 42.6% mass loss, observable between 325 and 359 °C and peaking at 347 °C. The mass loss due to the pyrolysis of cellulose on Luffa

fibers is found to be underrated on the TG analysis, as cellulose content is higher than 60 wt % in literature studies (Table 2). The overlapping of cellulose and hemicellulose pyrolysis events could explain this difference for the most part.

Pyrolysis on lignin, contrary to the other biopolymers, did not appear as an observable DTG peak, given its minor proportion on *Luffa cylindrica* fibers. The degradation of this biopolymer can be seen, however, as a slow and steady 8.8 % mass loss event from 359 °C onwards. This mass loss is coherent with what is found in the literature (Table 2). Total mass loss at 900 °C was 86.8 %, leaving 13.2 wt % of ashes, which resonates with literature (Table 2).

Pyrolysis events on the Thermogravimetric analysis of Luffa fibers are far more discernible on DTG curves, as can be seen in figure 34. Therefore, to facilitate the observation and study of the thermal degradation of Luffa, Differential Thermogravimetric curves of biochars obtained from 2 °C/min electrical furnace pyrolysis are available in figure 35. The first event observed on every curve is the evaporation of adsorbed water, once biochars were not kept in a 100% humidity-free environment after pyrolysis. However, all biochars had lower water content if compared to raw Luffa fibers because the sponge, as a vegetable material, had not only adsorbed water molecules on the surface but its inner structures.

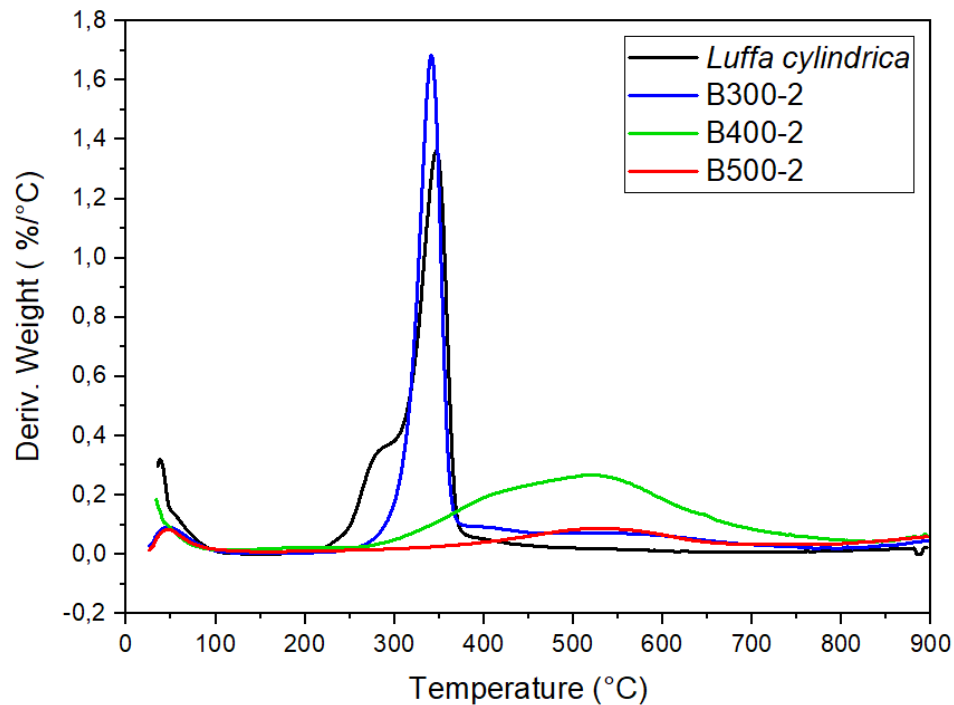


Figure 35 - DTG curves of *Luffa cylindrica* and *Luffa cylindrica* biochar from 2 °C/min pyrolysis experiments.

As was expected, the 288 °C hemicellulose peak was the first to disappear on the B300-2 curve, due to the degradation of this biopolymer in the pyrolysis experiment. The degradation of cellulose in B300-2 peaked at 341.2 °C. Different from what is observed on the Luffa DTG curve, two small peaks correlated to primary and secondary pyrolysis reactions of lignin can be seen around 400 and 550 °C (KAWAMOTO, 2017) on the B400-2 curve. As other polymers pyrolyze, lignin content becomes more significant.

B400-2 DTG curve does not present any observable cellulose peak. The degradation of cellulose, as was expected, happened in the pyrolysis electrical furnace experiments, in which the biomass was submitted to temperatures up to 400 °C. The degradation of lignin, however, has its visibility enhanced. Lignin degradation was observed from 368.7 °C onwards. Two peaks correlated to primary and secondary pyrolysis reactions of lignin are observed at 416.4 and 523.6 °C.

Finally, on the B500-2 DTG, the only observable event, other than the water evaporation, is the secondary pyrolysis reactions of lignin. This event is reported to have begun at 418.0 °C, peaking at 519.5 °C.

Differential Thermogravimetric curves of biochars obtained from 10 °C.min⁻¹ electrical furnace pyrolysis are available in figure 36. B300-2 and B300-10 Differential Thermogravimetric curves pyrolysis show a remarkable similarity. The hemicellulose peak cannot be found in either of them, while the strong cellulose peak is only slightly shifted from 341.2 °C to 347.7 °C.

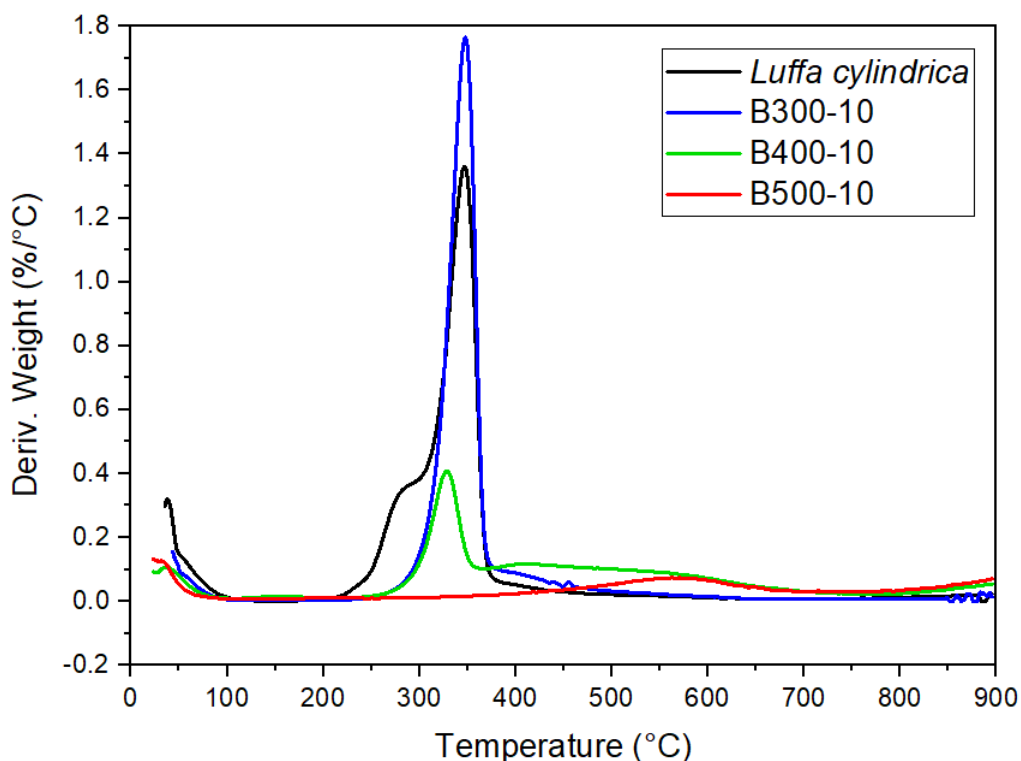


Figure 36 - DTG curves of *Luffa cylindrica* and *Luffa cylindrica* biochar from 10 °C/min pyrolysis experiments.

The greatest difference observed in the DTG results from 2 °C.min⁻¹ and 10 °C.min⁻¹ pyrolysis biochars reside on the 400 °C curves. The cellulose peak is not observed on the B400-2 curve while it is still present on the B400-10 curve. The higher heating rate resulted in incomplete cellulose pyrolysis.

Lastly, B500-10 TGA/DTG curves are again similar to the B500-2 ones. The remaining cellulose content was degraded and primary pyrolysis of lignin happened to an expressive extent in the electrical furnace pyrolysis, since none of the peaks related to these events is found on the curve in question. The secondary pyrolysis reactions of the lignin peak are observed from 445.3 to 645.7 °C, peaking at 562.8 °C.

Differential Thermogravimetric curves of biochars obtained from 20 °C.min⁻¹ electrical furnace pyrolysis are available in figure 37. DTG curves of biochars obtained from 300 °C final temperature pyrolyzes were very similar at all heating rates. The hemicellulose peak cannot be found in either of them, while the strong cellulose peak is only slightly shifted to 336.8 °C on the B300-20 DTG curve.

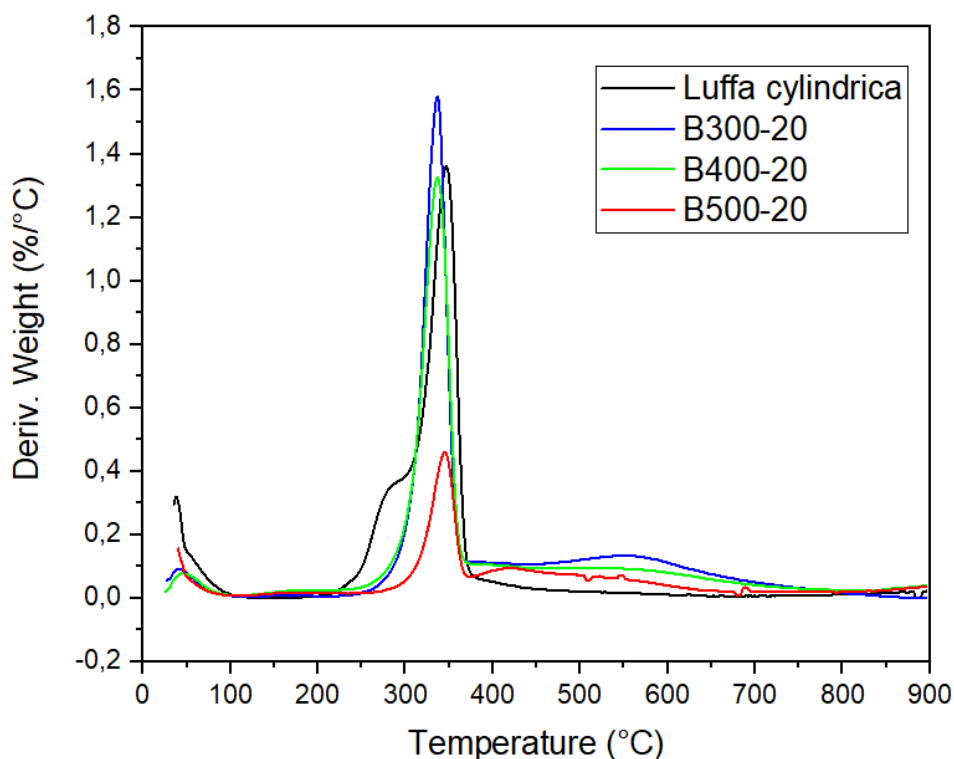


Figure 37 - DTG curves of *Luffa cylindrica* and *Luffa cylindrica* biochar from 20 °C/min pyrolysis experiments.

The B300-20 and B400-20 curves obtained from DTG analysis present great similarities. This result indicates that cellulose degradation in the 300 to 400 °C temperature range did not happen to the expected extent due to the faster heating rate. It is still possible to observe the cellulose

peak even at the B500-20 DTG curve. Lignin degradation was also minimal since the lignin primary pyrolysis peak is observable even in the curve of the highest pyrolysis temperature biochar. Therefore, 20 °C.min⁻¹ pyrolysis presented a very incomplete pyrolysis behavior, resulting in great preservation of cellulose and lignin structures.

Finally, the Differential Thermogravimetric curve of the solar biochar is available in figure 38. No hemicellulose peak can be found in the solar biochar DTG curve since the pyrolysis experiment was conducted at temperatures up to 417 °C. On the other hand, the characteristic cellulose peak is still present, however quite diminished when compared to the *Luffa cylindrica* DTG curve. The cellulose content in the solar biochar is between that of the B400-10 and B400-20 biochars, as the cellulose peak in the solar DTG curve is also of intermediate proportions. Lignin content is still well-preserved, as both peaks associated with lignin pyrolysis are present.

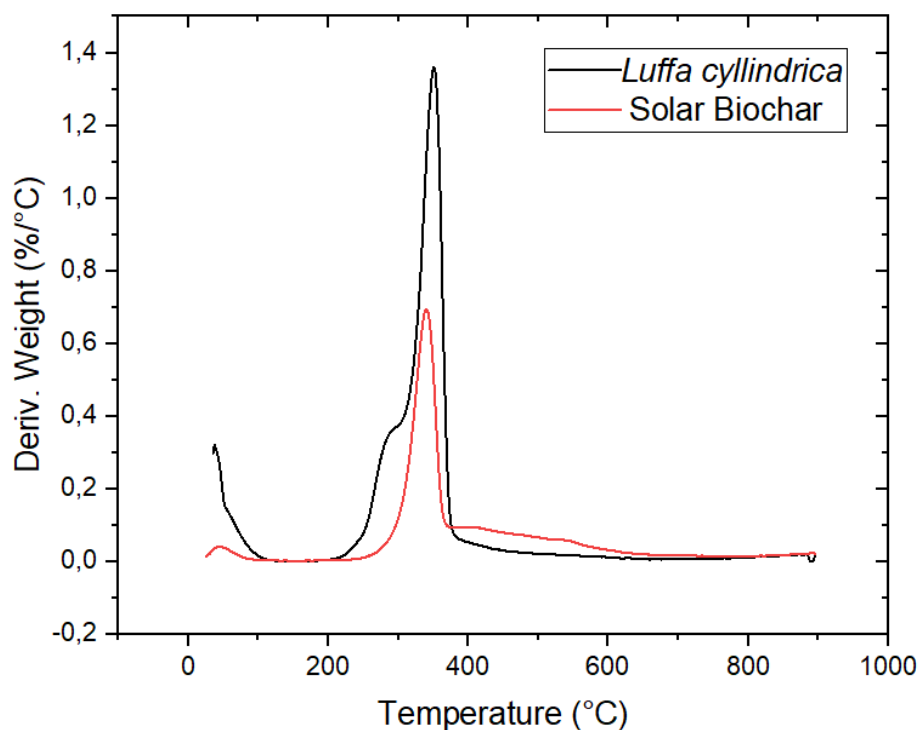


Figure 38 - DTG curves of *Luffa cylindrica* and *Luffa cylindrica* solar biochar.

4.4.4 Fourier Transform Infrared Spectroscopy

The Infrared absorption spectrum of *Luffa cylindrica* acquired by FTIR analysis is displayed in figure 39.

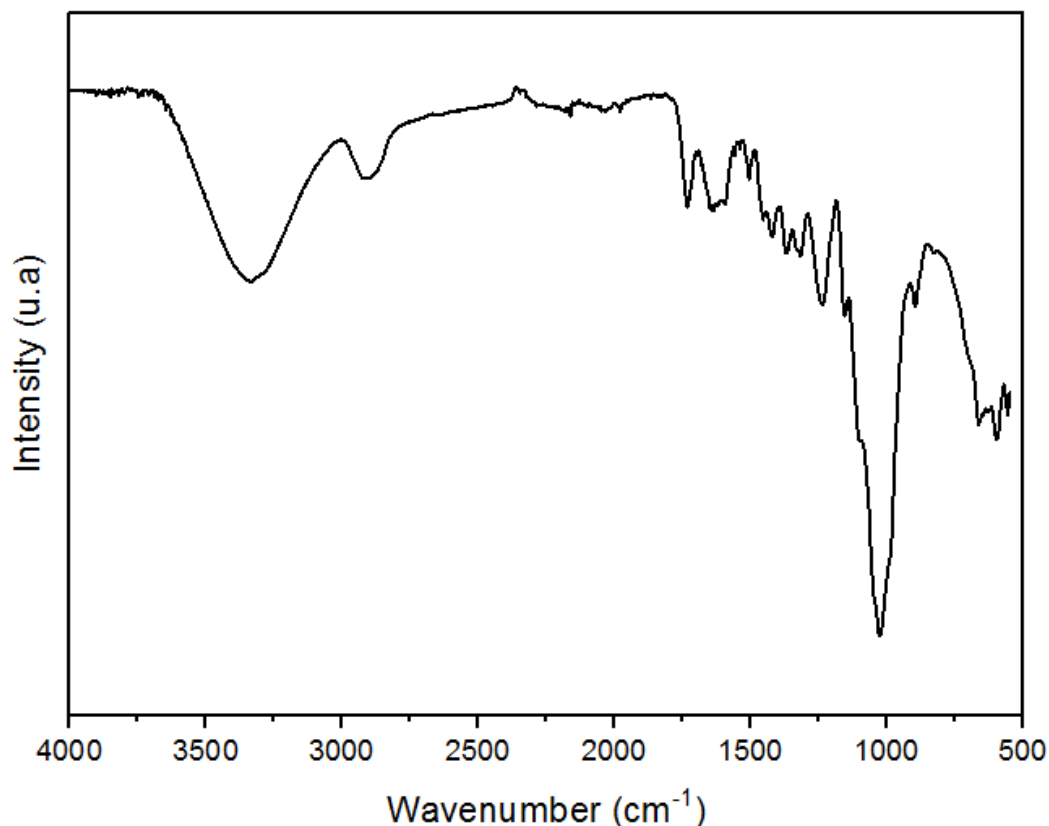


Figure 39 - Infrared absorption spectrum of *Luffa cylindrica*.

Except for small shifts in the functional groups, the obtained spectrum in this study is similar to the ones present in literature (NAGARAJAGANESH; MURALIKANNAN, 2016; SEKI et al., 2011; SIQUEIRA et al., 2013; TANOBE et al., 2005) and exposed in section 2.2.1 of this document. Some not cataloged peaks of *Luffa cylindrica* on specific literature were spotted and assigned to functional groups taking other biomass studies as a reference (XU et al., 2013; YANG et al., 2007). The interpretation of the signals observed on the FTIR spectrum of *Luffa cylindrica* is given in Table 12.

Table 12. Interpretation of FTIR Peaks of *Luffa cylindrica* fibers.

Wavenumber (cm ⁻¹)	Assignment
3335	OH stretching
2905	Saturated C–H stretching

1733	C=O stretching (acetyl or carboxylic acid)
1642	OH bending (absorbed water)
1597	C=C stretching of aromatic
1506	C-H aromatic bending
1454	CH ₂ symmetric bending (lignin)
1425	O-H in-plane bending
1372	C-H bending
1325	C-O stretching
1239	C-O-C stretching (hemicellulose)
1156	Asymmetric bridge C-OR-C stretching (cellulose)
1098	Anhydroglucose ring
1027	C-OR stretching (cellulose and hemicellulose)

Biochars obtained from electrical furnace pyrolysis were also submitted to FTIR analysis. Figure 40 displays the IR absorption spectrums of 2 °C.min⁻¹ pyrolysis experiments. As expected, as the final pyrolysis temperature increases, most functional groups present on the *Luffa cylindrica* spectrum start to fade due to the carbonization of the solid phase. The wide hydroxyl peak at 3335 cm⁻¹ decreases rapidly even at 300 °C, mainly by the decomposition of hemicelluloses, while at 400 °C, a high enough temperature to degrade cellulose molecules, the peak is quite soft. At 500 °C lignin is partially degraded and no hydroxyl peak can be found in the biochar spectrum. A very similar trend can be observed on the 2905 cm⁻¹ C-H stretching peak due to the carbonization of the solid phase.

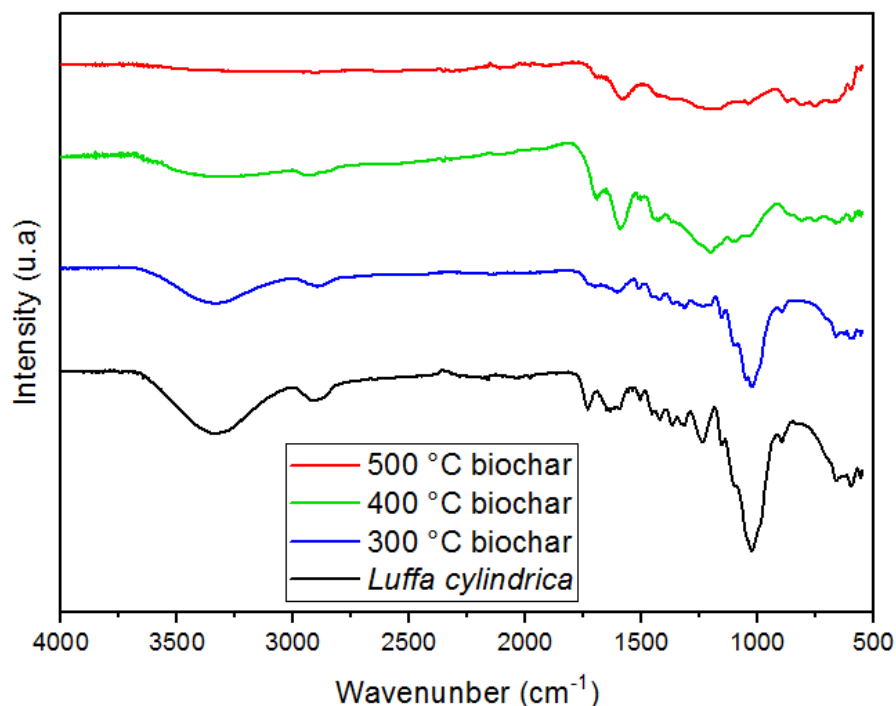


Figure 40 - Infrared absorption spectrum of *Luffa cylindrica* and *Luffa cylindrica* biochar from 2 °C.min⁻¹ pyrolysis experiments.

At the 1733 cm⁻¹ C=O stretching peak, a different phenomenon is observed: the initial C=O bond content initially decreases at 300 °C, due to the degradation of hemicelluloses, biopolymers with some monomers with carbonyl groups. However, as the final pyrolysis temperature rises to 400 °C, this peak is rather enhanced due to the formation of C=O bonds. The thermal degradation mechanisms of all three major components of lignocellulosic biomass have carbonyl-containing intermediate products (LIN et al., 2009; NAKAMURA; KAWAMOTO; SAKA, 2008; SHEN; GU; BRIDGWATER, 2010). Once pyrolysis reactions mechanisms come to an end, these intermediate products are further degraded resulting in a decrease in the 1733 cm⁻¹ C=O stretching peak on the B500-2 spectrum. The 1642 cm⁻¹ absorbed water peak is present only on the *Luffa* spectrum due to the high pyrolysis temperatures biochars were submitted to.

The C=C stretching of aromatic compounds peak at 1597 cm⁻¹ in the *Luffa* spectrum is due mainly to lignin, the only aromatic major component of lignocellulosic biomass. At 300 °C, this peak is softened by the volatilization of minor aromatic constituents, once lignin molecules

are stable at this temperature. At 400 °C, however, the 1597 cm⁻¹ peak is enhanced evidencing the formation of aromatic species. The thermal decomposition of cellulose produces great quantities of furanoses (furfural, hydroxymethylfurfural, etc.), which are aromatic heterocyclic compounds. At 500 °C the peak is softened once again by the volatilization of furanoses and decomposition of lignin.

Peaks from 1506 to 1325 cm⁻¹ follow the same trend, fading as temperature increases due to the degradation of Luffa fibers and the volatilization of products. The 1239 cm⁻¹ C–O–C stretching peak, however, which is correlated to the glycosidic bond on hemicelluloses, is only found at the Luffa spectrum, once at 300 °C hemicelluloses have already been degraded. 1156, 1098, and 1027 peaks are correlated to both cellulose and hemicelluloses, given the chemical similarity between these biopolymers. Therefore, at 300 °C, these peaks are softened, while at 400 °C, they are not found in the biochar spectrum. Special attention is given to the strong 1027 cm⁻¹ peak, relative to the stretching vibration of the characteristic glycosidic bond C-OR found on cellulose and hemicellulose polymer chains.

At 1205 cm⁻¹, a peak is observed in the B400-2 spectrum. This peak is assigned in literature to the C-O bond in phenolic structures (YANG et al., 2007). This result can be correlated to lignin primary pyrolysis phenolic products, like coniferyl alcohol, coniferyl aldehyde, isoeugenol, etc (KAWAMOTO, 2017). At 500 °C these products could have been further degraded or volatilized.

IR absorption spectrums of biochars obtained in 10 °C.min⁻¹ pyrolysis experiments were obtained via FTIR analysis and are displayed in figure 41.

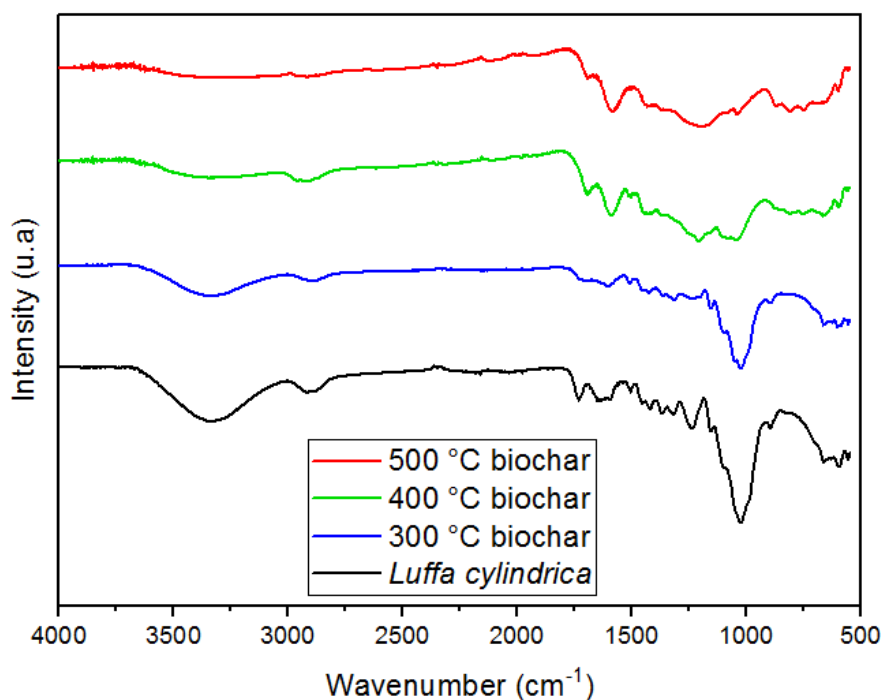


Figure 41 - Infrared absorption spectrum of *Luffa cylindrica* and *Luffa cylindrica* biochar from 10 °C.min⁻¹ pyrolysis experiments.

IR absorption spectrums of 10 °C.min⁻¹ pyrolysis experiments support the discussion raised in section 4.2 of this document. The 300 °C spectrums from both 2 °C.min⁻¹ and 10 °C.min⁻¹ pyrolysis biochars are very similar, which indicates that the pyrolysis of hemicelluloses is a fast kinetics event, given that at this temperature, they are the only major component of *Luffa cylindrica* to degrade in large proportions (WANG et al., 2017). Hemicelluloses are heteropolymers with amorphous branched structures whose monomers are bonded by weak glycosidic bonds (SHEN; GU; BRIDGWATER, 2010; STEFANIDIS et al., 2014).

At 400 °C, however, the spectrums from 2 °C.min⁻¹ and 10 °C.min⁻¹ pyrolysis biochars present significant differences. The 1027 cm⁻¹ C-OR peak is still preserved on the B400-10 curve. Pyrolysis of cellulose was not complete at these conditions due to a slower degradation kinetic in comparison to hemicelluloses. The organized homopolymeric crystalline structure of cellulose grants its higher stability, increasing pyrolysis activation energy, which influences the reaction kinetics (KUMAR GUPTA et al., 2019; WANG et al., 2017). The 2905 cm⁻¹ C-H stretching peak was also found to be more preserved at the B400-10 curve, conveying an overall less carbonized

biochar on faster heating rates. The 2905 cm^{-1} C–H aromatic bending peak is more preeminent on the B400-10 spectrum, which indicates that primary pyrolysis reactions of lignin occurred to a lesser extent at this heating rate.

At $500\text{ }^{\circ}\text{C}$, more differences were observed. B500-2 spectrum was found to be much flatter altogether, showing that in the $10\text{ }^{\circ}\text{C}\cdot\text{min}^{-1}$ pyrolyzes more functional groups are preserved. The C=C stretching of aromatic compounds peak at 1597 cm^{-1} is specially enhanced in the B500-10 spectrum. As it has been discussed, the degradation of cellulose results in the formation of large proportions of furanoses, which are aromatic compounds. In $2\text{ }^{\circ}\text{C}\cdot\text{min}^{-1}$ experiments, these furanoses were degraded or volatilized at $500\text{ }^{\circ}\text{C}$. In $10\text{ }^{\circ}\text{C}/\text{min}$ pyrolysis, however, these compounds are still present on the biochar. Another important difference is in the conservation of the 1205 cm^{-1} peak correlated to the C–O bond in phenolic structures of products from lignin primary pyrolysis reactions. This peak cannot be found in the B500-2 spectrum, once these products were already further degraded or volatilized. Therefore, the thermal decomposition of both, cellulose and lignin, were affected by the heating rate increase.

IR absorption spectrums of $20\text{ }^{\circ}\text{C}\cdot\text{min}^{-1}$ pyrolysis experiments were obtained via FTIR analysis and are displayed in figure 42.

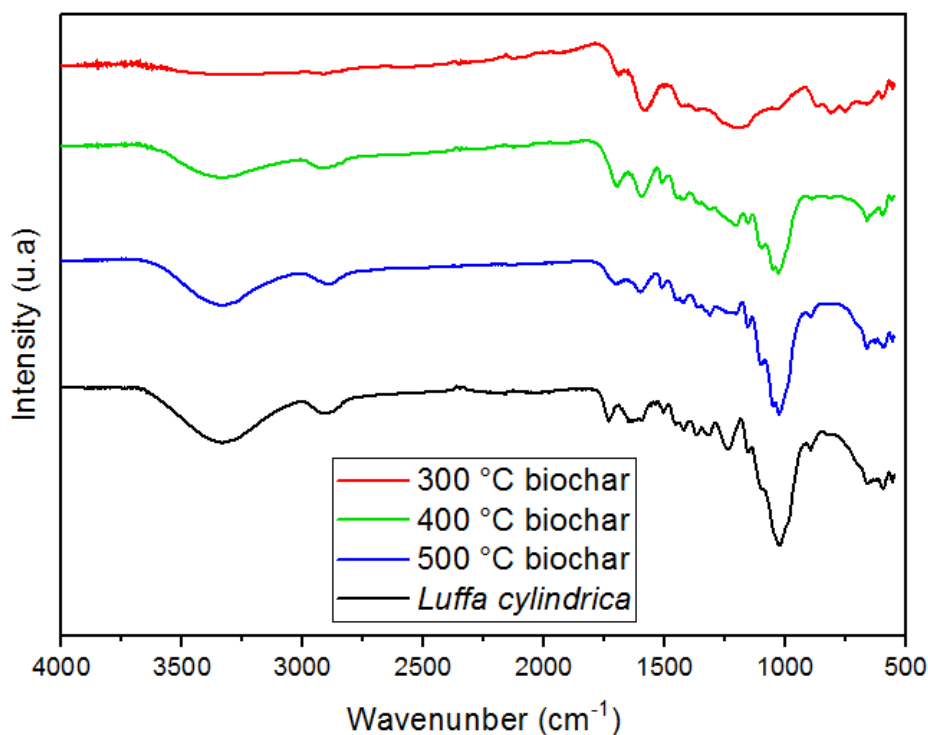


Figure 42 - Infrared absorption spectrum of *Luffa cylindrica* and *Luffa cylindrica* biochar from 20 °C/min pyrolysis experiments.

The effects observed in the 10 °C.min⁻¹ pyrolysis spectra were further enhanced in the 20 °C.min⁻¹ FTIR curves. Signals are far more preserved at this higher heating rate due to the shorter reaction time. The 1027 cm⁻¹ peak depth for the B300-20 spectrum indicates that even the thermal decomposition of hemicelluloses was not as complete as it was in the previous experiments with slower heating rates.

This peak is still very pronounced in the B400-20 curve, showing that the pyrolysis of cellulose is a process highly dependent on the reaction time. The well preserved 3335 cm⁻¹ O-H stretching and 2905 cm⁻¹ saturated C-H stretching peaks evidence that a good proportion of *Luffa cylindrica* biopolymers are still present on the solid phase even at 400 °C. The 1597 cm⁻¹ peak, assigned to the C=C bond on aromatic compounds is softer in the B400-20 curve when compared to the other heating rates, due to less formation of furanoses, products of the cellulose decomposition. The 1205 cm⁻¹ peak, assigned to the phenolic products of lignin primary

pyrolysis reactions is also softer if compared to the B400-2 curve, conveying that the degradation of this product was also not as extensive as in faster heating rates experiments.

Finally, the B500-20 spectrum was found to be very similar to the B500-10 one. This result evidences that the cellulose and lignin decomposition processes that didn't have enough time to happen to the expected extent at 400 °C, occurred in the 400 to 500 °C interval.

IR spectrum of the solar biochar and *Luffa cylindrica* and displayed in figure 43. The solar biochar spectrum is similar to those of the B400-10 and B400-20 samples. The observable softening of the hydroxyl peak at 3335 cm^{-1} and the 2905 cm^{-1} C-H stretching peak confirms the thermal degradation of lignocellulosic biomass biopolymers. The 1027 cm^{-1} C-OR peak is still observable due to the incomplete pyrolysis of cellulose, which resonates with the DTG result. The 1733 cm^{-1} C=O peak and the C=C stretching of aromatic compounds peak at 1597 cm^{-1} , similarly to what was overserved on the electric furnace spectra, are enhanced due to the formation of pyrolysis products with carbonyl-containing products and aromatic products. The soft 1205 cm^{-1} C-O peak correlated to the phenolic lignin products conveys that some early stages of lignin pyrolysis have happened through the experiment. Overall, most peaks from the *Luffa cylindrica* spectrum are softened or not found on the solar biochar spectra due to the pyrolysis process.

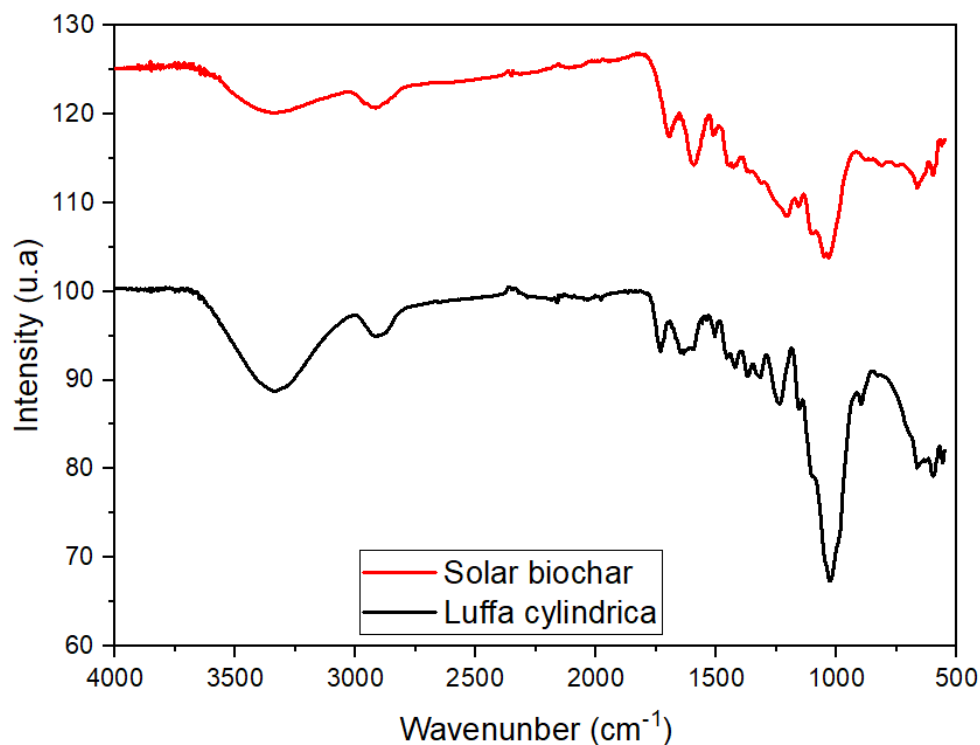


Figure 43 - Infrared absorption spectrum of *Luffa cylindrica* and *Luffa cylindrica* solar biochar.

4.4.5 Heat of Combustion Analysis

The higher heating value is a critical property for chars and other fuels. Once this work focuses on *Luffa cylindrica* pyrolysis with emphasis on its biochars, it was of utter importance to investigate the energetic potential of these products. It is noteworthy that a good route for the disposal of biochars would be to use them as fuel after their use as adsorbents for aqueous contaminants. Figure 44 presents HHVs for the *Luffa cylindrica* sample and all produced biochars. HHV of produced biochars is considered relatively high. For comparison, *eucalyptus* charcoal, one of the most widespread solid fuels in Brazil had an average 31.28 MJ.kg⁻¹ higher heating value in a recent study (DE PAULA PROTÁSIO et al., 2021).

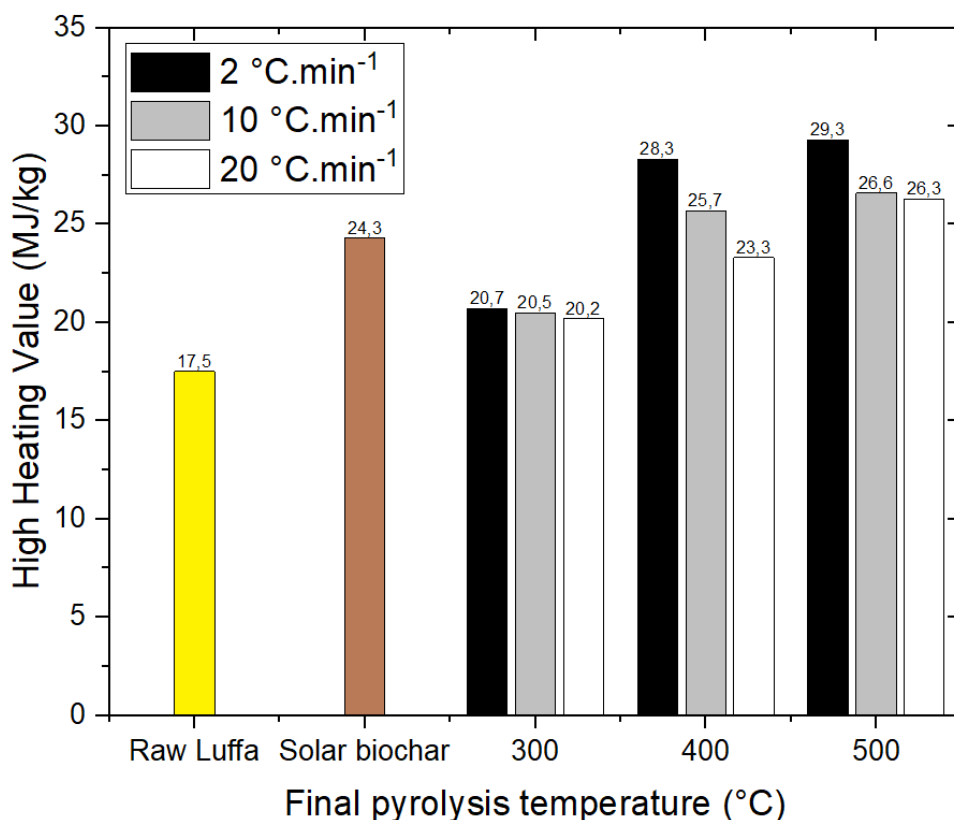


Figure 44 - HHV of *Luffa cylindrica* and produced biochars.

Luffa cylindrica's experimental HHV (17.5 MJ.kg⁻¹) is very close to the prediction made via the ultimate analysis correlation (17.0 MJ.kg⁻¹), with an absolute error of only 2.8%. This low HHV is mainly due to the high cellulose-hemicellulose to lignin ratio of this biomass, since the HHV for the first two biopolymers are reported to be around 18.6 MJ.kg⁻¹, while for the latter it ranges from 23.3 to 25.6 MJ/kg on literature (DEMIRBAŞ, 2001). It can be observed as a general trend that the greater the pyrolysis temperature is, the greater is also the HHV, which resonates with the literature (DEMIRBAS, 2006; QIAN et al., 2020). HHV results had also a great correlation with pyrolysis heating rate. Slower heating rates resulted in greater thermal degradation of lignocellulosic biopolymers, producing biochars with higher calorific power.

Higher heating values of studied biochars greatly agreed with TG and FTIR results. As it was seen on the other characterization methods, B300 biochars were very similar, despite the heating rate difference. B400-20 was the only biochar submitted to 400 °C pyrolysis with visible TG and FTIR peaks related to cellulose. Similarly, it had the lowest HHV among B400 biochars.

B500-2, the biochar with the highest HHV (29.3 MJ.kg⁻¹), was also the one with the lower pyrolysis solid yield and overall highest thermal degradation. Solar biochar had an intermediate higher heating value (24.3 MJ.kg⁻¹), which was expected due to the incomplete lignin pyrolysis at the final temperature for this pyrolysis run, 401.9 °C. With an average heating rate of 5.5 °C.min⁻¹, the solar biochar HHV was expected to be between those of B400-2 and B400-10. However, due to greater temperature gradients in the solar reactor arrangement, the HHV was found to be between those of B400-10 and B400-20.

4.4.6 Scanning Electron Microscopy

A qualitative Energy-Dispersive X-Ray Spectroscopy spectrum of *Luffa cylindrica* was obtained utilizing the Scanning Electron Microscope built-in structure (Appendix J). Other than the elements present on the XRF and ultimate analysis, were spotted magnesium, sodium, aluminum, and silicon. Unlike magnesium, sodium is not essential to plant metabolism, while silicon and aluminum may even be toxic to the plant in high concentrations (GUO et al., 2016; MA, 2005; SUBBARAO et al., 2003).

Figure 45 compiles 6 *Luffa cylindrica* micrographs obtained by Scanning Electron Microscopy via secondary electrons detection. A natural Luffa fiber, observable with the naked eye, is magnified in Figure 45-a. For the most part, the rough fiber surface does not have any observable pores that allow for the contact of the external medium with the inner structure. Figure 45-b shows this continuous rough surface with greater detail. This morphology is detrimental to adsorption systems since only a small part of the material is available for solute removal. Only a small tear on the fiber is observable in Figure 45-a at the lower right corner of the micrograph. Similar defects were not found in other sections of the sample. This tear is further magnified in Figure 45-c and even more in Figure 45-d. The highly fibrous inner structure of *Luffa cylindrica* is unveiled. On the top left corner of Figure 45-a, a couple of sharp blade cuts, made in the sample preparation procedure, are observed. These cuts reveal the cross-section structure of *Luffa cylindrica*, which are further magnified in Figure 45-e and Figure 45-f. The interior of the fiber presents itself as a rather compact structure, with small and sparse porosity.

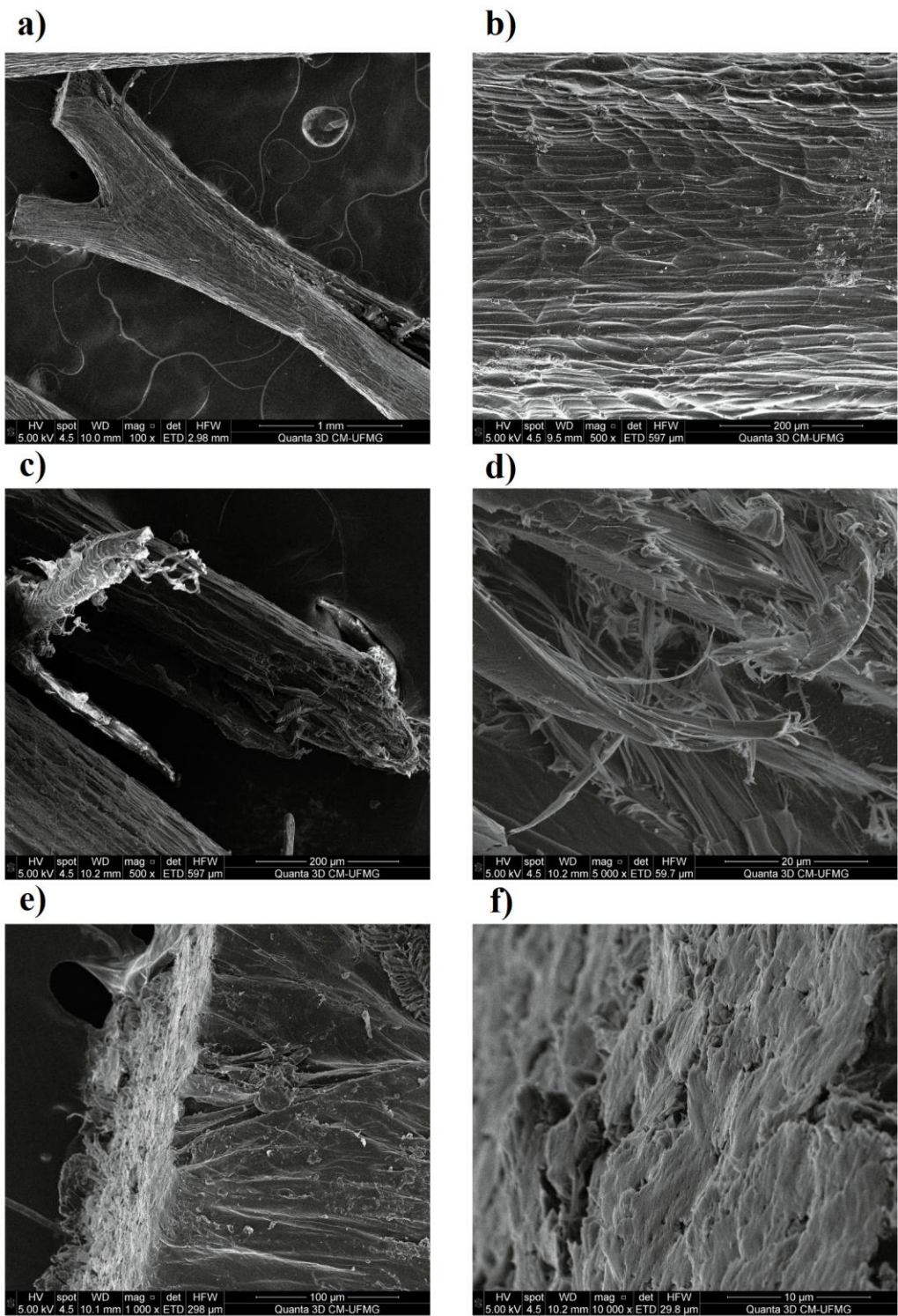


Figure 45 – *Luffa cylindrica* SEM micrographs: **a)** Fiber (X 100); **b)** Fiber surface (X 500); **c)** Natural fiber tear (X 500); **d)** Natural fiber tear up close (X 5000); **e)** Fiber cross section (X 1000); **f)** Fiber cross section up close (X 10000).

The biochar with the highest adsorption capacity was of particular interest for SEM imaging. As will be discussed in section 4.5, biochar B400-2 presented the best result in the preliminary iodine adsorption study. Figure 46 compiles SEM micrographs of such sample. Figures 46-a and 46-b both show that the biochar surface has many cracks and pores, unlike the raw Luffa fiber surface. The cross-section observed in Figure 46-a is further magnified in Figures 46-c and 46-d. Different from what is observed on the Luffa micrographs, the inner structure of the biochar is not compact. Tubular structures with 10 to 50 μm of diameter are observed. During pyrolysis, the mass loss due to the evolution of volatile products causes the surface to break or crack and the inner structure to become more porous, resulting in a fragile, less dense solid phase with a higher surface area.

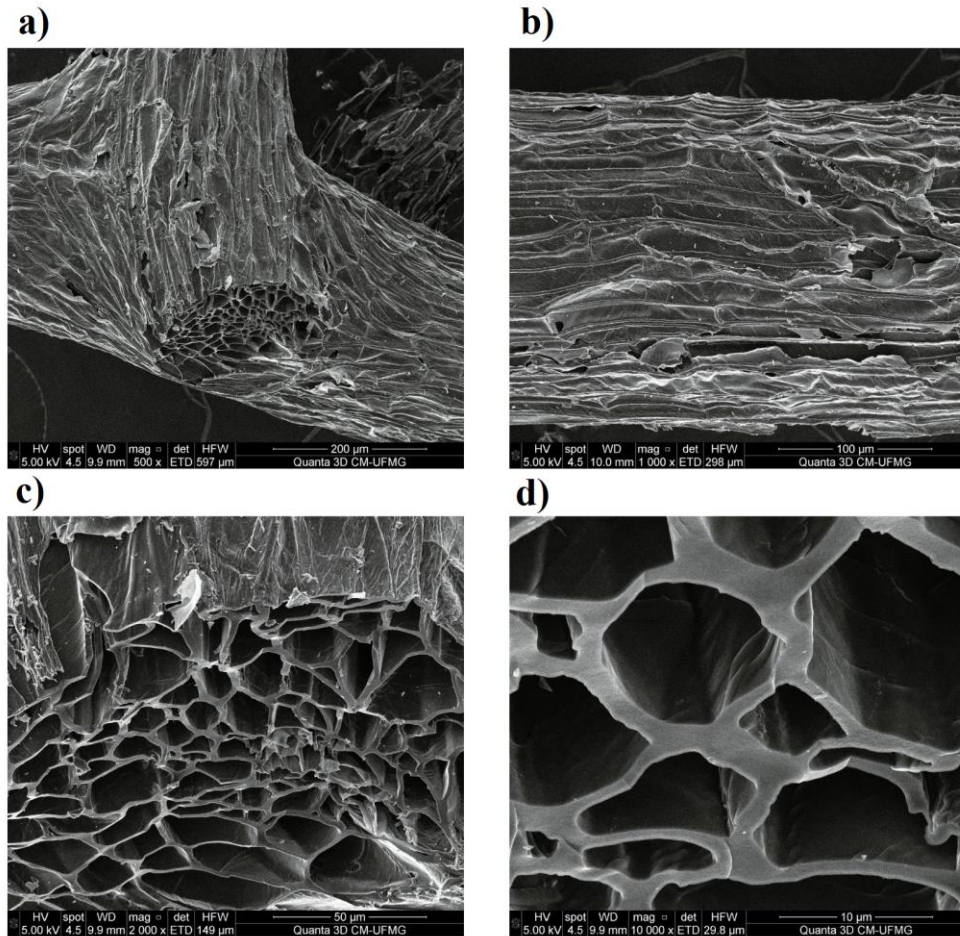


Figure 46– *Luffa cylindrica* biochar (B400-2): **a)** X500; **b)** X1000; **c)** Cross-section (X2000); **d)** Cross-section (X10000).

The morphologic effects caused by pyrolysis are enhanced when the final temperature is increased. Figure 47 compiles SEM micrographs of the B500-2 biochar, the one with the highest mass loss. As can be seen even in a more macroscopic scale in Figure 47-a, the biochar surface is highly deteriorated, with many cracks and pores. Figure 47-b shows this effect with higher magnification. As can be seen in figures 47-c and 47-d, the inner structure of the biochar appears hollower. The tubular pores have perceptively thinner walls. The B500-2 biochar is a material with a high surface to mass ratio, which is a positive property for both adsorption and fuel applications.

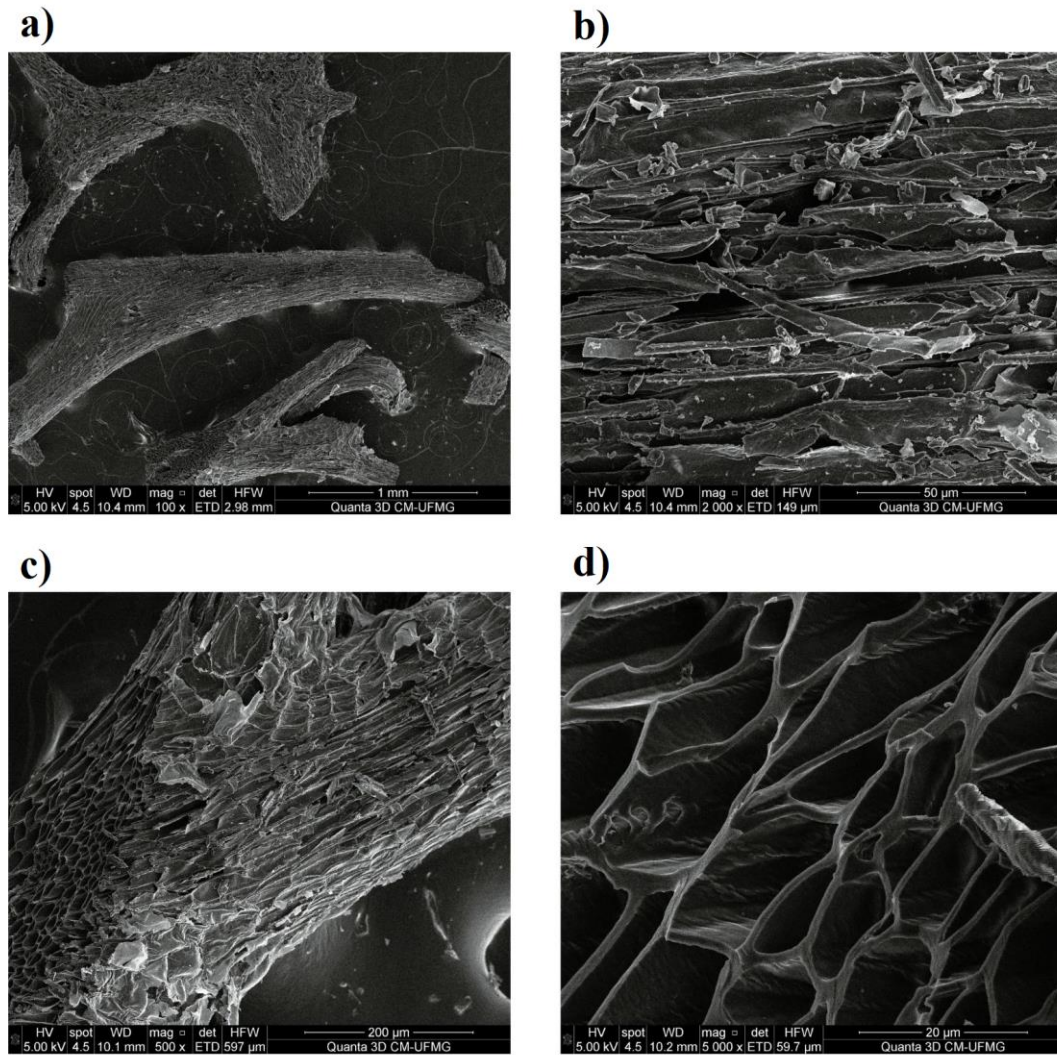


Figure 47 – *Luffa cylindrica* biochar (B500-2): **a)** X100; **b)** X2000; **c)** Cross-section and surface (X500); **d)** Cross-section (X5000).

The last biochar analyzed via SEM is the one obtained through solar pyrolysis. The biochar overall observed morphology (Figure 48) is similar to the one observed for the B400-2, which is sensible since the maximum solar pyrolysis temperature was 417 °C. Cracks and pores, such as the one observed in Figure 48-c, are present on the surface. However, the inner structure of this biochar appears better preserved than that of B400-2, which is also sensible, due to the higher heating rate (lower reaction time) of the solar pyrolysis. The walls of the inner tubular pores come across as being thicker and with a rougher character, which resembles what is observed on the *Luffa cylindrica* cross-section micrograph.

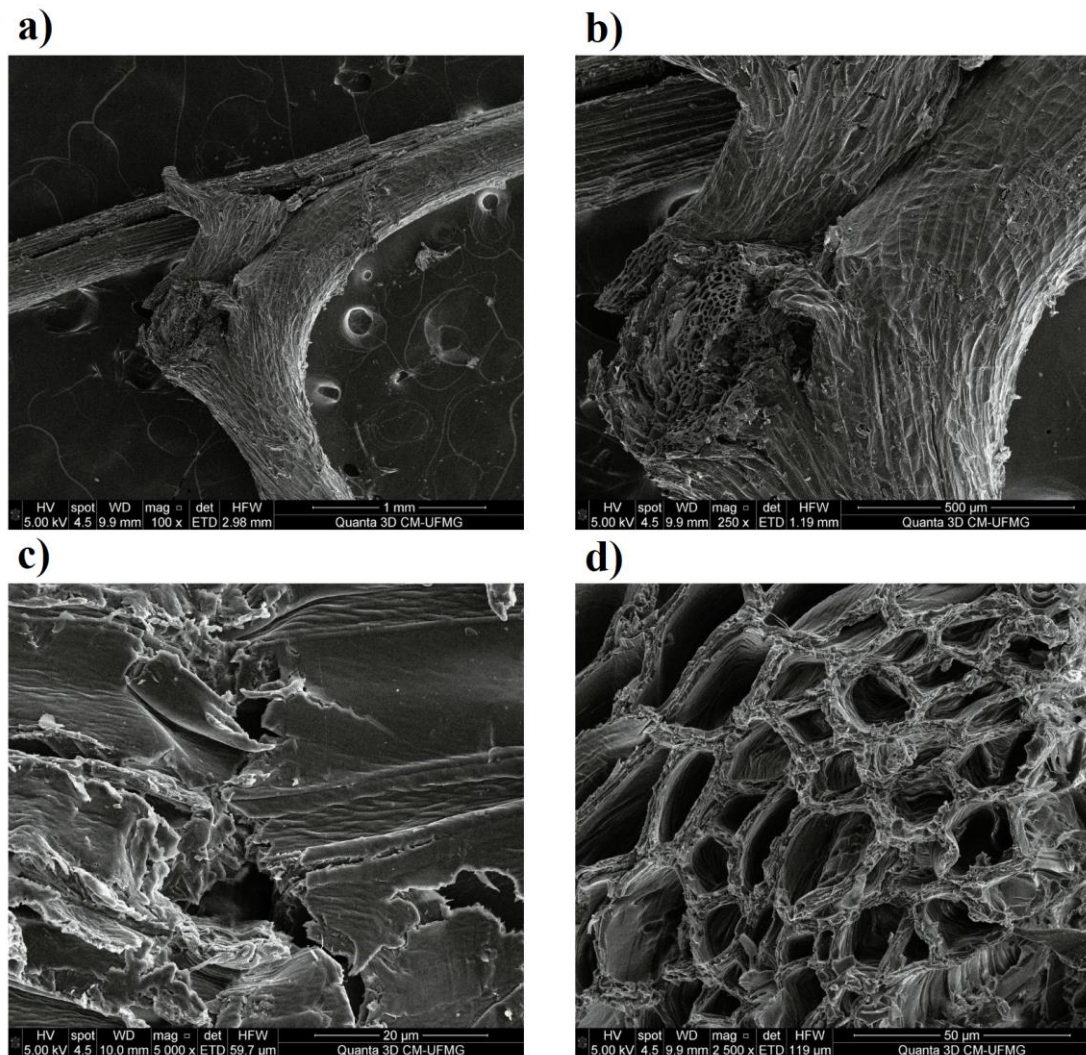


Figure 48 – *Luffa cylindrica* solar biochar: **a)** X500; **b)** X1000; **c)** Cross-section (X2000); **d)** Cross-section (X10000).

4.5 PRELIMINARY IODINE ADSORPTION EXPERIMENTS

ASTM D4607-14 covers the determination of the relative activation level of unused or reactivated carbons by adsorption of iodine from an aqueous solution (ASTM D4607- 94, 1999). It also is a relative indicator of porosity in activated carbon, being used even as an approximation of surface area for some types of activated carbons. As activation processes were not the focus of this study, a simplified version of the ASTM D4607-14 methodology was employed to assess the potential use of *Luffa cylindrica* biochars in adsorption systems with or without later activation. Figure 49 presents the iodine adsorption performance of all produced biochars. The greatest iodine adsorption, 162.9 mg.g⁻¹, was observed on the B400-2 biochar. For comparison, CABOT Norit GAC 1240 commercial activated carbon had an iodine adsorption result of 878 mg.g⁻¹, a result very close to the official reported iodine number of 950 mg.g⁻¹ (CABOT, 2012). These much higher numbers can be explained by the highly optimized activation process which was employed on the commercial char, while *Luffa cylindrica* biochar was tested untreated.

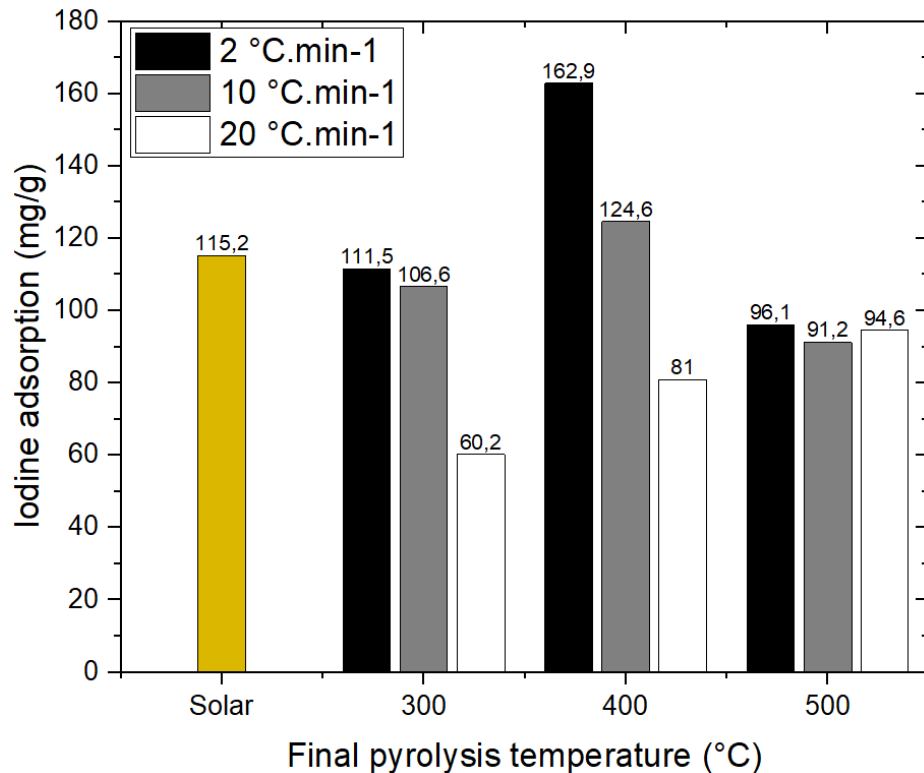


Figure 49 - Iodine adsorption of produced biochars.

A similar trend is observed on the Iodine adsorption of biochars produced in 2 and 10 °C.min⁻¹ pyrolysis. There is an improvement in adsorption performance when the final pyrolysis temperature is increased from 300 to 400 °C, followed by a subsequent decrease when the temperature is raised to 500 °C. Literature supports that surface area in biochars has a positive relationship with pyrolysis temperature in the range of 300 to 500 °C (ANGIN; ŞENSÖZ, 2014; KACAN, 2016), which explains the initial adsorption increase. However, as pyrolysis progresses to higher temperatures, surface functional groups are removed by charring reactions, resulting in a negative impact on adsorption performance.

Another trend observed in iodine adsorption results is the decrease in performance as the pyrolysis heating rate increases. It has been reported in the literature that higher heating rates produce biochars with lower surface areas (ANGIN, 2013; LUA, 2020). While lower heating rates allow for sufficient time for diffusion of volatile pyrolysis products, at higher heating rates, these products accumulate on empty spaces, decreasing porosity. Therefore, biochars produced at 20 °C.min⁻¹ did not develop good porosity, resulting in poor iodine adsorption performance at lower temperatures. B500-20, however, had iodine adsorption equivalent to other B500 biochars. This result indicates that, at this higher temperature, volatiles accumulated on porous medium have been evaporated, increasing biochar porosity and hence iodine adsorption. The solar biochar had the third best iodine adsorption, 115.2 mg.g⁻¹, which shows that it has a good balance between porosity and surface functional groups.

5 CONCLUSIONS

The present work covered a thorough study on the pyrolysis of the *Luffa cylindrica* dry gourd biomass with special emphasis on the production of biochars. The *Luffa cylindrica* gourd biomass was characterized through ultimate analysis, XRF, FTIR, TG/DTG, HHV, and SEM. Characterization methods FTIR, TG/DTG, HHV, and SEM were employed on all produced biochars to tailor the understanding of pyrolysis parameters influence on biochar properties. The Iodine adsorption of biochars was also studied.

Two solar reactors were designed and built, although only one of them could be fully operationalized in time. The parabolic trough solar pyrolyzer has a partial design flaw that makes it unfeasible to be used for pyrolysis purposes in the winter when the solar altitude or elevation is too low. The parabolic dish solar pyrolyzer, which was built on a R\$ 200,00 budget, on the other hand, was a remarkable success, being capable of rapidly reaching pyrolysis temperatures even on suboptimal solar elevations. Temperatures up to 417 °C were reached under a 1-hour long run. The biochar produced on the solar dish pyrolyzer had great HVV and iodine adsorption results, being comparable to the best performing biochars produced on the electric furnace reactor.

It is concluded that the yield of biochar is highly dependent on the final pyrolysis temperature, as well as the heating rate of the process. The higher the temperature, the greater the thermal degradation, and the more volatile components are formed. The higher the heating rate, the shorter the residence time of the biomass in the reactor, which leads to incomplete degradation of the biopolymer structures.

Through the TG/DTG tests, it is concluded that the thermal decompositions of the lignocellulosic biopolymers have different relationships with temperature and heating rate. Hemicelluloses and cellulose have distinct DTG peaks at 280 and 350 °C, respectively, while lignin degradation extends over a broad temperature range from 400 °C onwards. Hemicelluloses degrade easily, so that, their degradation peak is not found in any biochar DTG curve, regardless of the heating rate. Cellulose degradation, on the other hand, is kinetically slower, being highly dependent on the heating rate. The cellulose degradation peak is found even at the DTG curve of the biochar produced at 500 °C, 20 °C.min⁻¹ pyrolysis. Similarly, lignin degradation is a kinetically slow event, being almost complete on 500 °C, 2 °C.min⁻¹ pyrolysis, but hardly started in the pyrolysis at the same temperature but with 20 °C.min⁻¹ heating rate.

Pyrolysis mechanisms of biomass biopolymers described in the literature were confirmed on FTIR results. As pyrolysis temperature increases, fewer functional groups are present on the biochar. As the heating rate increases, more functional groups are still preserved and are detected. Peaks related to some pyrolysis products are observed on FTIR spectra of biochars produced at

mild conditions. As pyrolysis parameters become harsher, these compounds are further degraded or volatilized. This phenomenon was observed in the formation of furanoses from cellulose pyrolysis, phenolic compounds from lignin pyrolysis, and in the formation of carbonyl-containing products from the degradation of all major lignocellulosic biopolymers (cellulose, hemicellulose, and lignin).

The higher heating value of *Luffa cylindrica* biochars rises as pyrolysis temperature increases. The same effect is observed when the heating rate is decreased. A more thorough degradation process results in biochar with greater energy density. The HHV of biochars produced at 500 °C are comparable to the values found for commercial vegetal coal.

Iodine adsorption of biochars presented a different behavior regarding the studied parameters. An initial rise in temperature caused the adsorption to increase due to the growth in surface area (porosity). Further temperature increase caused the functional groups due to charring reactions, causing the adsorption to decrease. Therefore, intermediate temperatures resulted in the best adsorptive performance. Increasing heating rate caused this effect to become less pronounced since charring and porosity increase are postponed to higher temperatures in faster heating circumstances. Therefore, the biochar with the best adsorptive capacity was the one produced at the intermediate temperature (400 °C) and slower heating rate (2 °C.min⁻¹).

Scanning Electron micrographs of *Luffa cylindrica* and selected biochars support conclusions made over iodine adsorption results regarding the increase of surface area by pyrolysis temperature increase and heating rate decrease. The *Luffa cylindrica* fiber was found to be a compact material of rough surface with low porosity. As pyrolysis progresses, biochar surface cracks and becomes porous, while tubular pores develop in the inner structure of the material.

Pyrolysis once again is demonstrated to be a great methodology for the production of valuable products from biomass. Produced biochars show potential to be used in adsorption systems, such as those implemented for pollutants removal. Their high HHV indicate that energy

retrieval by incineration could be a good alternative for their life cycle termination. Finally, the promising use of solar irradiance as an energy source was proven to be feasible even under low financial investment.

6 FUTURE WORK SUGGESTIONS

As suggestions for future work, it is proposed:

- To study *Luffa cylindrica* pyrolysis with emphasis on liquid and gaseous products;
- To study *Luffa cylindrica* pyrolysis under different atmospheres like carbon dioxide, water vapor, and vacuum.
- To study the solar pyrolysis of *Luffa cylindrica* and other biomasses with emphasis on process parameters like exposure time and seasonal variability.
- To perform activation processes to enhance adsorption performance of *Luffa cylindrica* biochar;
- To design an improved parabolic trough solar collector to enable continuous processes;
- To design and operationalize an automation system capable of following the sun path in the sky.

REFERENCES

- ABDELWAHAB, O.; AMIN, N. K. Adsorption of phenol from aqueous solutions by *Luffa cylindrica* fibers: Kinetics, isotherm and thermodynamic studies. **Egyptian Journal of Aquatic Research**, v. 39, n. 4, p. 215–223, 2013.
- AHMAD, M. et al. Biochar as a sorbent for contaminant management in soil and water: A review. **Chemosphere**, v. 99, p. 19–33, 2014.
- AKHTAR, J.; SAIDINA AMIN, N. A review on operating parameters for optimum liquid oil yield in biomass pyrolysis. **Renewable and Sustainable Energy Reviews**, v. 16, n. 7, p. 5101–5109, 2012.
- ALTINIŞIK, A.; GÜR, E.; SEKI, Y. A natural sorbent, *Luffa cylindrica* for the removal of a model basic dye. **Journal of Hazardous Materials**, v. 179, n. 1–3, p. 658–664, 2010.
- ANASTOPOULOS, I.; PASHALIDIS, I. The application of oxidized carbon derived from *Luffa cylindrica* for caffeine removal. Equilibrium, thermodynamic, kinetic and mechanistic analysis. **Journal of Molecular Liquids**, v. 296, n. xxxx, p. 112078, 2019.
- ANGIN, D. Effect of pyrolysis temperature and heating rate on biochar obtained from pyrolysis of safflower seed press cake. **Bioresource Technology**, v. 128, p. 593–597, 2013.
- ANGIN, D.; ŞENSÖZ, S. Effect of Pyrolysis Temperature on Chemical and Surface Properties of Biochar of Rapeseed (*Brassica napus* L.). **International Journal of Phytoremediation**, v. 16, n. 7–8, p. 684–693, 2014.
- ARCHER, C. L.; JACOBSON, M. Z. Evaluation of global wind power. **Journal of Geophysical Research D: Atmospheres**, v. 110, n. 12, p. 1–20, 2005.
- ASMADI, M.; KAWAMOTO, H.; SAKA, S. Gas- and solid/liquid-phase reactions during pyrolysis of softwood and hardwood lignins. **Journal of Analytical and Applied Pyrolysis**, v. 92, n. 2, p. 417–425, 2011.
- ASTM D4607- 94. Standard Test Method for Determination of Iodine Number of Activated Carbon. **Astm International**, v. 94, n. Reapproved, p. 1–5, 1999.
- BASTOS, P. C. et al. TRATAMENTOS INTERFACIAIS DO ADSORVENTE LUFFA CYLINDRICA PARA REMOÇÃO DE ÉTER-AMINAS DE EFLUENTES. XXVII Encontro Nacional de Tratamento de Minérios e Metalurgia Extrativa. **Anais...**Belém-PA: 2017

BASTOS, P. C. **Caracterização do bioissorvente Luffa Cylindrica in natura e funcionalizado e seu uso na remoção de eteraminas de soluções aquosas.** [s.l.] UFMG, 2018.

BOYNARD, C. A.; D'ALMEIDA, J. R. M. Morphological characterization and mechanical behavior of sponge gourd (*Luffa cylindrica*)-polyester composite materials. **Polymer - Plastics Technology and Engineering**, v. 39, n. 3, p. 489–499, 2000.

BREBU, M.; VASILE, C. Thermal degradation of lignin - A review. **Cellulose Chemistry and Technology**, v. 44, n. 9, p. 353–363, 2010.

BRIDGWATER, A. V. Review of fast pyrolysis of biomass and product upgrading. **Biomass and Bioenergy**, v. 38, p. 68–94, 2011.

CABOT, W. H. Y. Norit ® GAC 1240 W. n. January, p. 2012–2013, 2012.

CASIO COMPUTER, C. L. **Solar elevation angle (for a day) Calculator.** Disponível em: <<https://keisan.casio.com/exec/system/1224682277>>. Acesso em: 13 ago. 2021.

CHEN, D. et al. Pyrolysis polygeneration of poplar wood: Effect of heating rate and pyrolysis temperature. **Bioresource Technology**, v. 218, p. 780–788, 2016.

CHEN, X. G. et al. Adsorption of Methylene Blue by Rice Hull Ash. **Separation Science and Technology**, v. 47, n. 1, p. 147–156, 2012.

DE PAULA PROTÁSIO, T. et al. Charcoal productivity and quality parameters for reliable classification of Eucalyptus clones from Brazilian energy forests. **Renewable Energy**, v. 164, p. 34–45, 2021.

DEMIRBAS, A. Effect of temperature on pyrolysis products from four nut shells. **Journal of Analytical and Applied Pyrolysis**, v. 76, n. 1–2, p. 285–289, 2006.

DEMIRBAŞ, A. Relationships between lignin contents and heating values of biomass. **Energy Conversion and Management**, v. 42, n. 2, p. 183–188, 2001.

DHYANI, V.; BHASKAR, T. A comprehensive review on the pyrolysis of lignocellulosic biomass. **Renewable Energy**, v. 129, p. 695–716, 2018.

DI BLASI, C.; BRANCA, C.; GALGANO, A. Biomass screening for the production of furfural via thermal decomposition. **Industrial and Engineering Chemistry Research**, v. 49, n. 6, p. 2658–2671, 2010.

DO NASCIMENTO, L. R. et al. Extreme solar overirradiance events: Occurrence and impacts on utility-scale photovoltaic power plants in Brazil. **Solar Energy**, v. 186, n. May, p. 370–381,

2019.

DREYER, I.; UOZUMI, N. Potassium channels in plant cells. **FEBS Journal**, v. 278, n. 22, p. 4293–4303, 2011.

E. PEREIRRA ET AL. Atlas brasileiro de energia solar (Vol. 1). p. 80, 2006.

FAHMY, T. Y. A. et al. Biomass pyrolysis: past, present, and future. **Environment, Development and Sustainability**, v. 22, n. 1, p. 17–32, 2020.

FEARON, E. P. et al. Thermal effects of substrate materials used in the laser curing of particulate silver inks Laser Cleaning of Precious Metals View project Laser-Assisted direct write (laser sintering) View project. n. February 2014, p. 379–390, 2007.

FENG, Y. et al. Norfloxacin removal from aqueous solution using biochar derived from luffa sponge. **Journal of Water Supply: Research and Technology - AQUA**, v. 67, n. 8, p. 703–714, 2018.

FERNÁNDEZ-GARCÍA, A. et al. Parabolic-trough solar collectors and their applications. **Renewable and Sustainable Energy Reviews**, v. 14, n. 7, p. 1695–1721, 2010.

FOLEY, R. T. Localized corrosion of aluminum alloys—a review. **Corrosion**, v. 42, n. 5, p. 277–288, 1986.

FORTELAB - Industria de Fornos Elétricos LTDA - Forno FT - 1200H/V. Disponível em: <<https://www.fortelab.com.br/index.php/produtos/fornos-de-pesquisa-e-desenvolvimento-para-laboratorio/fornos-tubulares-ate-1300-c/forno-ft-1200h-v>>. Acesso em: 3 fev. 2021.

GARCIA-NUNEZ, J. A. et al. Historical Developments of Pyrolysis Reactors: A Review. **Energy and Fuels**, v. 31, n. 6, p. 5751–5775, 2017.

GEDAM, A. H.; DONGRE, R. S. Activated carbon from *Luffa cylindrica* doped chitosan for mitigation of lead(ii) from an aqueous solution. **RSC Advances**, v. 6, n. 27, p. 22639–22652, 2016.

GÍRIO, F. M. et al. Hemicelluloses for fuel ethanol: A review. **Bioresource Technology**, v. 101, n. 13, p. 4775–4800, 2010.

Global Waste Management Outlook. [s.l: s.n.].

GOOD, P. et al. Spectral reflectance, transmittance, and angular scattering of materials for solar concentrators. **Solar Energy Materials and Solar Cells**, v. 144, p. 509–522, 2016.

GUEDES, R. E.; LUNA, A. S.; TORRES, A. R. Operating parameters for bio-oil production in

biomass pyrolysis: A review. **Journal of Analytical and Applied Pyrolysis**, v. 129, p. 134–149, 2018.

GUIZANI, C.; ESCUDERO SANZ, F. J.; SALVADOR, S. Effects of CO₂ on biomass fast pyrolysis: Reaction rate, gas yields and char reactive properties. **Fuel**, v. 116, n. August, p. 310–320, 2014.

GUO, W. et al. Magnesium deficiency in plants: An urgent problem. **Crop Journal**, v. 4, n. 2, p. 83–91, 2016.

GUPTA, V. K. et al. **Amputation of congo red dye from waste water using microwave induced grafted Luffa cylindrica cellulosic fiber**. [s.l.] Elsevier Ltd., 2014. v. 111

HASANUZZAMAN, M. et al. Plant nutrients and abiotic stress tolerance. **Plant Nutrients and Abiotic Stress Tolerance**, n. June, p. 1–590, 2018.

HEIDARI, A. et al. Evaluation of fast and slow pyrolysis methods for bio-oil and activated carbon production from eucalyptus wastes using a life cycle assessment approach. **Journal of Cleaner Production**, v. 241, p. 118394, 2019.

HENINI, G. et al. Study of static adsorption system phenol / Luffa cylindrica fiber for industrial treatment of wastewater. **Energy Procedia**, v. 18, p. 395–403, 2012.

HUANG, Y. F.; LO, S. L. Predicting heating value of lignocellulosic biomass based on elemental analysis. **Energy**, v. 191, n. xxxx, p. 116501, 2020.

INCROPERA, F. P.; BERGMAN, T.; LAVINE, A. **Incropera: Fundamentos de Transferência de Calor e de Massa**. 6th editio ed. Rio de Janeiro: LTC, 2008.

JOARDDER, M. U. H. et al. Energy, Solar pyrolysis: converting waste into asset using solar. In: **Clean Energy for Sustainable Development**. [s.l.] Elsevier, 2017. p. 632.

KACAN, E. Optimum BET surface areas for activated carbon produced from textile sewage sludges and its application as dye removal. **Journal of Environmental Management**, v. 166, p. 116–123, 2016.

KAN, T.; STREZOV, V.; EVANS, T. J. Lignocellulosic biomass pyrolysis: A review of product properties and effects of pyrolysis parameters. **Renewable and Sustainable Energy Reviews**, v. 57, p. 1126–1140, 2016.

KAWAMOTO, H. Lignin pyrolysis reactions. **Journal of Wood Science**, v. 63, n. 2, p. 117–132, 2017.

KAYHAN, Ö. A thermal model to investigate the power output of solar array for stratospheric balloons in real environment. **Applied Thermal Engineering**, v. 139, n. March, p. 113–120, 2018.

KAZA, S. et al. **WHAT A WASTE 2.0: A Global Snapshot of Solid Waste Management to 2050**. [s.l.: s.n.].

KHANDELWAL, M.; WINDLE, A. H. Hierarchical organisation in the most abundant biopolymer-cellulose. **Materials Research Society Symposium Proceedings**, v. 1504, p. 16–21, 2013.

KODAMA, T. **High-temperature solar chemistry for converting solar heat to chemical fuels**. [s.l.: s.n.]. v. 29

KUMAR GUPTA, P. et al. An Update on Overview of Cellulose, Its Structure and Applications. **Cellulose**, n. May, 2019.

LAIDANI, Y. et al. Study of a Fibrous Annual Plant, Luffa Cylindrica for Ppaper Application Part I: Characterization of theVegetal. **Iranian Journal Of Chemistry And Chemical Engineering**, v. 31, n. 4, p. 119–129, 2012.

LEISOLA, M.; PASTINEN, O.; AXE, D. D. Lignin--Designed Randomness. **BIO-Complexity**, v. 2012, n. 3, p. 1–11, 2012.

LI, H. et al. Carbon-Increasing Catalytic Strategies for Upgrading Biomass into Energy-Intensive Fuels and Chemicals. **ACS Catalysis**, v. 8, n. 1, p. 148–187, 2018.

LIATSOU, I. et al. Surface characterization of oxidized biochar fibers derived from Luffa Cylindrica and lanthanide binding. **Journal of Environmental Chemical Engineering**, v. 5, n. 4, p. 4069–4074, 2017a.

LIATSOU, I. et al. Uranium binding by biochar fibres derived from Luffa cylindrica after controlled surface oxidation. **Journal of Radioanalytical and Nuclear Chemistry**, v. 311, n. 1, p. 871–875, 2017b.

LIATSOU, I.; CHRISTODOULOU, E.; PASHALIDIS, I. Thorium adsorption by oxidized biochar fibres derived from Luffa cylindrica sponges. **Journal of Radioanalytical and Nuclear Chemistry**, v. 317, n. 2, p. 1065–1070, 2018.

LIATSOU, I.; CONSTANTINOU, P.; PASHALIDIS, I. Copper Binding by Activated Biochar Fibres Derived from Luffa cylindrica. **Water, Air, and Soil Pollution**, v. 228, n. 7, 2017.

- LIN, Y. et al. Kinetics and Mechanism of Cellulose Pyrolysis. **Journal of Physical Chemistry**, p. 20097–20107, 2009.
- LINDINO, C. et al. A tecnologia de remoção de fósforo: Gerenciamento do elemento em resíduos industriais. **Revista Ambiente e Agua**, v. 9, n. 3, p. 445–458, 2014.
- LUA, A. C. A detailed study of pyrolysis conditions on the production of steam-activated carbon derived from oil-palm shell and its application in phenol adsorption. **Biomass Conversion and Biorefinery**, v. 10, n. 2, p. 523–533, 2020.
- MA, J. F. Plant root responses to three abundant soil minerals: Silicon, aluminum and iron. **Critical Reviews in Plant Sciences**, v. 24, n. 4, p. 267–281, 2005.
- MANYÀ, J. J. et al. Experimental study on the effect of pyrolysis pressure, peak temperature, and particle size on the potential stability of vine shoots-derived biochar. **Fuel**, v. 133, p. 163–172, 2014.
- MOHAN, D.; PITTMAN, C. U.; PHILIP, S. Pyrolysis of Wood/Biomass for Bio-oil: A Critical Review Dinesh. **Progress in Energy and Combustion Science**, v. 62, n. 4, p. 848–889, 2017.
- NAGARAJAGANESH, B.; MURALIKANNAN, R. Extraction and characterization of lignocellulosic fibers from *Luffa cylindrica* fruit. **International Journal of Polymer Analysis and Characterization**, v. 21, n. 3, p. 259–266, 2016.
- NAKAMURA, T.; KAWAMOTO, H.; SAKA, S. Pyrolysis behavior of Japanese cedar wood lignin studied with various model dimers. **Journal of Analytical and Applied Pyrolysis**, v. 81, n. 2, p. 173–182, 2008.
- NOBLES, D. R.; ROMANOVICZ, D. K.; BROWN, J. Cellulose in cyanobacteria. Origin of vascular plant cellulose synthase? **Plant Physiology**, v. 127, n. 2, p. 529–542, 2001.
- NZIHOU, A. et al. The catalytic effect of inherent and adsorbed metals on the fast/flash pyrolysis of biomass: A review. **Energy**, v. 170, p. 326–337, 2019.
- OBOH, I. O.; ALUYOR, E. O. *Luffa cylindrica* - an emerging cash crop. **African Journal of Agricultural Research**, v. 4, n. 8, p. 684–688, 2009.
- PAGLICAWAN, M. A. et al. Loofah Fiber as Reinforcement Material for Composite. v. 134, n. December, p. 113–120, 2005.
- PARK, H. J.; PARK, Y. K.; KIM, J. S. Influence of reaction conditions and the char separation system on the production of bio-oil from radiata pine sawdust by fast pyrolysis. **Fuel Processing**

Technology, v. 89, n. 8, p. 797–802, 2008.

PARTAP, S. et al. Luffa Cylindrica : An important medicinal plant. **J. Nat. Prod. Plant Resour**, v. 2, n. 1, p. 127–134, 2012.

PENG, F. et al. Fractional purification and bioconversion of hemicelluloses. **Biotechnology Advances**, v. 30, n. 4, p. 879–903, 2012.

PEREIRA, P. H. F. et al. Vegetal fibers in polymeric composites: A review. **Polimeros**, v. 25, n. 1, p. 9–22, 2015.

PITZ-PAAL, R.; BOTERO, N. B.; STEINFELD, A. Heliostat field layout optimization for high-temperature solar thermochemical processing. **Solar Energy**, v. 85, n. 2, p. 334–343, 2011.

PONNUSAMY, V. K. et al. A review on lignin structure, pretreatments, fermentation reactions and biorefinery potential. **Bioresource Technology**, v. 271, p. 462–472, 2019.

PREMALATHA, N. et al. Structural and Thermal Properties of Chemically Modified Luffa Cylindrica Fibers. **Journal of Natural Fibers**, v. 00, n. 00, p. 1–7, 2019.

QIAN, C. et al. Prediction of higher heating values of biochar from proximate and ultimate analysis. **Fuel**, v. 265, n. December 2019, p. 116925, 2020.

QU, T. et al. Experimental Study of Biomass Pyrolysis Based on Three Major Components: Hemicellulose, Cellulose, and Lignin. **Energy Conversion and Management**, v. 50, n. 18, p. 10424–10433, 2011.

RABEMANOLONTSOA, H.; SAKA, S. Comparative study on chemical composition of various biomass species. **RSC Advances**, v. 3, n. 12, p. 3946–3956, 2013.

RALPH, J.; LAPIERRE, C.; BOERJAN, W. Lignin structure and its engineering. **Current Opinion in Biotechnology**, v. 56, p. 240–249, 2019.

ROUT, G. R.; SAHOO, S. Role of Iron in Plant Growth and Metabolism. **Reviews in Agricultural Science**, v. 3, n. 0, p. 1–24, 2015.

SADEGH, H. et al. Nanomaterial surface modifications for enhancement of the pollutant adsorption from wastewater: Adsorption of nanomaterials. **Nanotechnology Applications in Environmental Engineering**, n. July, p. 143–170, 2019.

SAFDARI, M. S. et al. Heating rate and temperature effects on pyrolysis products from live wildland fuels. **Fuel**, v. 242, n. October 2018, p. 295–304, 2019.

SAHIN, A. Z.; KALYON, M. The critical radius of insulation in thermal radiation environment.

Heat and Mass Transfer/Waerme- und Stoffuebertragung, v. 40, n. 5, p. 377–382, 2004.

SATYANARAYANA, K. G.; GUIMARÃES, J. L.; WYPYCH, F. Studies on lignocellulosic fibers of Brazil. Part I: Source, production, morphology, properties and applications. **Composites Part A: Applied Science and Manufacturing**, v. 38, n. 7, p. 1694–1709, 2007.

SAXE, J. P. et al. Just or bust? Energy justice and the impacts of siting solar pyrolysis biochar production facilities. **Energy Research and Social Science**, v. 58, n. September 2018, p. 101259, 2019.

SEKI, Y. et al. Characterization of *Luffa cylindrica* Fibers and the Effect of Water Aging on the Mechanical Properties of Its Composite with Polyester. **Journal of Applied Polymer Science**, v. 123, p. 2330–2337, 2011.

SHAHIDI, A.; JALILNEJAD, N.; JALILNEJAD, E. A study on adsorption of cadmium(II) ions from aqueous solution using *Luffa cylindrica*. **Desalination and Water Treatment**, v. 53, n. 13, p. 3570–3579, 2015.

SHELDON, R. A. Green and sustainable manufacture of chemicals from biomass: State of the art. **Green Chemistry**, v. 16, n. 3, p. 950–963, 2014.

SHEN, D. K. et al. The pyrolytic degradation of wood-derived lignin from pulping process. **Bioresource Technology**, v. 101, n. 15, p. 6136–6146, 2010a.

SHEN, D. K.; GU, S.; BRIDGWATER, A. V. Study on the pyrolytic behaviour of xylan-based hemicellulose using TG-FTIR and Py-GC-FTIR. **Journal of Analytical and Applied Pyrolysis**, v. 87, n. 2, p. 199–206, 2010.

SHEN, J. et al. The prediction of elemental composition of biomass based on proximate analysis. **Energy Conversion and Management**, v. 51, n. 5, p. 983–987, 2010b.

SHEN, J. et al. Mechanical properties of luffa sponge. **Journal of the Mechanical Behavior of Biomedical Materials**, v. 15, p. 141–152, 2012.

SHYLES, S. et al. Novel Strategies for the Production of Fuels, Lubricants, and Chemicals from Biomass. **Accounts of Chemical Research**, v. 50, n. 10, p. 2589–2597, 2017.

SILVA, M. W. K. P.; RANIL, R. H. G.; FONSEKA, R. M. *Luffa cylindrica* (L.) M. Roemer (Sponge Gourd-Niyam wetakolu): An Emerging High Potential Underutilized Cucurbit. **Tropical Agricultural Research**, v. 24, n. 2, p. 186, 2015.

SIQUEIRA, G. et al. Thermal and mechanical properties of bio-nanocomposites reinforced by

Luffa cylindrica cellulose nanocrystals. **Carbohydrate Polymers**, v. 91, n. 2, p. 711–717, 2013.

STEFANIDIS, S. D. et al. A study of lignocellulosic biomass pyrolysis via the pyrolysis of cellulose, hemicellulose and lignin. **Journal of Analytical and Applied Pyrolysis**, v. 105, p. 143–150, 2014.

SUBBARAO, G. V. et al. Sodium - A Functional Plant Nutrient. **Critical Reviews in Plant Sciences**, v. 22, n. 5, p. 391–416, 2003.

SURIAPPARAO, D. V.; VINU, R. Effects of Biomass Particle Size on Slow Pyrolysis Kinetics and Fast Pyrolysis Product Distribution. **Waste and Biomass Valorization**, v. 9, n. 3, p. 465–477, 2018.

TAHERZADEH, M. J. et al. Characterization and Fermentation of Dilute-Acid Hydrolyzates from Wood. **Industrial and Engineering Chemistry Research**, v. 36, n. 11, p. 4659–4665, 1997.

TANOBE, V. O. A. et al. A comprehensive characterization of chemically treated Brazilian sponge-gourds (*Luffa cylindrica*). **Polymer Testing**, v. 24, n. 4, p. 474–482, 2005.

TÓTH, A. et al. ESCA (XPS) study on light-induced yellowing of thermomechanical and chemothermomechanical pulps. **Applied Surface Science**, v. 72, n. 3, p. 209–213, 1993.

TRIPATHI, M.; SAHU, J. N.; GANESAN, P. Effect of process parameters on production of biochar from biomass waste through pyrolysis: A review. **Renewable and Sustainable Energy Reviews**, v. 55, p. 467–481, 2016.

URAS, Ü. et al. Physico-chemical characterization of biochars from vacuum pyrolysis of South African agricultural wastes for application as soil amendments. **Journal of Analytical and Applied Pyrolysis**, v. 98, p. 207–213, 2012.

VORWERK, S.; SOMERVILLE, S.; SOMERVILLE, C. The role of plant cell wall polysaccharide composition in disease resistance. **Trends in Plant Science**, v. 9, n. 4, p. 203–209, 2004.

WANG, S. et al. Lignocellulosic biomass pyrolysis mechanism: A state-of-the-art review. **Progress in Energy and Combustion Science**, v. 62, p. 33–86, 2017.

WANG, S.; LUO, Z. **Pyrolysis of biomass**. [s.l.] De Gruyter, 2016.

WELDEKIDAN, H. et al. Waste to Energy Conversion of Chicken Litter through a Solar-Driven Pyrolysis Process. **Energy and Fuels**, v. 32, n. 4, p. 4341–4349, 2018.

WHITE, P. J.; BROADLEY, M. R. Calcium in plants. **Annals of Botany**, v. 92, n. 4, p. 487–511, 2003.

WU, S. et al. Role of β -O-4 glycosidic bond on thermal degradation of cellulose. **Journal of Analytical and Applied Pyrolysis**, v. 119, p. 147–156, 2016.

XU, F. et al. Qualitative and quantitative analysis of lignocellulosic biomass using infrared techniques: A mini-review. **Applied Energy**, v. 104, p. 801–809, 2013.

YANG, H. et al. Characteristics of hemicellulose, cellulose and lignin pyrolysis. **Fuel**, v. 86, n. 12–13, p. 1781–1788, 2007.

YE, C.; HU, N.; WANG, Z. Experimental investigation of *Luffa cylindrica* as a natural sorbent material for the removal of a cationic surfactant. **Journal of the Taiwan Institute of Chemical Engineers**, v. 44, n. 1, p. 74–80, 2013.

YRUELA, I. Copper in plants. **Brazilian Journal of Plant Physiology**, v. 17, n. 1, p. 145–156, 2005.

YU, J. et al. Influence of temperature and particle size on structural characteristics of chars from Beechwood pyrolysis. **Journal of Analytical and Applied Pyrolysis**, v. 130, n. December 2017, p. 249–255, 2018.

ZDARTA, J.; JESIONOWSKI, T. *Luffa cylindrica* Sponges as a Thermally and Chemically Stable Support for *Aspergillus niger* Lipase. p. 657–665, 2016a.

ZDARTA, J.; JESIONOWSKI, T. *Luffa cylindrica* sponges as a thermally and chemically stable support for *Aspergillus niger* lipase. **Biotechnology progress**, v. 32, n. 3, p. 657–665, 2016b.

ZENG, K. et al. Solar pyrolysis of carbonaceous feedstocks: A review. **Solar Energy**, v. 156, p. 73–92, 2017.

ZHANG, H. et al. Biomass fast pyrolysis in a fluidized bed reactor under N₂, CO₂, CO, CH₄ and H₂ atmospheres. **Bioresource Technology**, v. 102, n. 5, p. 4258–4264, 2011.

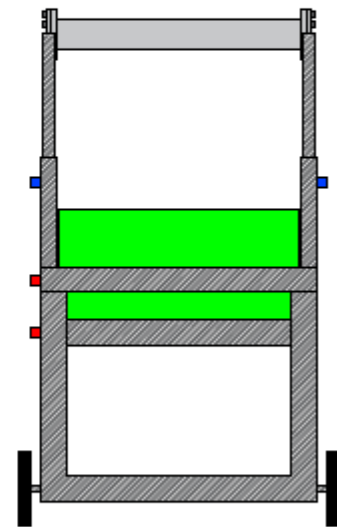
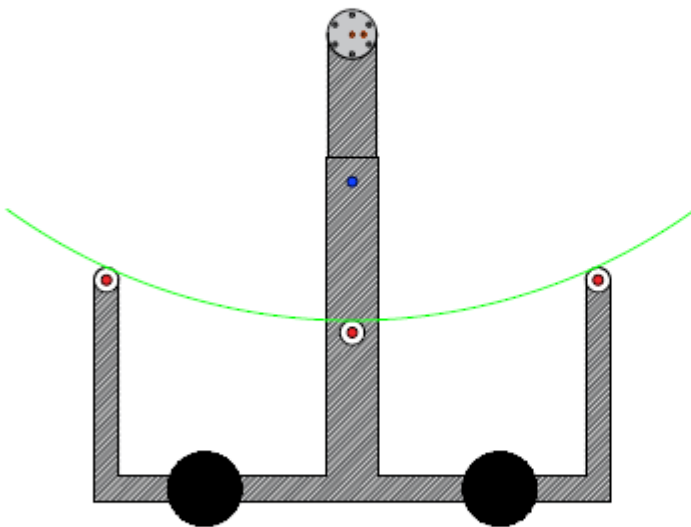
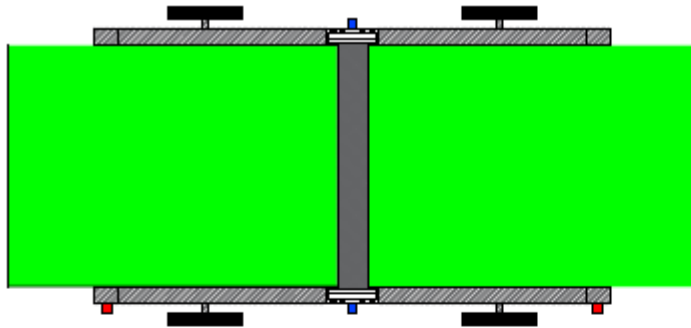
ZHANG, H. L. et al. Concentrated solar power plants: Review and design methodology. **Renewable and Sustainable Energy Reviews**, v. 22, p. 466–481, 2013.









ZHANG, Y. H. et al. Thermal destruction of *luffa* sponge under air and nitrogen. **Journal of Thermal Analysis and Calorimetry**, v. 128, n. 1, p. 53–60, 2017.

ZHU, G. Development of an analytical optical method for linear fresnel collectors. **Solar Energy**, v. 94, p. 240–252, 2013.

ZHU, G. et al. History, current state, and future of linear Fresnel concentrating solar collectors. **Solar Energy**, v. 103, p. 639–652, 2014.

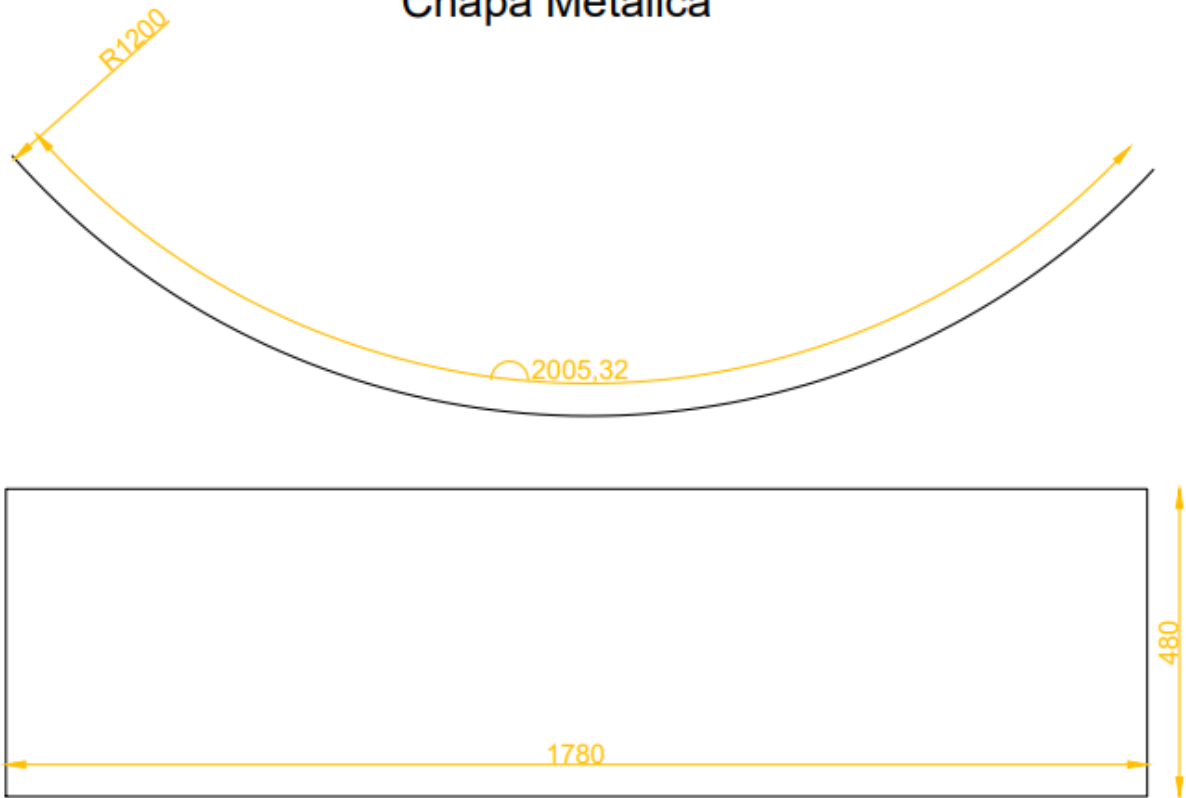
APPENDIX A – PARABOLIC TROUGH SOLAR PYROLYZER DESIGN



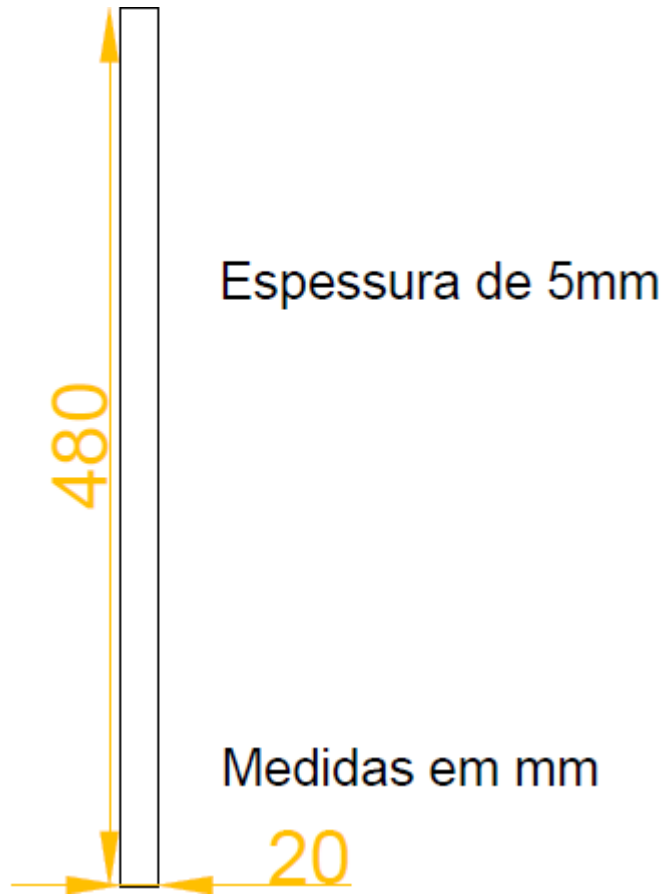
- | | | |
|---|---|--|
|  Aço carbono |  Regulador de altura |  Roscas 1/8 em aço 316l |
|  Aço 316l |  Dispositivo p/ travar o rolamento |  Conexões 1/8 |
|  Espelho |  Rolamento emborrachado | |

APPENDIX B - CURVED CARBON STEEL SHEET

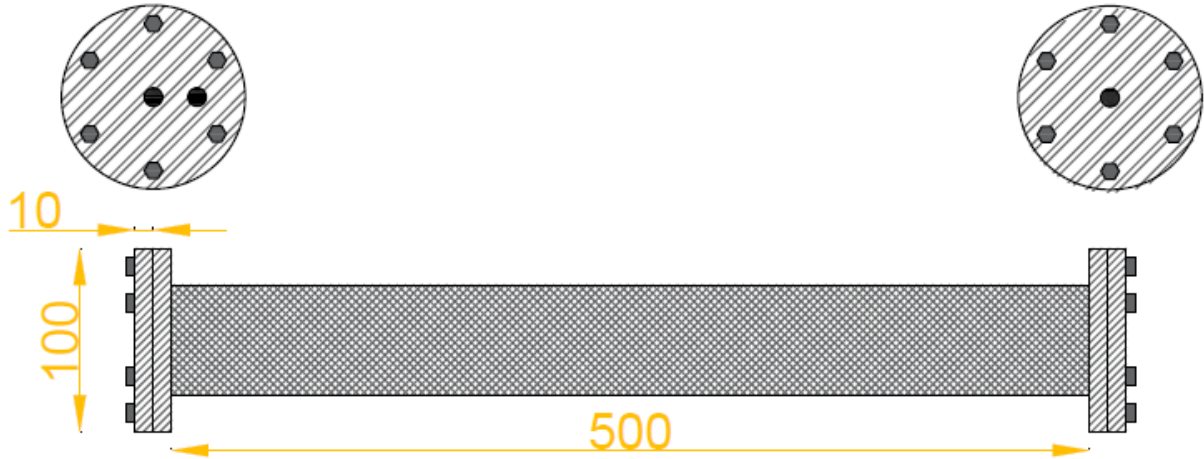
Chapa Metálica




APPENDIX C - MIRROR STRIP





APPENDIX D - CYLINDRICAL STAINLESS-STEEL REACTOR




 Tubo cilíndrico 2" SCH 80s em Aço 316l

Escala em mm

 Flanges em aço 316l

 Roscas 1/8" em aço 316l

 Conexões 1/8"

APPENDIX E – PARABOLIC TROUGH REACTOR CONVECTIVE COEFFICIENTS

Thermophysical properties of air at atmospheric pressure were obtained from Incropera et al. (2008)(INCROPERA; BERGMAN; LAVINE, 2008). The velocity of the airflow considered in the calculations was the global average wind velocity over land, 3.28 m/s(ARCHER; JACOBSON, 2005).

Exposed cylinder convective coefficient

From data obtained from Incropera et al. (2008):

$$Pr = 0.707$$

$$Pr_s = 0.720$$

$$Re_d = \frac{\rho * v * d}{\mu} = (1.1614 \text{ kg/m}^3) * (3.28 \text{ m/s}) * (0.073 \text{ m}) / (184.6 * 10^{-7} \text{ N.s/m}^2)$$

$$Re_d = 1.056 * 10^4$$

Where Pr is the Prandtl number of air at 300 K; Pr_s the Prandtl number for the surface temperature (900 K, in this case); Re_d the Reynolds number for the reactor diameter; ρ the density of air at 300 K; v the wind velocity; d the diameter of the reactor; μ the viscosity of air at 300 K.

Considering the Zukauskas correlation below:

$$Nu_d = \frac{h * d}{k} = C * Re_d^m * Pr^n * \left(\frac{Pr}{Pr_s}\right)^{0.25}$$

Where Nu_d the Nusselt number for the reactor diameter (d); h is the convective coefficient; k is the thermal conductivity; C , m , and n are constants that depend on Reynolds and Prandtl numbers.

For Reynolds numbers between 1000 and 200000, values of C and m are respectively 0.26 and 0.6. For Pr numbers lower than 10, 0.37 is the corresponding value of n . Thus, following Zukauskas's correlation, the convective coefficient of the exposed area can then be calculated.

$$\frac{h * 0.073 \text{ m}}{0.0263 \text{ W}/(\text{m} * \text{K})} = 0.26 * 10560^{0.6} * 0.707^{0.37} * \left(\frac{0.707}{0.720}\right)^{0.25}$$

$$h = 26.3 \text{ W}/(\text{m} * \text{K})$$

The final surface temperature is taken as 900 K and the convective coefficient as 26.3 W/(m²*K) for the insulated lids.

Insulated cylinder convective coefficient and surface temperature

$$Pr = 0.707$$

$$Pr_s = ?$$

$$Re_d = \frac{\rho * v * D}{\mu} = (1.1614 \text{ kg}/\text{m}^3) * (3.28 \text{ m}/\text{s}) * (0.173 \text{ m}) / (184.6 * 10^{-7} \text{ N} \cdot \text{s}/\text{m}^2)$$

$$Re_d = 3.57 * 10^4$$

Where Pr is the Prandtl number of air at 300 K; Pr_s the Prandtl number for the surface temperature (unknown, in this case); Re_d the Reynolds number for the insulated reactor diameter; D is the diameter of the insulated reactor, which is equal to the diameter of the exposed reactor plus two times the insulation height (0.05 m); ρ the density of air at 300 K; v the wind velocity; μ the viscosity of air at 300 K.

Once the surface temperature is unknown, it is not possible to directly determine the Prandtl number at the surface. The alternative is to implement an iterative algorithm to obtain the surface temperature and the convective coefficient. In the first run of the algorithm, an arbitrary surface temperature (900 K) is used to obtain a value for the convective coefficient h through the Zukauskas's correlation ($Pr_s = 0.720$ at 900 K). In this correlation, Nu_D the Nusselt number for

the insulated reactor diameter (d); h is the convective coefficient; k is the thermal conductivity; C , m , and n are constants that depend on Reynolds and Prandtl numbers.

$$Nu_D = \frac{h * D}{k} = C * Re_d^m * Pr^n * \left(\frac{Pr}{Pr_s}\right)^{0.25}$$

$$\frac{h * 0.173 \text{ m}}{0.0263 \text{ W}/(\text{m} * \text{K})} = 0.26 * 35700^{0.6} * 0.707^{0.37} * \left(\frac{0.707}{0.720}\right)^{0.25}$$

$$h = 18.6 \text{ W}/(\text{m}^2 * \text{K})$$

Then, a new surface temperature can be calculated using the found value of h . The surface temperature is the one at which the heat loss due to convection equals the heat conduction from the inner part of the insulation to the outer surface. The thermal conductivity (k) of the insulator was informed by the manufacturer as $0.12 \text{ W}/(\text{m.K})$.

$$Q_{convection} = h * Area * (T_{s1} - 300K)$$

$$Q_{conduction} = 2 * \pi * L * k * (1/\ln(D/d)) * (900K - T_{s1})$$

Where T_{s1} is the surface temperature for the first iteration. Taking $Q_{convection}$ to be equal to $Q_{conduction}$:

$$\begin{aligned} & \left[18.63 \frac{\text{W}}{\text{m}^2 * \text{K}} \right] * (\pi * 0.173 \text{ m} * 0.5 \text{ m}) * (T_{s1} - 300K) \\ & = \frac{2 * \pi * (0.5 \text{ m}) * [0.12 \text{ W}/(\text{m.K})]}{\ln(0.173 \text{ m}/0.073 \text{ m})} * (900K - T_{s1}) \end{aligned}$$

Resolving for T_{s1} :

$$T_{s1} = 347.7 \text{ K}$$

The second run of the iterative algorithm starts with the calculation of a new convective coefficient at the calculated temperature ($Pr_s = 0.700$ at 347 K).

$$Nu_D = \frac{h * D}{k} = C * Re_d^m * Pr^n * \left(\frac{Pr}{Pr_s}\right)^{0.25}$$

$$\frac{h * 0.173 \text{ m}}{0.0263 \text{ W}/(\text{m} * \text{K})} = 0.26 * 35700^{0.6} * 0.707^{0.37} * \left(\frac{0.707}{0.700}\right)^{0.25}$$

$$h = 18.76 \text{ W}/(\text{m}^2 * \text{K})$$

Then, a new surface temperature (T_{s2}) can be calculated using the found value of h. Taking Qconvection to be equal to Qconduction, and resolving for T_{s2} :

$$\begin{aligned} \left[18.76 \frac{\text{W}}{\text{m}^2 * \text{K}}\right] * (\pi * 0.173 \text{ m} * 0.5 \text{ m}) * (T_{s2} - 300\text{K}) \\ = \frac{2 * \pi * (0.5 \text{ m}) * [0.12 \text{ W}/(\text{m} * \text{K})]}{\ln(0.173 \text{ m}/0.073 \text{ m})} * (900\text{K} - T_{s2}) \end{aligned}$$

Resolving for T_{s2} :

$$T_{s2} = 347.4 \text{ K}$$

As T_{s1} and T_{s2} are almost identical, the algorithm ends its routine. The final surface temperature is taken as 347 K and the convective coefficient as 18.8 W/(m²*K) for the insulated area.

Insulated lids convective coefficient and surface temperature

$$\begin{aligned} L &= \frac{d}{2} * \sqrt{\pi} = \frac{0.10\text{m}}{2} * \sqrt{\pi} = 0.089\text{m} \\ Re_L &= \frac{\rho * v * L}{\mu} = \frac{(1.1614 \text{ kg}/\text{m}^3) * (3.28 \text{ m}/\text{s}) * (0.089\text{m})}{(184.6 * 10^{-7} \text{ N} * \text{s}/\text{m}^2)} = 1.84 * 10^4 \end{aligned}$$

Where L is the length of the flat plate, which is considered to be equal to the edge of and square whose area is equivalent to the reactor lid's area; Re_L the Reynolds number for the equivalent plate length; ρ the density of air at 300 K; v the wind velocity; μ the viscosity of air at 300 K; Pr is the Prandtl number of air at 300 K.

The convective coefficient follows from the correlation below, which considers the lids to be flat plates in a laminar flow with constant thermal flow. In this correlation, Nu_L is the Nusselt number for the equivalent length and h is the convective coefficient. Pr is the Prandtl number of air at 300 K, 0.707.

$$Nu_L = \frac{h * L}{k} = 0.453 * Re_L^{1/2} * Pr^{1/3}$$

$$Nu_L = \frac{h * 0.089m}{0.0263W/(m * K)} = 0.453 * (1.84 * 10^4)^{1/2} * 0.707^{1/3}$$

$$h = 16.2W/(m^2 * K)$$

Once the convective coefficient is known, the surface temperature can be calculated using the found value of h . The surface temperature (T_s) is the one at which the heat loss due to convection equals the heat conduction from the inner part of the insulation to the outer surface. The thermal conductivity (k) of the insulator was informed by the fabricant as 0.12 W/(m.K). The insulation height (X) is 0.05 m.

$$Q_{convection} = h * Area * (T_s - 300K)$$

$$Q_{conduction} = \frac{k * Area}{X} * (900K - T_s)$$

$$\left(16.2 \frac{W}{m^2 * K}\right) * Area * (T_s - 300K) = \frac{0.12 W/(m.K) * Area}{0.05m} * (900K - T_s)$$

Resolving for T_s :

$$T_s = 377.4K$$

The final surface temperature is taken as 377 K and the convective coefficient as 16.2 W/(m²*K) for the insulated lids.

APPENDIX F - PARABOLIC TROUGH REACTOR HEAT LOSSES

Heat loss of the exposed cylinder

According to the convective heat flow equation (INCROPERA; BERGMAN; LAVINE, 2008):

$$Q_{exposed} = h * Area * (T_{hot} - T_{cold})$$

Where $Q_{exposed}$ is the heat loss the exposed cylinder, h is the convective coefficient, $Area$ is the cylinder area, T_{hot} the hot surface temperature and T_{cold} is the ambient temperature.

$$Q_{exposed} = \left[26.3 \frac{W}{m^2 * K} \right] * (\pi * 0.073m * 0.50m) * (900K - 300K)$$

Heat loss of the insulated cylinder

According to the convective heat flow equation (INCROPERA; BERGMAN; LAVINE, 2008):

$$Q_{insulated} = h * Area * (T_{hot} - T_{cold})$$

Where $Q_{insulated}$ is the heat loss of the insulated cylinder, h is the convective coefficient, $Area$ is the cylinder area, T_{hot} the hot surface temperature and T_{cold} is the ambient temperature.

$$Q_{insulated} = \left[18.8 \frac{W}{m^2 * K} \right] * (\pi * 0.173m * 0.50m) * (347K - 300K)$$

$$Q_{exposed} = 240 W$$

Heat loss of the insulated lids

According to the convective heat flow equation (INCROPERA; BERGMAN; LAVINE, 2008):

$$Q_{lid} = h * Area * (T_{hot} - T_{cold})$$

Where Q_{lid} is the heat loss of an insulated lid, h is the convective coefficient, $Area$ is the cylinder area, T_{hot} the hot surface temperature and T_{cold} is the ambient temperature.

$$Q_{lid} = \left[16.2 \frac{W}{m^2 * K} \right] * (\pi * (0.05m)^2) * (377K - 300K)$$

$$Q_{lid} = 9.8 W$$

Total heat loss

Because the cylindrical reactor is designed to have 90% of its area covered by the ceramic fiber insulator, while the other 10% are exposed, it is considered that the total heat loss of the partially insulated cylinder is equal to the sum of 90% of the heat loss of a fully insulated cylinder and 10% of the heat loss of a fully exposed cylinder. The convective loss at the insulated lids is also considered for the calculation of the total heat loss.

$$Q_{loss} = 0.9 * Q_{insulated} + 0.1 * Q_{exposed} + 2 * Q_{lid}$$

$$Q_{loss} = 0.9 * 240 W + 0.1 * 1809 W + 2 * 9.8 W$$

$$Q_{loss} = 416 W$$

APPENDIX G – PARABOLIC DISH REACTOR CONVECTIVE COEFFICIENTS

Thermophysical properties of air at atmospheric pressure were obtained from Incropera et al. (2008)(INCROPERA; BERGMAN; LAVINE, 2008). The velocity of the airflow considered in the calculations was the global average wind velocity over land, 3.28 m/s(ARCHER; JACOBSON, 2005).

Insulated cylinder convective coefficient

From data obtained from Incropera et al. (2008):

$$Pr = 0.707$$

$$Pr_s = 0.720$$

$$Re_d = \frac{\rho * v * d}{\mu} = (1.1614 \text{ kg/m}^3) * (3.28 \text{ m/s}) * (0.125 \text{ m}) / (184.6 * 10^{-7} \text{ N.s/m}^2)$$

$$Re_d = 25794$$

Where Pr is the Prandtl number of air at 300 K; Pr_s the Prandtl number for the surface temperature (900 K, in this case); Re_d the Reynolds number for the reactor diameter; ρ the density of air at 300 K; v the wind velocity; d the diameter of the insulated reactor; μ the viscosity of air at 300 K.

Considering the Zukauskas correlation below:

$$Nu_d = \frac{h * d}{k} = C * Re_d^m * Pr^n * \left(\frac{Pr}{Pr_s}\right)^{0.25}$$

Where Nu_d the Nusselt number for the reactor diameter; h is the convective coefficient; C , m , and n are constants that depend on Reynolds and Prandtl numbers; k is the thermal conductivity of air.

For Reynolds numbers between 1000 and 200000, values of C and m are respectively 0.26 and 0.6. For Pr numbers lower than 10, 0.37 is the corresponding value of n . Thus, following Zukauskas's correlation, the convective coefficient of the exposed area can then be calculated.

$$\frac{h * 0,125 \text{ m}}{0.0263 \text{ W}/(\text{m} * \text{K})} = 0.26 * 25794^{0.6} * 0.707^{0.37} * \left(\frac{0.707}{0.720}\right)^{0.25}$$

$$h = 21.2 \text{ W}/(\text{m} * \text{K})$$

Lid's convective coefficient

$$L = \frac{d}{2} * \sqrt{\pi} = \frac{0.075 \text{ m}}{2} * \sqrt{\pi} = 0.0665 \text{ m}$$

$$Re_L = \frac{\rho * v * L}{\mu} = \frac{(1.1614 \text{ kg}/\text{m}^3) * (3.28 \text{ m}/\text{s}) * (0.0665 \text{ m})}{(184.6 * 10^{-7} \text{ N} \cdot \text{s}/\text{m}^2)} = 1.37 * 10^4$$

Where L is the length of the flat plate, which is considered to be equal to the edge of the square whose area is equivalent to the reactor lid's area; Re_L the Reynolds number for the equivalent plate length; ρ the density of air at 300 K; v the wind velocity; μ the viscosity of air at 300 K; Pr is the Prandtl number of air at 300 K.

The convective coefficient follows from the correlation below, which considers the lids to be flat plates in a laminar flow with constant thermal flow. In this correlation, Nu_L is the Nusselt number for the equivalent length and h is the convective coefficient. Pr is the Prandtl number of air at 300 K, 0.707.

$$Nu_L = \frac{h * L}{k} = 0.453 * Re_L^{1/2} * Pr^{1/3}$$

$$Nu_L = \frac{h * 0.0665 \text{ m}}{0.0263 \text{ W}/(\text{m} * \text{K})} = 0.453 * (1.37 * 10^4)^{1/2} * 0.707^{1/3}$$

$$h = 18.7 \text{ W}/(\text{m}^2 * \text{K})$$

APPENDIX H – PARABOLIC DISH REACTOR FINAL TEMPERATURE

Insulated lid heat loss

Heat transfer on the insulated lid has to overcome two resistances, conduction resistance over the insulating material and convective resistance.

$$R^{-1} = r_1^{-1} + r_2^{-1}$$

$$Q_{Ins.lid} = \left(\frac{X}{k * Area} + \frac{1}{h * Area} \right)^{-1} * (T_{reactor} - T_{air})$$

$$Q_{Ins.lid} = \left(\frac{0,025m}{0.12 \text{ W/(m. K)} * \pi * \frac{0,075^2}{4}} + \frac{1}{18.7 \frac{W}{m^2 * K} * \pi * \frac{0,075^2}{4}} \right)^{-1} * (T_{reactor} - 300K)$$

$$Q_{Ins.lid} = 0,0168 * (T_{reactor} - T_{air})$$

Where X is insulator thickness; k is the insulator thermal conductivity; h is the convective coefficient.

Insulated cylinder heat loss

Heat transfer on the insulated cylinder also has to overcome two resistances, conduction resistance over the insulating material and convective resistance.

$$Q_{Ins.cyl} = \left(\frac{\ln(D/d)}{2 * \pi * L * k} + \frac{1}{(h * Area)} \right)^{-1} * (T_{reactor} - T_{air})$$

$$Q_{Ins.cyl} = \left(\frac{\ln(0,125m/0,075)}{2 * \pi * 0,05m * 0.12 \text{ W/(m. K)}} * + \frac{1}{(21.2 \text{ W/(m * K)} * \pi * \frac{0,125^2}{4})} \right)^{-1} * (T_{reactor} - T_{air})$$

$$Q_{Ins.cyl} = 0,0574 * (T_{reactor} - T_{air})$$

Where L is insulator thickness; k is the insulator thermal conductivity; d is the reactor diameter; D is the insulated reactor diameter; h is the convective coefficient.

Exposed lid heat loss

Heat transfer on the exposed lid has to overcome only convective resistance.

$$Q_{Exp.lid} = (18.7 \text{ W}/(\text{m}^2 * \text{K}) * \pi * \frac{0,075^2}{4}) * (T_{reactor} - T_{air})$$

$$Q_{Exp.lid} = 0,0826 * (T_{reactor} - T_{air})$$

Where h is the convective coefficient.

Final reactor temperature calculation

For the final reactor temperature calculation, the following mass balance is taken:

$$Q_{total} = Q_{Ins.lid} + Q_{Exp.lid} + Q_{Ins.cyl}$$

$$158 \text{ W} = 0,156 * (T_{reactor} - 300\text{K})$$

$$T_{reactor} = 1313 \text{ K}$$

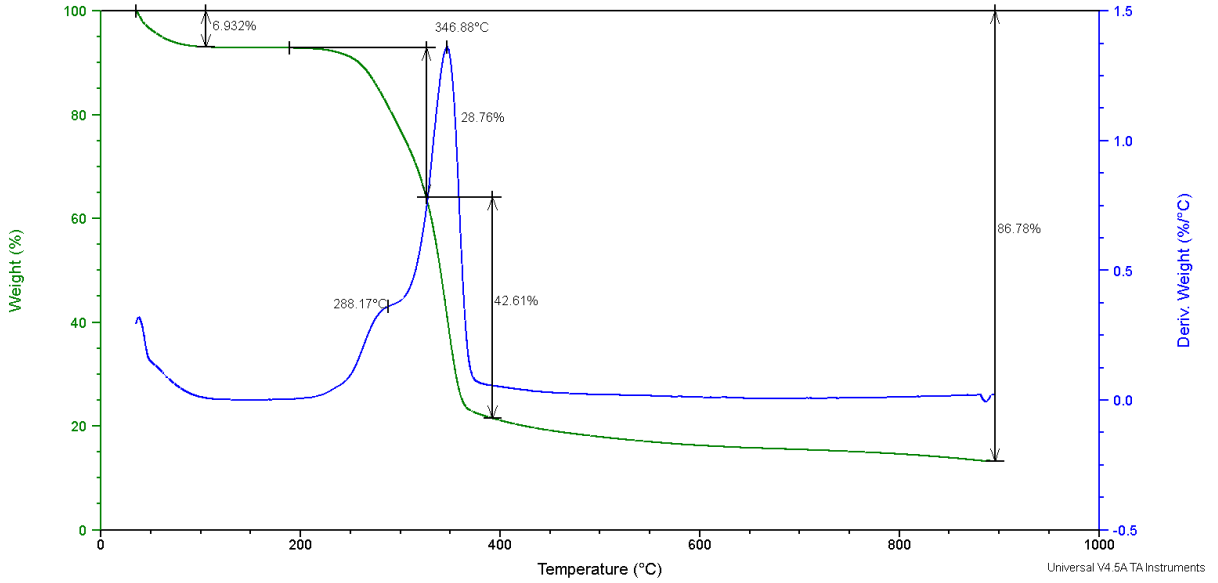
APPENDIX I – TGA/DTG CURVES

- Luffa cylindrica*

Sample: Bucha Vegetal
Size: 5.8470 mg
Method: Pirolise

TGA

File: C:\...TGA\Daniel\Pedro\bucha vegetal.001
Operator: Daniel
Run Date: 22-Jan-2021 13:48
Instrument: TGA Q50 V20.13 Build 39

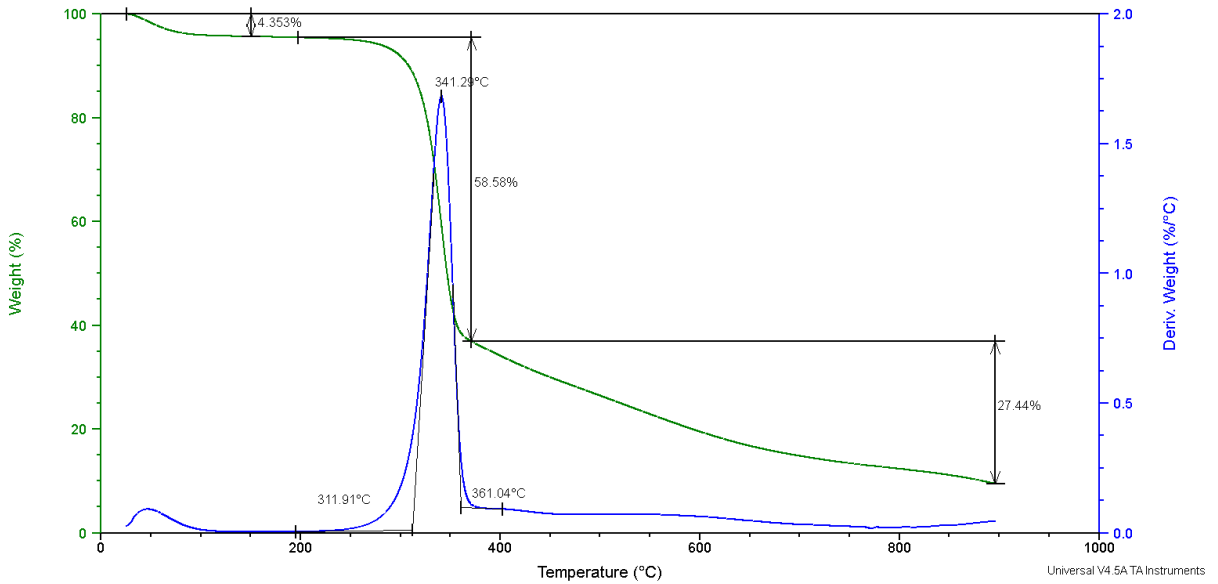


- B300-2

Sample: 300C 2cm
Size: 6.0100 mg
Method: Pirolise

TGA

File: C:\...Pedro\300C 2cm (RE342-21).001
Operator: Poliana
Run Date: 15-Feb-2021 08:44
Instrument: TGA Q50 V20.13 Build 39

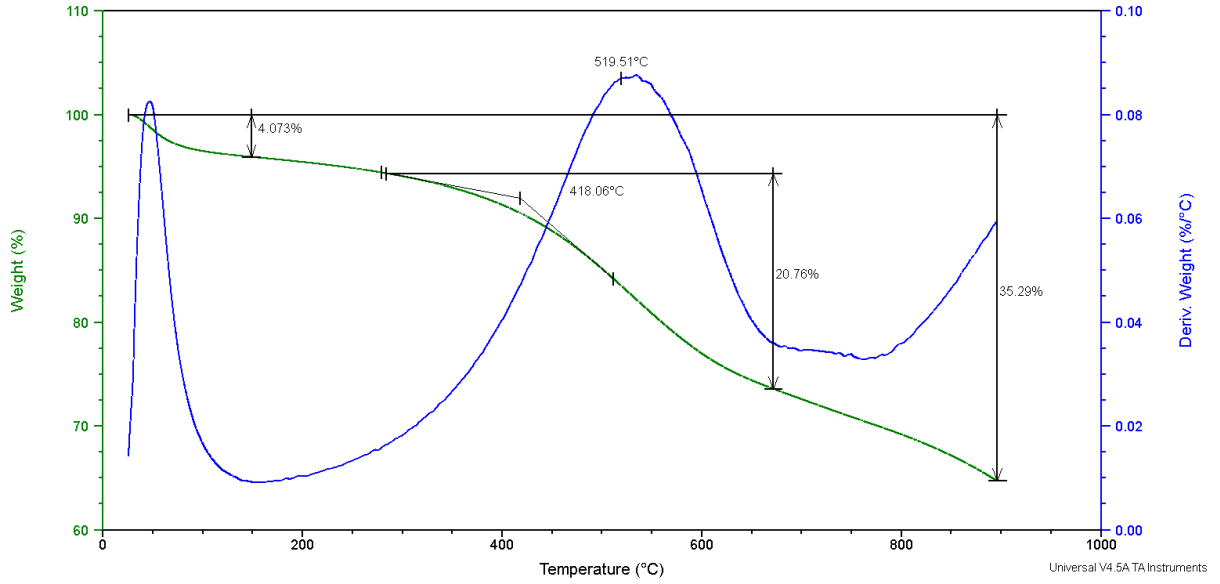


- B400-2

Sample: 500C 2cm
 Size: 8.0000 mg
 Method: Pirolise

TGA

File: C:\...Pedro\500C 2cm (RE345-21).001
 Operator: Poliana
 Run Date: 16-Feb-2021 09:40
 Instrument: TGA Q50 V20.13 Build 39

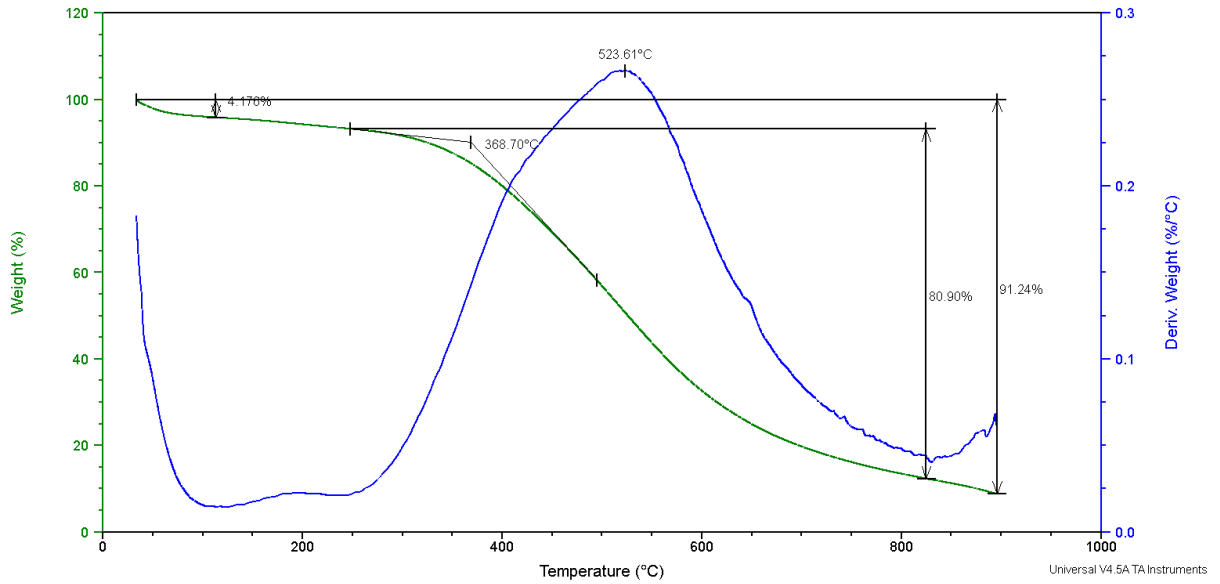


- B500-2

Sample: 400C 2cm
 Size: 5.5090 mg
 Method: Pirolise

TGA

File: C:\TAData\TGA\Daniel\Pedro\400C 2cm.001
 Operator: Daniel
 Run Date: 29-Jan-2021 11:08
 Instrument: TGA Q50 V20.13 Build 39

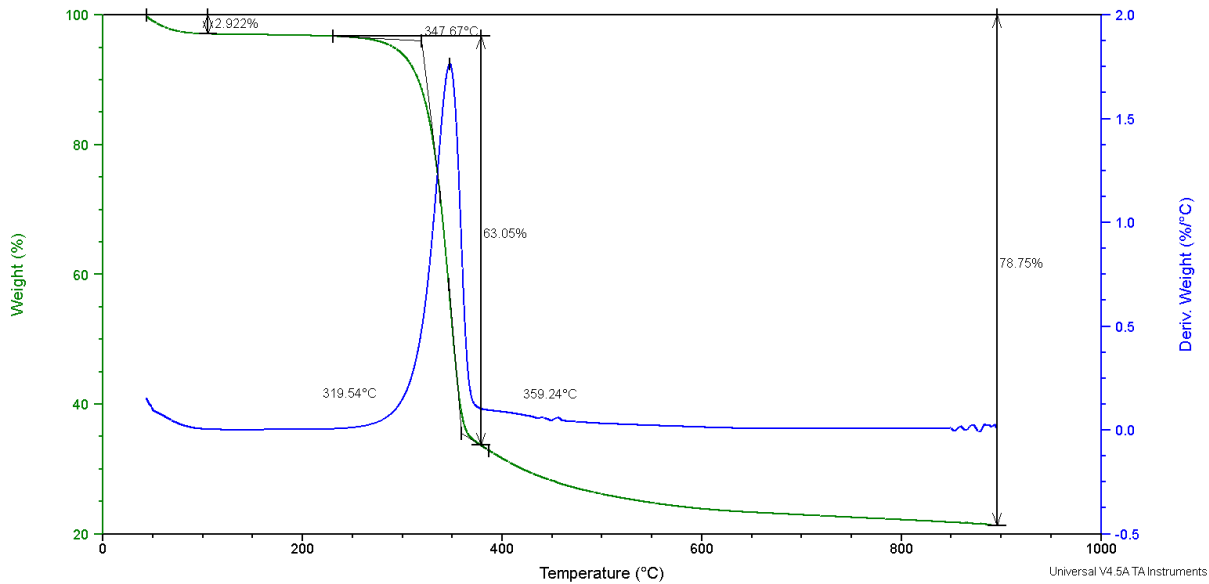


- B300-10

Sample: 300C 10cm
 Size: 8.2270 mg
 Method: Pirolise

TGA

File: C:\...TGA\Daniel\Pedro\300C 10cm.001
 Operator: Daniel
 Run Date: 22-Jan-2021 15:46
 Instrument: TGA Q50 V20.13 Build 39

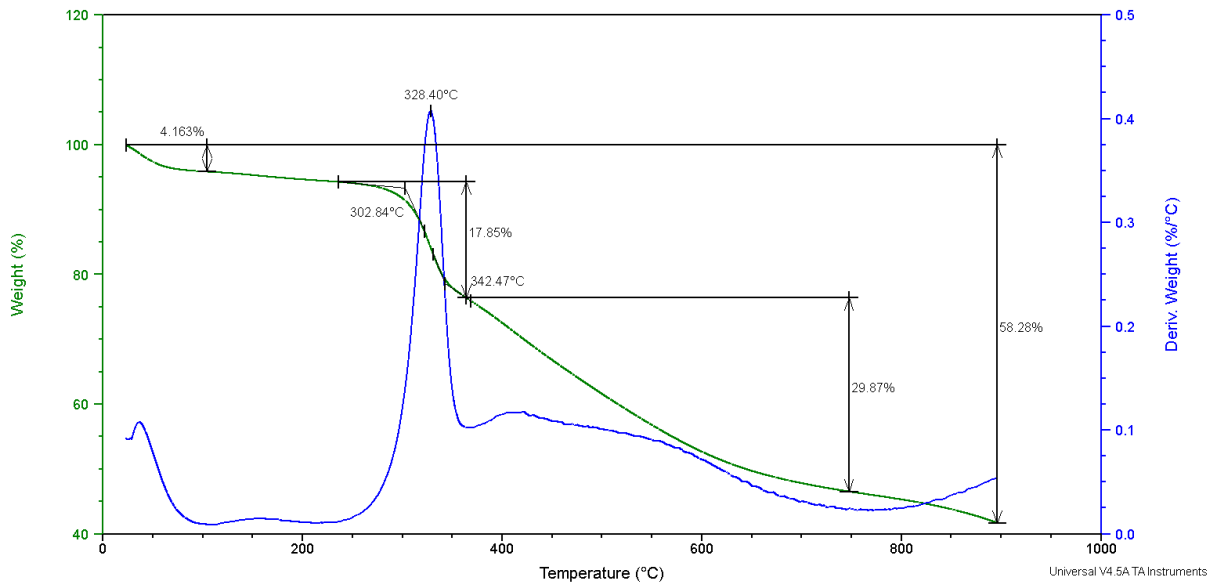


- B400-10

Sample: 400C 10cm
 Size: 6.2310 mg
 Method: Pirolise

TGA

File: C:\...TGA\Daniel\Pedro\400C 10cm.001
 Operator: Daniel
 Run Date: 25-Jan-2021 08:11
 Instrument: TGA Q50 V20.13 Build 39

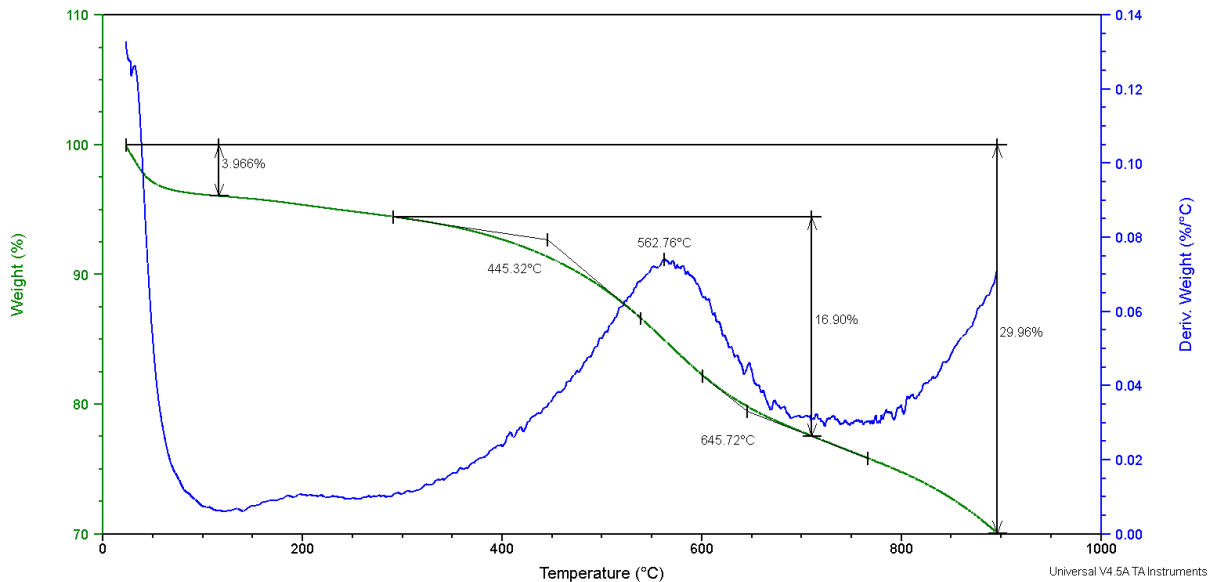


- B500-10

Sample: 500C 10cm
 Size: 3.9110 mg
 Method: Pirolise

TGA

File: C:\...TGA\Daniel\Pedro\500C 10cm.001
 Operator: Daniel
 Run Date: 26-Jan-2021 08:08
 Instrument: TGA Q50 V20.13 Build 39

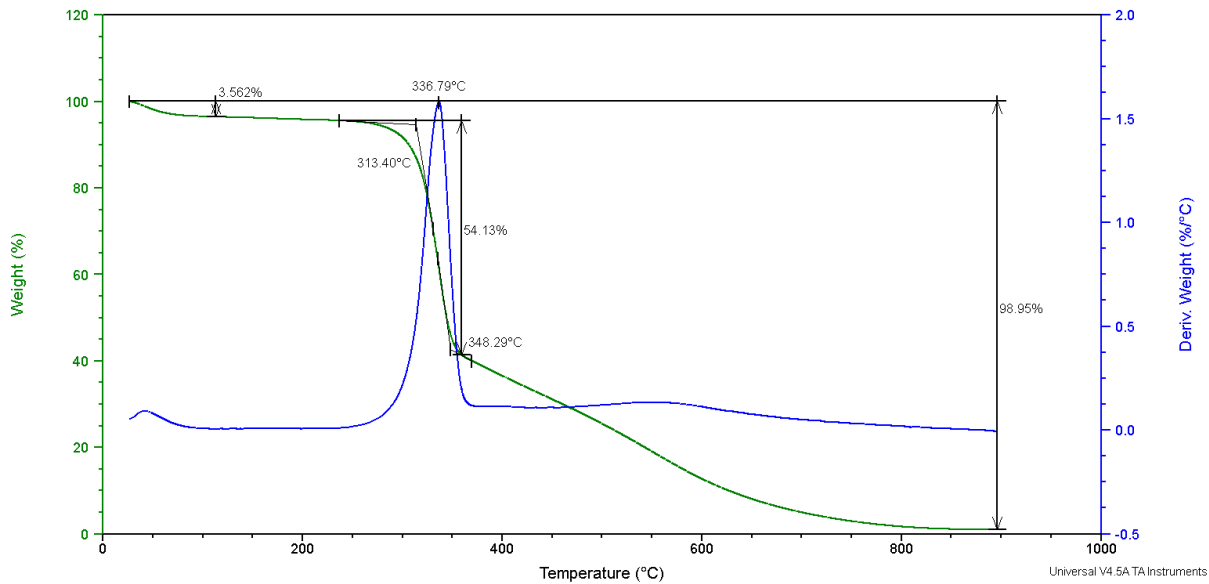


- B300-20

Sample: 300C 20cm
 Size: 5.4880 mg
 Method: Pirolise

TGA

File: C:\...TGA\Daniel\Pedro\300C 20cm.001
 Operator: Daniel
 Run Date: 29-Jan-2021 09:03
 Instrument: TGA Q50 V20.13 Build 39

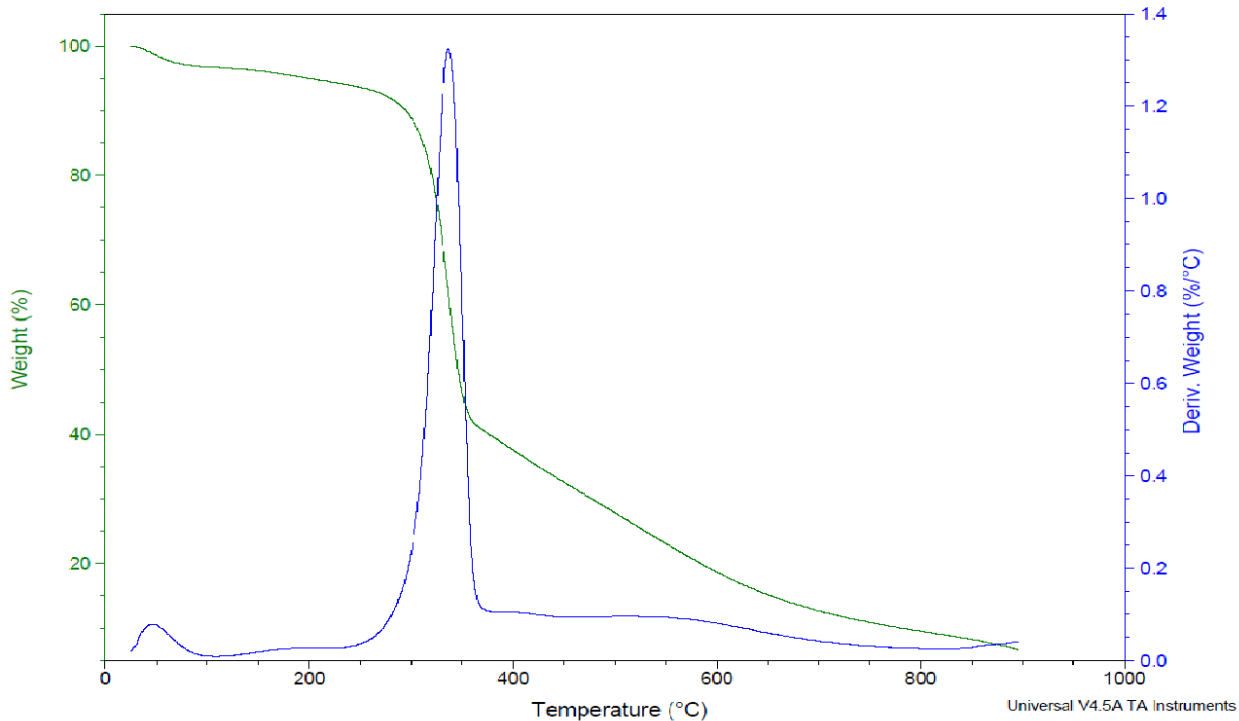


- B400-20

Sample: 400C 20cm rep (RE559-21)
 Size: 8.0160 mg
 Method: Pirolise

TGA

File: C:\...\Pedro\400C 20cm rep (RE559-21).001
 Operator: Poliana
 Run Date: 09-Mar-2021 09:25
 Instrument: TGA Q50 V20.13 Build 39

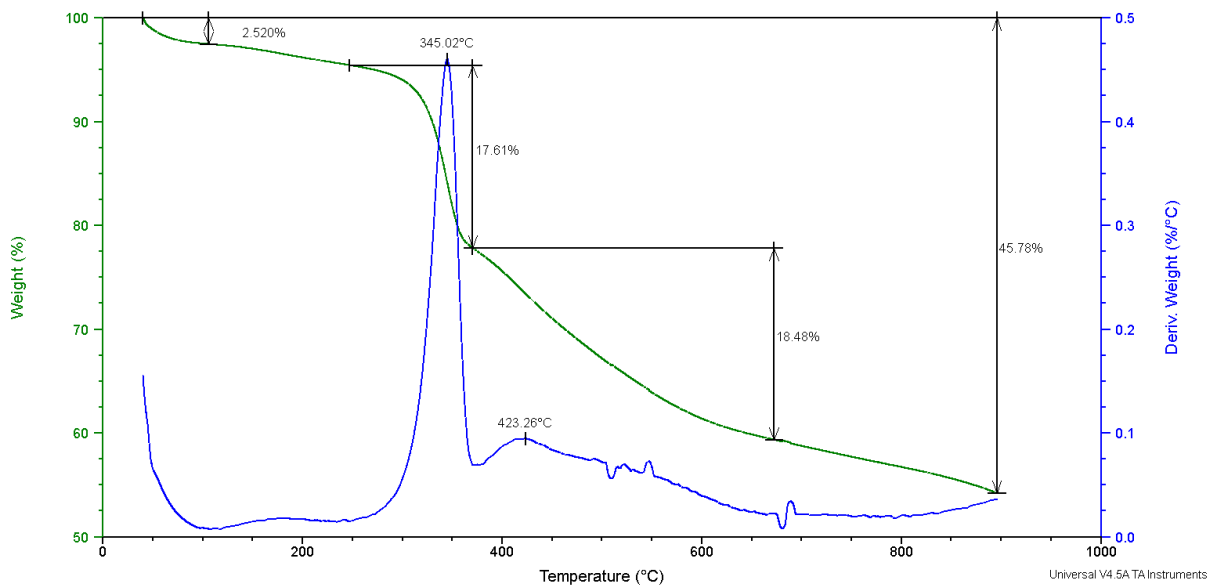


- B500-20

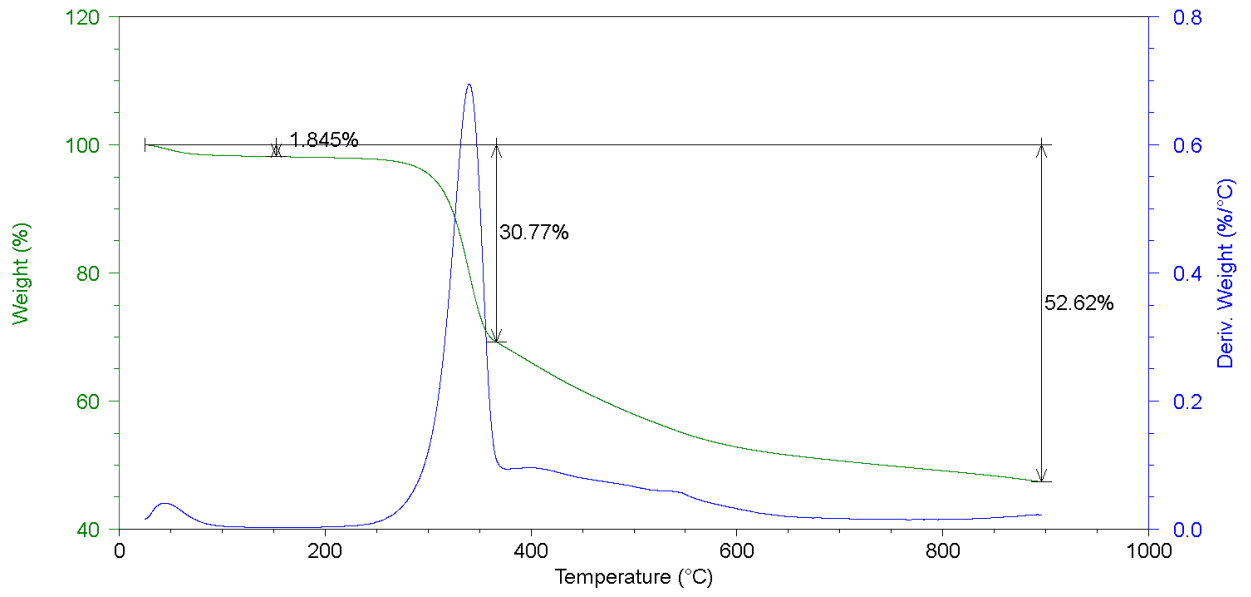
Sample: 500C 20cm
 Size: 4.7670 mg
 Method: Pirolise

TGA

File: C:\...TGA\Daniel\Pedro\500C 20cm.001
 Operator: Daniel
 Run Date: 25-Jan-2021 10:08
 Instrument: TGA Q50 V20.13 Build 39



- Solar Biochar



APPENDIX J – LUFFA CYLINDRICA EDS

